UNIVERSITY OF CALIFORNIA
SANTA CRUZ

ADVANCED ANOMALY DETECTION TECHNIQUES FOR CYBER-PHYSICAL POWER SYSTEMS

A dissertation submitted in partial satisfaction of the
requirements for the degree of

DOCTOR OF PHILOSOPHY

in

ELECTRICAL AND COMPUTER ENGINEERING

by

Gabriel Andres Intriago Velasquez

September 2024

The Dissertation of Gabriel Andres Intriago Velasquez is approved by:

Dr. Patrick Mantey, Chair

Dr. Yu Zhang, Advisor

Dr. Leila Parsa

Peter Biehl
Vice Provost and Dean of Graduate Studies

Table of Contents

List of Figures

List of Tables

List of Symbols

$\mathcal{O}$	Feature space
$\mathcal{Y}$	Class space
α_i	Rotating angle of the i-th inverter
$\gamma_{di,qi}$	d-axis and q-axis auxiliary state variables for the PI current controllers at the i-th inverter
ω_b	Nominal frequency of the microgrid
ω_{ci}	Cut-off frequency of the low-pass filters for the active and reactive power at the i-th inverter
ω_{com}	Frequency of the common reference frame
ω_i	Frequency of the i-th inverter
ω_{ni}	Nominal frequency of the i-th inverter
$\phi_{di,qi}$	d-axis and q-axis auxiliary state variables for the PI voltage controllers at the i-th inverter

C_{fi}	Capacitance of the LC filter at the i-th inverter
$i_{ldi,lqi}$	d-axis and q-axis output current magnitude of the i-th inverter
$i^*_{ldi,lqi}$	d-axis and q-axis output current magnitude of the PI voltage controller at the i-th inverter
$i_{lodi,loqi}$	d-axis and q-axis current magnitude of the i-th load
$i_{odi,oqi}$	d-axis and q-axis current magnitude of the LC filter at the i-th inverter
K_{IC_i}	Current PI controller's integral gain at the i-th inverter
K_{IV_i}	Voltage PI controller's integral gain at the i-th inverter
K_{PC_i}	Current PI controller's proportional gain at the i-th inverter
K_{PV_i}	Voltage PI controller's proportional gain at the i-th inverter
L_{ci}	Output connector's inductance at the i-th inverter
L_{fi}	Inductance of the LC filter at the i-th inverter
L_{lo}	Inductance of the i-th load
m_{Pi}	Active power droop coefficient at the i-th inverter
n_{Qi}	Reactive power droop coefficient at the i-th inverter
P_i	Active power of the i-th inverter
Q_i	Reactive power of the i-th inverter

R_{ci} Output connector's resistance at the i-th inverter

R_{fi} Resistance of the LC filter at the i-th inverter

R_{lo} Resistance of the i-th load

t_c Fault clearing response time

t_o Fault detection response time

$v_{bdi,bqi}$ d-axis and q-axis bus voltage magnitude at the PCC of the i-th inverter

v_{bi} Total bus voltage magnitude $\sqrt{v_{bdi}^2 + v_{bqi}^2}$ of the i-th inverter

$v_{idi,iqi}^*$ d-axis and q-axis output voltage magnitude of the PI current controller at the i-th inverter

V_{ni} Nominal voltage magnitude of the i-th inverter

$v_{odi,oqi}$ d-axis and q-axis output voltage magnitude of the i-th inverter

$v_{odi,oqi}^*$ d-axis and q-axis voltage magnitude references for the PI voltage controller at the i-th reference frame

v_{oi} Total output voltage magnitude $\sqrt{v_{bdi}^2 + v_{bqi}^2}$ of the i-th inverter

$\boldsymbol{\beta}_{\mathrm{u}}^{(i)}$ Sparse code vector corresponding to the i-th unlabeled feature vector

$\boldsymbol{o}_t$ Feature vector at time t

D Matrix dictionary of basis vectors or atoms

L	Base learner
W	Variable-length window with historic instances
y_t	class label corresponding to $\boldsymbol{o}_t$

Abstract

Advanced Anomaly Detection Techniques for Cyber-Physical Power Systems

by

Gabriel Andres Intriago Velasquez

Electric power systems are undergoing significant transformations that have brought fundamental challenges to the system's situational awareness. This research aims to develop reliable strategies to manage such challenges for two typical anomaly-detection problems in modern power systems: cyber-attacks and faults. The growing complexity of power grids due to the penetration of intelligent monitoring devices and recent technological advances in energy management systems have rendered cyber-physical systems like electric grids increasingly vulnerable to cyber threats. These anomalies have been estimated to have a considerable economic impact during a severe cyber-attack. This work is essential for protecting modern and clean power systems because it implements effective methods for detecting and isolating faults in emerging technologies for renewable electric energy generation. Consequently, this research not only reduces the frequency of disruptions but also reduces the risk of damage, lowers maintenance costs, and extends the lifespan of equipment. This work is vital in preventing economic and power-related disruptions caused by cyber-attacks and faults.

Cyber-physical power systems (CPPS) rely on wide-area monitoring, protection, and control (WAMPAC) technologies, allowing operators to drive modern systems more efficiently and reliably. WAMPAC technologies use modern devices such as intelligent relays, digital recorders, and phasor measurement units (PMUs) to monitor the CPPS state. However, such devices produce continuous and unbounded data streams, posing significant data handling, storage, and processing challenges. Moreover, WAMPAC devices and their communication links are vulnerable to cybersecurity risks. To cope with these challenges, this study introduces two novel event detection methods for cyber and non-cyber contingencies based on the Hoeffding Adaptive Tree classifier. This robust machine learning classifier can handle high-velocity and high-volume data streams with limited memory and low computational burden. We consider several cyber and non-cyber events affecting the physics and monitoring infrastructure of CPPS, such as short-circuit faults, line maintenance, remote tripping command injection, relay setting change, and false data injection. The data are generated based on a modified IEEE 9-bus system. Simulation results show that our proposed approach outperforms the state-of-the-art method in the literature.

Fault detection is vital in ensuring the reliable and resilient operation of modern power systems. Its importance lies in swiftly identifying and isolating faults, preventing cascading failures, and enabling rapid power restoration. This work proposes a strategy based on observers and residuals for detecting internal faults in grid-forming inverters with power-sharing coordination for clean and small-scale AC microgrids. Grid-forming inverters will be the future drivers of modern and clean power systems to accelerate the adoption of renewable energy sources such as solar and wind. The dynamics of the inverters are captured through a nonlinear state space model. The design of our observers and residuals considers H_-/H_∞ conditions to ensure robustness against disturbances and responsiveness to faults. The proposed design is less restrictive than existing observer-based fault detection schemes by leveraging the properties of quadratic inner-boundedness and one-sided Lipschitz conditions. Also, this work introduces a residual-based adaptive threshold for fault detection. An inequality for the upper bound on the ℓ_2 norm of the residual is derived and used for designing the adaptive threshold. The upper bound is obtained via semidefinite programming with two linear matrix inequality constraints. The internal faults considered in this paper include actuator faults, busbar faults, and inverter bridge faults, which are modeled using vector-matrix representations that modify the state space model of the inverters. One significant advantage of the proposed methods is its cost-effectiveness, as it does not require additional sensors. Experiments are conducted on an islanded AC microgrid with three inductive lines, four inductive loads, and four grid-forming inverters to validate the merits of the proposed fault detection strategy. The results demonstrate that our designs outperform existing methods in the field.

Acknowledgments

Completing my doctoral studies represents a transcendental and indulgent achievement. I am deeply grateful to my academic supervisor, Professor Yu Zhang, for his invaluable guidance and exceptional mentorship during my PhD program. I owe much of the completion of this thesis to his academic and financial support. The direction and quality of my research have been shaped by his expertise, suggestions, and valuable feedback. I am truly fortunate to have had the opportunity to work under his mentorship, which not only contributed to the completion of this work but has also enhanced my academic and professional development. I want to thank Professor Patrick Mantey, who kindly agreed to serve as the chair of my dissertation committee. I am forever indebted to Patrick because he trusted in my abilities and decided to secure the funding to make it possible for me to be admitted to my doctoral studies at UCSC in 2019. Such a decision changed my life forever since if it hadn't happened, I wouldn't be where I am. I would also like to thank Professor Leila Parsa who served on my thesis reading committee.

I thank my beloved family and friends for their support and encouragement throughout my academic voyage. To my wife, Gabriela, for her endless support, understanding, and sacrifices that have been the foundation of my triumphs. To my parents, Raúl and Fátima, for their constant motivation and unconditional love, which maintained me through the challenges and successes of this endeavor. To my brothers Raúl and Andres, whose willingness to lend an ear, unwavering support,

and offer advice have been invaluable during this journey. To my labmates Jing, Sifat, Kejun, and Shourya, for their endless kindness and support, which multiplied prosperity by two and reduced hardship by half. I am forever indebted to them and will always carry their love and support with me.

Chapter 1

Introduction

Situational awareness has been receiving increasing attention for power systems, especially when it comes to the design of effective anomaly detection strategies. Such strategies can be defined as the cognition of the elements that allow the system operators, during routine procedures, to enable accurate detection of anomalous events such as cyber threats, non-cyber contingencies, and faults [4]. Moreover, power system operators constantly face numerous challenges to balance the electrical supply and demand due to modern electrical power systems' ever-growing size and complexity. Developing a scheme that detects anomalies in the power system per the standards imposed by regulators and policymakers is critical in preserving the system's reliability. However, multiple underlying factors govern the system's stability, turning the scheme's development into a highly complex process [5]. This research aims to provide anomaly detection procedures that leverage the system's underlying information, improving its situational awareness while coping with these challenges in modern power systems.

The ambition to increase the situational awareness of power systems and the ever-growing gathering of large volumes of energy data streams pose new challenges for traditional anomaly detection techniques, especially machine learning techniques. In such a scenario, a data-driven strategy inherits the requirements of streaming learning: process one instance at a time and at most once, use a limited amount of memory, work during a limited amount of time, and pose a timely prediction [6]. Also, we need to consider that the statistical properties of energy data are time-variant. That is, the data is expected to evolve unpredictably and unanticipated. Opposed to traditional machine learning, it is very likely that by the time any selection strategy is implemented, the underlying data distribution has changed, often making the strategy no longer valid [7]. In this context, designing an anomaly detection policy based on machine learning that chooses a relevant portion from the original data and adapts for data modeled as a stream becomes indispensable. Not doing so may incur performance degradation of machine learning algorithms and infeasible processing times under real-time environments such as power systems.

The electrical power system is currently evolving significantly from centralized to distributed generation. Most distributed energy sources rely on power-electronics-based technologies, allowing smooth energy conversion between the main grid and small-scale systems such as microgrids. In the coming years, microgrids will be increasingly dominated by a significant share of the generation mix stemming from renewable energy sources interfaced by grid-forming inverter technologies

[8, 9]. Microgrids in the grid-connected mode rely on the main grid for voltage and frequency regulation and benefit from upstream protection. However, ensuring stability in an islanded microgrid is more challenging than in the grid-connected mode [10]. An islanded microgrid functions as an independent system and must independently maintain reference voltage magnitude and frequency for its components. This situation is further aggravated when the power generators are grid-forming inverters, as they reduce the available electrical inertia in the system [11]. Therefore, it is crucial to have an intelligent fault detection (FD) strategy that is resilient against disturbances and sensitive to faults to prevent energy supply interruptions and promote a stable microgrid performance.

This work aims to answer questions about how using data from the power system under study could enable reliable anomaly detection of anomalous events: Can online machine learning algorithms detect cyber- and non-cyber contingencies in power systems? Do energy data behave as an unbounded stream with fluctuating underlying properties? Also, we attempt to answer questions about the design of model-based fault detection for grid-forming inverters: Are observer-centric and residual-based strategies appropriate for fault detection in grid-forming inverters? How do internal faults influence the behavior of grid-forming inverters? How does the built-in uncertainty of the inverter model affect the fault detection design?

1.1 Scope and organization

The main objective of this thesis is to design and evaluate the performance of novel anomaly detection strategies dedicated to improving the situational awareness of modern power systems. Specifically, this thesis investigates the effectiveness of the proposed strategies when dealing with a subset of anomalies: cyber-attacks, non-cyber contingencies, and faults. We acknowledge that the set of potential anomalies in modern power systems is vast and varied; however, detecting the subset of anomalies studied in this work enables a reliable and secure operation of modernized power systems. This thesis comprises four published articles, three journal papers, and one conference paper introducing events and fault detection schemes using machine learning for data streams and observer theory.

Chapter 2 introduces two novel event detection strategies for cyber-physical power systems using a tree-based online machine-learning algorithm [1]. The data obtained from the system are assumed to behave as a data stream, that is, as a continuous flow of data at a high rate of speed and time-varying statistical properties, also known as concept drift. However, such an assumption imposes hard constraints on the performance properties of the chosen algorithm, such as processing one data instance at a time, a reduced amount of memory, a limited processing time, and being ready to predict at any time. To deal with the performance challenges imposed by data streams, our detection strategies are designed as wrappers that enhance the ca-

[1] The material in this chapter was published at the 2021 IEEE Power and Energy Society General Meeting conference (https://ieeexplore.ieee.org/abstract/document/9637891) and IEEE ACCESS (https://ieeexplore.ieee.org/abstract/document/10054027).

pabilities of a high-performance algorithm for data streams, the Hoeffding Adaptive Tree (HAT). The first detection strategy improves HAT's performance by transforming its input data using a feature engineering approach based on semi-supervised learning. Our approach starts by building a dictionary of higher-level features (such as sudden, recurrent, or gradual changes) from unlabeled raw data. Then, the labeled data are represented as sparse linear combinations of learned dictionary atoms. We capitalize on those sparse codes to train the online classifier with efficient change detectors such as the drift detection method (DDM) and adaptive windowing (ADWIN). The second detection strategy presented in Chapter 2 develops an instance selection algorithm that facilitates data management by selecting the most relevant instances for the learning task, further reducing the computational burden and memory consumption. The instance selection algorithm is combined with the HAT classifier to deal with evolving phasor measurement unit (PMU) data streams by constantly retraining the classifier when system changes are detected. Our focus is to select the instances most similar to the target instance by using a spatiotemporal distance function that adapts to the range of the PMU measurements. The proposed selection algorithm can generally determine the optimal subset of data instances in a nonstationary streaming environment.

Chapter 3 sets the stage for detecting internal faults such as busbar, actuator, inverter bridge, and sensor faults in grid-forming inverters operating in islanded AC microgrids [2]. A nonlinear dynamic model in a state-space formulation describes

[2] The material in this chapter was published in IEEE Systems Journal (https://ieeexplore.ieee.org/document/10464193) and IEEE ACCESS

the inverters' dynamics, where the model considers the presence of bounded and polytopic parametric uncertainties. The triggering mechanism that detects the occurrence of faults consists of three essential components: the residual norm, the threshold, and a comparator. The comparator judges the occurrence of a fault when the residual norm exceeds the threshold and judges the absence of fault otherwise. One significant advantage of the proposed approaches in this chapter is their cost-effectiveness, as they do not require additional sensors for achieving fault detection. The first approach introduces an observer-centric approach using a time-varying residual norm and a fixed threshold for fault detection. Such a strategy leverages an $\mathcal{H}_{-}/\mathcal{H}_{\infty}$ optimization framework to design a Luenberger observer [12] that mimics the behavior of the inverter. Such a framework allows the design of an observer to be sensitive to faults and robust against disturbances. The proposed design is less restrictive than existing observer-based fault detection schemes based on the Lipschitz modeling of nonlinearities. Our approach assumes the nonlinear properties of the inverter model follow the quadratic inner-boundedness and one-sided Lipschitz conditions. The second approach preserves the residual norm obtained from the Luenberger observer while introducing an adaptive threshold for fault detection. The effectiveness of the adaptive threshold is assessed using busbar and sensor faults. An inequality for the upper bound on the ℓ_2 norm of the residual is derived and used for designing the adaptive threshold. The upper bound is obtained via semidefinite programming with two linear matrix inequality constraints.

(https://ieeexplore.ieee.org/document/10500414).

Chapter 2

Event detection for electric power networks

This chapter presents two novel adaptations of the Hoeffding Adaptive Tree (HAT) classifier for event detection and classification in power systems to enhance cyber-physical power systems' (CPPS) situational awareness. Using unlabeled and labeled data, the first method combines the HAT classifier with semi-supervised learning techniques to accurately distinguish cyber-attacks from regular system perturbations. The approach builds a dictionary by learning higher-level features from unlabeled data. The labeled data are then represented as sparse linear combinations of learned dictionary atoms. We capitalize on those sparse codes to train the online classifier and efficient change detectors. The second method combines HAT with a novel instance selection algorithm with three algorithmic stages to ease data management. The instance selection algorithm facilitates data management by selecting the most relevant instances for the learning task, reducing the computational burden and memory consumption. A cost and complexity analysis of the algorithm is discussed. The classifier can handle high-velocity, high-volume, and evolving data streams from the PMUs with reduced computational effort.

2.1 Literature review

The existing solutions for the contingency detection task can be categorized as model-, machine learning-, neural networks-, and streaming learning-based approaches. Event detection in power systems is challenging because most events are infrequent, the system's measurements are noisy, and the system's operating point changes continuously. Traditionally, model-based methods detect events by observing the deviation between the measurements of the system and its model. A significant disturbance indicates that an event has occurred in the system [13, 14]. The small-signal model of the system can be used to monitor the parametric sensitivity of the system's eigenvalues against load-altering attacks, as shown in [15]. However, large-scale attacks demand an analysis under nonlinear grid models rather than the linearized small-signal model. In [16], the authors develop a framework that leveraged the system model and a cumulative sum detector to identify stealthy false data injection (FDI) attacks in an AC smart grid. Despite the merits of these prior arts, these works face essential challenges, such as requiring a mathematical description of the system and its components, scaling to more extensive power networks, and being specific to certain events. In contrast, our work adopts a model-agnostic approach that can adapt to time-variant scenarios and discriminate events of multiple types.

Unlike model-based methods, machine learning and NN methods can operate without any information regarding the physics and mathematical models governing the power system [17–21]. In [22], the authors design an anomaly detection method using multivariate Gaussian models from micro-phasor measurement units (μPMUs) to detect malicious attacks. Nevertheless, the efficacy of such a method is limited to only two types of attacks: transient and steady. Another approach presented in [23] developed a framework that combines wavelet denoising and filtering to detect data anomalies accurately. However, the method did not show a favorable trade-off between computational time and accuracy. A collaborative machine learning-based framework for detecting attacks was proposed in [24]. This method can efficiently extract patterns from attack vectors. However, this method is limited to FDI attacks and does not incorporate a mechanism to adapt the model to evolving scenarios. Habibi et al. [21] combined time-series analysis with nonlinear autoregressive neural networks to study the effect of FDI attacks. Nonetheless, this approach needs to train neural networks for each distributed energy resource in the microgrid, which imposes a high computational burden. Machine learning and neural network methods have shown outstanding performance and flexibility in detecting events in power systems. However, their main shortcomings are the assumption of a static environment, the inability to retrain the models in real-time, and the high computational burden for model learning, especially for NN methods. The approach proposed in this work can detect changes in the underlying data distribution and retrain the model accordingly. The retraining process improves the model's accuracy without adding a significant processing burden.

Motivated by the discussions above, researchers have turned to stream learning to tackle the event detection task for power systems. In [25], Dahal et al. used a Hoeffding adaptive tree (HAT) to classify the normal operation and electrical faults of a power system operating with load fluctuations. Dahal demonstrated the applicability and ability of HAT to classify power system events. However, the experiments in Dahal's study were not designed to handle multiple events. The authors in [26] take a step further and modify the HAT classifier to incorporate two change detectors, the drift detection method (DDM) and adaptive windowing (ADWIN), to classify binary, ternary, and multiple events, including disturbances and cyberattacks. The authors rely on discretizing the dataset according to domain knowledge, which may not be affordable in a real-time scenario. Moreover, the results report a noticeable performance for binary and ternary events, but the performance for the multiple events scenario was moderate. In this study, our proposed classifier exhibits high accuracy and low computational cost when dealing with binary, ternary, or multiple events.

A method based on selecting the most promising features using gradient boosting trees to enhance the performance of several machine learning classifiers was presented in [27]. This study shows that feature engineering is a crucial consideration in event detection; however, the classifiers are trained to assume a stationary environment and may not capture the real-time changes occurring in the system. A framework that dynamically detects and classifies cyberattacks was presented in [28]. The framework consists of three modules: detection, classification, and signal retrieval. Although the method has been proven to detect and classify events under harsh learning conditions, it only detects FDI attacks. Moreover, this method depends on vast historical data, which may not represent the current system state.

We recommend this survey of statistical literature [29] for readers interested in anomaly detection for time series data.

2.2 Stream learning

2.2.1 Classification for data streams

Classification for data streams inherits many problems from traditional machine learning. There are also new challenges, such as one-pass learning, limited processing time and memory, and changes in data distribution. In this study, we focus on data stream classification. Let $\{(\boldsymbol{o}_t, z_t)\}_{t=1}^{\infty}$ denote a data stream containing a set of labeled instances. At time t, $\boldsymbol{o}_t \in \mathbb{R}^m$ denotes the vector of m features while z_t is the corresponding class label. Let $\mathcal{O}$ represent the entire feature space and $\mathcal{Z}$ the class space. A classification algorithm learns a mapping $f : \mathcal{O} \mapsto \mathcal{Z}$ such that it can be used to predict the class label for a new instance. Traditional classification can load all the data into memory. By contrast, stream classification is a one-pass strategy, meaning the processed instances are automatically discarded or only stored temporarily.

A learning model should meet the following criteria to comply with data stream learning [6]:

- Learn an instance at a time and inspect it at most once.
- The model must use a limited amount of memory.
- Require limited working time.
- The model must be able to predict at any time.

2.2.2 Concept drift

In the stream learning lexicon, *concepts* are defined as the target information that a model aims to predict using a set of features [30]. Data streams are inherently infinite, temporal, and dynamic. The data distribution may evolve, whereas the mapping between instances and targets can be time-varying. This situation results in the *concept drift* phenomena [7].

As a case of concept drift, feature drift occurs when a subset of features becomes irrelevant to a learning task [30]. This study's features are the PMU measurements, such as voltages, currents, and impedances. Feature drift in the context of power systems includes the following: (i) the removal of an existing PMU from the monitoring system, (ii) less informative voltage magnitude measurements owing

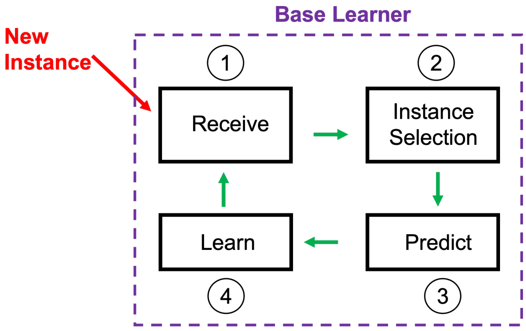

Figure 2.1: Streaming learning framework with instance selection.

to the injection of bad data (FDI), and (iii) changes in the PMU measurements due to cyber-attack events.

2.2.3 Prequential evaluation

We follow the rules of *Prequential evaluation* [31] to be compliant with the stream learning framework. Essentially, prequential evaluation comprises two major stages: testing and training. In the test stage, the base learner predicts the class of the next available instance from the stream. After the test stage, the model metrics are updated. The base learner processes the actual instance during training to update its structure and statistics. In our study, the training stage is governed by our proposed streaming instance selection method, which is explained in detail in the next section. Fig. 2.1 depicts the stream learning framework with instance selection.

2.2.4 The Hoeffding Adaptive Tree (HAT) classifier

HAT comprises three main components: a window to remember recent examples, a distribution-change detector, and an estimator for some input data statistics. Once a change is detected, an alternate tree will be created and grow with the instances appearing right after the change. The existing alternate tree will replace the current tree if it is more accurate. The HAT [32] classifier has the adaptive windowing (ADWIN) method as the change detector. A modified version of HAT is the HAD classifier with an additional change detector, the drift detection method (DDM).

ADWIN serves as an estimator and change detector that keeps a variable-length window $\mathcal{W}$ of recent data such that the window has the maximal length statistically consistent with the null hypothesis of the average value inside the window has not changed. When two “big enough" sub-windows of $\mathcal{W}$ have “distinct enough" averages, it can be said with high probability that a change in the data distribution has occurred and the older items in $\mathcal{W}$ should be dropped. The “big and distinct enough” can be quantitatively defined by the Hoeffding bound [33].

DDM is a change detector that relies on ‘context,’ defined as a set of contiguous examples whose data distribution is stationary. DDM incrementally controls the model’s error rate. Statistical theory guarantees that the error decreases if the data distribution remains stationary, and the error increases when the distribution changes. A new context is declared if the error reaches a warning level at instance

k_w and a drift level at instance k_d. This indicates a distribution change, and a new model is learned using the examples between k_w and k_d. A detailed explanation of DDM can be found in [34].

2.3 Datasets

We test our proposed methods with the multiclass industrial control system (ICS) cyber-attack dataset, which includes measurements of 37 events in an electric transmission system [35]. The publicly available dataset comprises 15 sets with 5000 instances and 128 features each. The datasets have three versions: binary, ternary, and multiclass dataset. Each of the four PMUs measures 29 features (voltages, currents, frequency, and impedances), adding up to 116 physical features. In addition, 12 additional cyber features correspond to information collected from networking and SCADA systems measured at substations such as SNORT, Syslog, and the control panel, totaling 128 features. The 37 simulated events are listed and distributed as follows:

- **Normal operation (1 event).** The system operated under stable conditions with smooth load changes.
- **Line maintenance (2 events).** The power lines are open via the protection relays.
- **Short-circuit fault (6 events).** A power line shortage can occur at different locations across lines.

- **Attack of remote tripping command injection (6 events).** An attacker opens a breaker by sending a command to the relay.

- **Attack of relay setting change (16 events).** An attacker turns off the secure relay configuration, which forces the relay to not trip against real faults and valid commands.

- **Attack of data Injection (6 events).** The attacker mimics a valid fault by changing the values of measurements such as voltages, currents, and impedances.

2.4 Performance Metrics

The performance metrics used in this study are listed below:

1. **Accuracy (*acc*):** Percent ratio of the number of correctly predicted instances to the total number of observed instances,

$$\text{Accuracy} = \frac{\text{Number of correct predictions}}{\text{Number of observed instances}}. \tag{2.1}$$

2. **Kappa (κ):** This statistic takes into account the probability of predictions agreement by chance [36],

$$\text{Kappa} = \frac{\rho_o - \rho_{\text{ran}}}{1 - \rho_{\text{ran}}}, \tag{2.2}$$

where ρ_o is the accuracy of the base learner under study, and ρ_{ran} is the accuracy of a random base learner. If Kappa is positive, the base learner is better than a random prediction. The metric Kappa is expressed in percent units.

3. **Time (t):** Processing time in seconds.

4. **Size (KB):** Size of the base learner in Kilobytes.

5. **Model cost ($cost$):** Amount of RAM (KB) deployed during one hour.

2.5 Combining semi-supervised learning and the HAT classifier

Labeling a massive amount of PMU data on the fly in practice is challenging and costly. Compared with data collection, which depends only on data storage capacity, data labeling often requires the rich domain knowledge of experts who can actively identify instances' labels. Therefore, we have abundant unlabeled and scarce labeled data with the same generative distribution. Due to this fact, semi-supervised learning (SSL) is an appropriate tool that combines a small amount of labeled data with a large amount of unlabeled data during training [37]. The first method proposes a novel approach for power system events and intrusion detection to improve classification performance by transforming the data through higher-level representations extracted from an unlabeled dataset.

2.5.1 Methodology

We obtain a dictionary by extracting higher-level features (such as oscillations, sudden changes, gradual changes, and stable periods) from the unlabeled dataset to represent later the labeled data, which are then used to train a classifier incrementally.

2.5.1.1 Online Dictionary Learning

Given a set of unlabeled instances $\left\{\mathbf{o}_{\mathrm{u}}^{(1)}, \ldots, \mathbf{o}_{\mathrm{u}}^{(p)}\right\}$, where $\mathbf{o}_{\mathrm{u}}^{(i)} \in \mathbb{R}^n$ is the i-th input feature vector, we formulate the following optimization problem to learn a new feature space representing these data points:

$$\min_{\mathbf{D}, \{\boldsymbol{\beta}_{\mathrm{u}}^{(i)}\}} \quad \frac{1}{2}\sum_{i=1}^{p} \left\|\mathbf{o}_{\mathrm{u}}^{(i)} - \mathbf{D}\boldsymbol{\beta}_{\mathrm{u}}^{(i)}\right\|_2^2 \tag{2.3a}$$

$$\text{s.t.} \quad \left\|\boldsymbol{\beta}_{\mathrm{u}}^{(i)}\right\|_0 \leq q,\ i = 1, 2, \ldots, p, \tag{2.3b}$$

$$\|\boldsymbol{d}_j\|_2 \leq 1,\ j = 1, 2, \ldots, m \tag{2.3c}$$

The optimization variables are the dictionary $\mathbf{D}_t = \left[\boldsymbol{d}_1, \ldots, \boldsymbol{d}_m\right] \in \mathbb{R}^{n \times m}$ and the sparse codes $\boldsymbol{\beta}_{\mathrm{u}}^{(i)} \in \mathbb{R}^m, i = 1, 2, \ldots, p$. We typically have $m \gg n$ so that the dictionary is rich enough. Hence, by the least square objective, each input $\mathbf{o}_{\mathrm{u}}^{(i)}$ is approximately represented as a linear combination of very few basis vectors in $\mathbf{D}$ with the corresponding coefficients given by $\boldsymbol{\beta}_{\mathrm{u}}^{(i)}$. The zero norm $\|\mathbf{a}\|_0$ denotes the number of non-zero coordinates of $\mathbf{a}$. Hence, the first constraint forces the vector

$\boldsymbol{\beta}_\mathrm{u}^{(i)}$ to have at most q nonzero elements. The energy of each atom (basis) in the dictionary $\mathbf{D}$ is bounded by one, as given by the second constraint. This constraint prevents the entries of $\mathbf{D}$ from being arbitrarily large while the entries of $\boldsymbol{\beta}_\mathrm{u}^{(i)}$ are minimal.

We leverage the alternating minimization method for the resulting nonconvex problem (1), i.e., minimizing one variable at each step while keeping all other variables fixed [38]. In the first step, we obtain the sparse codes $\boldsymbol{\beta}_\mathrm{u}^{(i)}, i = 1, 2 \dots, p$. The second step updates the dictionary $\mathbf{D}$.

- *Sparse coding – optimization over* $\boldsymbol{\beta}_\mathrm{u}^{(i)}$: Start with a fixed random dictionary $\mathbf{D}$, and solve (1) with the orthogonal matching pursuit (OMP) algorithm to obtain the $\boldsymbol{\beta}_\mathrm{u}^{(i)}$ that corresponds to the unlabeled point $\mathbf{o}_\mathrm{u}^{(i)}$ for $i = 1, 2, \dots, p$.
- *Dictionary update – optimization over* $\mathbf{D}$: Keep $\{\boldsymbol{\beta}_\mathrm{u}^{(i)}\}_{i=1}^{p}$ fixed, find the dictionary $\mathbf{D}_t$ by sequentially updating each atom via the block-coordinate descent (BCD) algorithm:

$$\mathbf{c}_j = \mathbf{A}_{jj}^{-1}(\mathbf{b}_j - \mathbf{D}_{t-1}\mathbf{a}_j) + \mathbf{d}_j, \qquad j = 1, 2, \dots, m \tag{2.4}$$

$$\mathbf{d}_j = \frac{\mathbf{c}_j}{\max(\|\mathbf{c}_j\|_2, 1)}, \qquad j = 1, 2, \dots, m, \tag{2.5}$$

where $\mathbf{D}_{t-1}$ is the dictionary at the previous iteration. The matrices $\mathbf{A} = [\mathbf{a}_1, \dots, \mathbf{a}_m] = \boldsymbol{\beta}_\mathrm{u}^{(i)} \boldsymbol{\beta}_\mathrm{u}^{(i)\top} \in \mathbb{R}^{m \times m}$ and $\mathbf{B} = [\mathbf{b}_1, \dots, \mathbf{b}_m] = \mathbf{o}_\mathrm{u}^{(i)} \boldsymbol{\beta}_\mathrm{u}^{(i)\top} \in \mathbb{R}^{n \times m}$ carry the information of the updated $\boldsymbol{\beta}_\mathrm{u}^{(i)}$'s. The update repeats until $\mathbf{D}_t$

converges.

2.5.1.2 New Feature Representation

Consider a set of labeled instances $\{(\mathbf{o}_\ell^{(1)}, z^{(1)}), \ldots, (\mathbf{o}_\ell^{(q)}, z^{(q)})\}$, where $\mathbf{o}_\ell^{(i)} \in \mathbb{R}^n$ is the ℓ-th input feature vector with label $z^{(i)} \in \{1, \ldots, N_C\}$ where N_C is the number of classes. Upon learning the dictionary $\mathbf{D}^*$ as elaborated above, the labeled data can be represented by using the basis vectors of $\mathbf{D}$. This is carried out by solving the following problem via the OMP for each labeled data point:

$$\min_{\boldsymbol{\beta}_\ell^{(i)}} \quad \frac{1}{2}\left\|\mathbf{o}_\ell^{(i)} - \mathbf{D}^*\boldsymbol{\beta}_\ell^{(i)}\right\|_2^2 \tag{2.6a}$$

$$\text{s.t.} \quad \left\|\boldsymbol{\beta}_\ell^{(i)}\right\|_0 \leq q. \tag{2.6b}$$

In other words, a labeled data point is now approximately represented as a linear combination of the learned atoms:

$$\mathbf{o}_\ell^{(i)} = \mathbf{D}\boldsymbol{\beta}_\ell^{(i)} + \boldsymbol{\xi}, \tag{2.7}$$

where $\boldsymbol{\xi}$ is the reconstruction error. We preserve each original label of $z^{(i)}$ by attaching it to the new representation, i.e., the q-sparse code $\boldsymbol{\beta}_\ell^{(i)}$ in a higher dimensional space. Finally, we train the HAD classifier with these new representations using the software package MOA [39].

Remark 2.5.1 (Matching pursuit vis-a-vis LASSO)**.** The sparse dictionary learning

Algorithm 1 Semi-supervised HAD (SSHAD)

```
Require:
    1) Unlabeled data $\{\mathbf{o}_{\mathrm{u}}^{(1)}, \ldots, \mathbf{o}_{\mathrm{u}}^{(p)}\}$
    2) Labeled data $\{(\mathbf{o}_{\ell}^{(1)}, z^{(1)}), \ldots (\mathbf{o}_{\ell}^{(q)}, z^{(q)})\}$.
    3) Randomly initialize $\mathbf{D}$ from unlabeled data vectors.
    4) Maximum iteration: max_iter = 200.
Normalize the labeled and unlabeled data.
for $t = 1$ to max_iter do
    Compute the sparse code $\boldsymbol{\beta}_{\mathrm{u}}$ with $\mathbf{D}_{t-1}$ by solving (1).
    Update $\mathbf{D}_t$ keeping the matrix $\boldsymbol{\beta}_u$ fixed.
end for
Solve (2.6b) to obtain the matrix $\boldsymbol{\beta}_{\ell}$.
Attach to $\boldsymbol{\beta}_{\ell}$ the labels from $\mathbf{o}_{\ell}$.
Train HAD with the new labeled dataset $\left\{(\boldsymbol{\beta}_{\ell}^{(1)}, z^{(1)}), \ldots, (\boldsymbol{\beta}_{\ell}^{(q)}, z^{(q)})\right\}$ using MOA.
return The trained HAD classifier.
```

problem generally has two formulations: matching pursuit and LASSO. The former is shown by problem (1), while the latter is relaxing ℓ_0 norm to ℓ_1 norm and lifting to the objective as a soft constraint. The matching pursuit formulation explicitly guarantees q-sparsity, which is more user-friendly in finding the "best" value of q by trial-and-error simulations. According to our numerical experiments, the solution to the matching pursuit is more stable numerically.

Algorithm 1 features two essential differences from the algorithm in [40]. In [40], the authors build the dictionary using self-taught learning (unlabeled and labeled datasets having different generative distributions [41]) to train later and test an SVM classifier with the new representation of the labeled dataset. In contrast, our model builds the dictionary using SSL and incrementally trains a HAD classifier with all the transformed labeled dataset instances. In a nutshell, our algorithm capitalizes on semi-supervised knowledge to enhance the HAD classifier's overall performance. We name the proposed algorithm SSHAD, where "SS" stands for semi-supervised, to differentiate it from the original version of HAD presented in [26].

2.5.2 Numerical Experiments

We ran all the experiments using MATLAB, WEKA, and the massive online analysis (MOA) software [42]. The relevant parameters were obtained by using cross-validation. The value of max_iter = 200 yielded the best results. The parameter q was set to 10 for both OMP procedures, i.e., each of $\boldsymbol{\beta}_u^{(i)}$'s and $\boldsymbol{\beta}_\ell^{(i)}$'s had at most ten nonzero values. We tested different sizes for the dictionary and found that 130 atoms performed the best. For both OMP optimization problems, the tolerance of the squared ℓ_2-norm residual was set to 0.01. Finally, the parameters for the HAT classifier were set to the default values in MOA.

We conducted classification experiments using the 2-class, 3-class, and 37-class datasets. The performance results were obtained with five different sizes, determined by the labeled dataset's sampling ratio. All values given in figures and tables are 10-fold average. The performance of our model improved with the increased size of the unlabeled dataset. It can be seen that the performance gets saturated with 50,000 unlabeled data points.

Fig. 2.2, 2.3, and Tab. 2.1 show the classification results for the 2-class and 3-class datasets. It can be seen that the performances of SSHAD and HAD were similar. However, when it comes to the 37-class dataset, our model outperformed

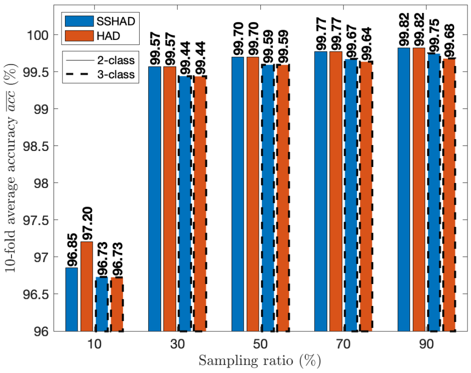

Figure 2.2: 10-fold average accuracy ($\overline{acc}$) comparison between SSHAD with parameter $q = 10$ and HAD using the 2-class and 3-class datasets.

HAD as shown in Fig. 2.6, 2.4, and Tab. 2.2. These results corroborated the merits of our proposed approach; representing the data with higher-level features yielded a more accurate identification of events in power systems. Moreover, as shown in Fig. 2.5, SSHAD is robust to bad data.

Table 2.1: The 3-class dataset: 10-fold average Kappa ($\overline{\kappa}$) and cost ($\overline{cost}$) comparisons between SSHAD ($q = 10$) and HAD.

Sampling	$\overline{\kappa}$(%)		$\overline{cost}$ (Ram-Hour)	
Ratio	SSHAD	HAD	SSHAD	HAD
10%	82.25	82.29	1.43×10^{-8}	1.37×10^{-8}
30%	88.36	88.44	2.18×10^{-8}	2.07×10^{-8}
50%	**69.87**	69.57	$\mathbf{2.87 \times 10^{-8}}$	2.89×10^{-8}
70%	**59.56**	59.28	$\mathbf{3.67 \times 10^{-8}}$	3.83×10^{-8}
90%	**51.91**	51.70	$\mathbf{4.63 \times 10^{-8}}$	5.27×10^{-8}

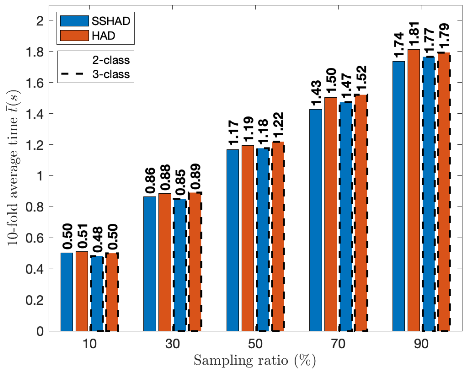

Figure 2.3: 10-fold average time ($\bar{t}$) comparison between SSHAD with parameter q = 10 and HAD using the 2-class and 3-class datasets.

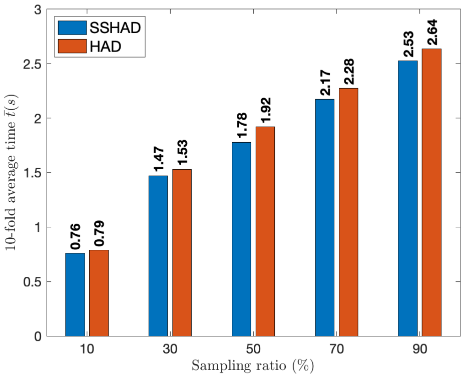

Figure 2.4: 10-fold average time ($\bar{t}$) comparison between SSHAD with parameter q = 10 and HAD using the 37-class dataset.

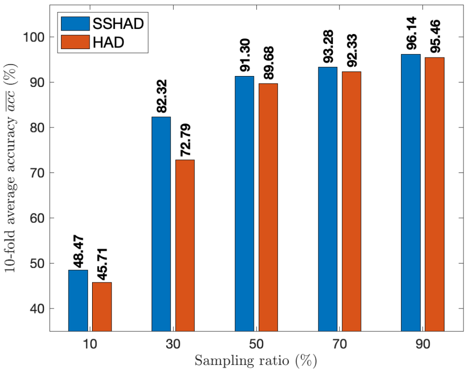

Figure 2.5: 10-fold average time ($\bar{t}$) comparison between SSHAD with parameter q = 10 and HAD using the 37-class dataset in the presence of 10% of bad data.

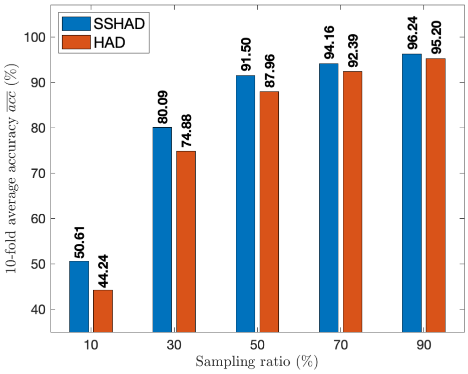

Figure 2.6: 10-fold average accuracy ($\overline{acc}$) comparison between SSHAD with parameter $q = 10$ and HAD using the 37-class dataset.

Table 2.2: The 37-class dataset: 10-fold average Kappa ($\overline{\kappa}$) and cost ($\overline{cost}$) comparisons between SSHAD ($q = 10$) and HAD.

Sampling Ratio	$\overline{\kappa}$(%)		$\overline{cost}$ (Ram-Hour)	
	SSHAD	HAD	SSHAD	HAD
10%	**29.80**	28.39	$\mathbf{5.80 \times 10^{-8}}$	5.88×10^{-8}
30%	**69.62**	62.32	$\mathbf{1.20 \times 10^{-7}}$	1.64×10^{-7}
50%	**79.48**	77.41	$\mathbf{9.24 \times 10^{-8}}$	1.09×10^{-7}
70%	**82.33**	80.30	$\mathbf{1.09 \times 10^{-7}}$	1.13×10^{-7}
90%	**85.64**	84.38	$\mathbf{1.24 \times 10^{-7}}$	1.28×10^{-7}

2.6 The HAT classifier and instance selection

This section discusses the adaptation of the HAT classifier with a novel instance selection algorithm to deal with real-time event detection tasks in power systems. Our model-agnostic approach relies on streaming learning to handle high-velocity and volume data streams with reduced computational effort. The HAT classifier uses an incremental decision tree classifier that learns from evolving data streams and handles data with concept drift. The instance selection algorithm accommodates data handling by selecting the most relevant data instances for the classification task, further reducing the processing and memory burden. The instance selection algorithm is combined with the HAT classifier to deal with evolving PMU data streams by constantly retraining the classifier when system changes are detected.

2.6.1 Methodology

In this section, we first present the concept of spatiotemporal similarity. Next, we discuss our proposed streaming instance selection's stream learning setup and details. Finally, we briefly describe the base learners.

2.6.1.1 Linear Spatio-temporal Similarity

Our proposed instance selection technique for data streams is based on the similarity among instances. The similarity captures the comparability of a pair of instances and is measured using a distance function. The concept of similarity

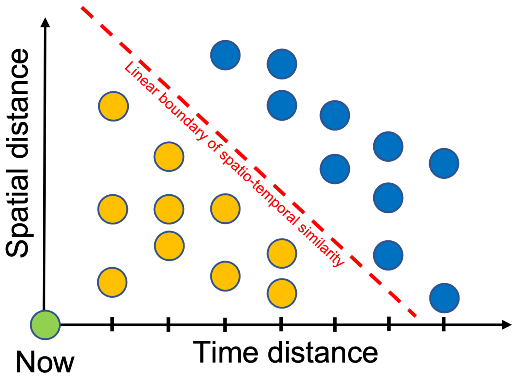

Figure 2.7: Linear combination of time and spatial distances. Each circle corresponds to a historical instance. The green circles are the target instance, while the yellow ones are similar to the targets because they have the least spatiotemporal distance determined by the red similarity boundary [1].

is inversely related to the concept of distance [43]. In other words, the smaller the distance between the instances, the more similar they are. Usually, the term *distance* is associated with distance in space. However, distance can not only be defined in space but also in time. Moreover, distance can be defined as a function of time and space, as suggested in [1] and shown in Fig. 2.7.

Remark 2.6.1. Potentially accurate results can be obtained using a spatiotemporal distance for contingency detection in power systems. For example, an instance with a low time distance but a high spatial distance may represent an abrupt change in the concept, such as transitioning from a normal operation to a single line fault. An instance with a low spatial and high time distance may indicate the evolution of a concept such as a single line fault under two different loading conditions.

Let $\boldsymbol{o}_t \in \mathbb{R}^m$ be the target instance whose class is to be predicted, $\boldsymbol{o}_i \in \mathbb{R}^m$ an already observed instance, $T(\cdot)$ a distance function in time, and $S(\cdot)$ a distance function in space. More formally, the spatiotemporal distance between $\boldsymbol{o}_t$ and $\boldsymbol{o}_i$ is defined as the following linear relationship:

$$E(\boldsymbol{o}_t, \boldsymbol{o}_i) = T(\boldsymbol{o}_t, \boldsymbol{o}_i) + S(\boldsymbol{o}_t, \boldsymbol{o}_i) \tag{2.8}$$

To simplify the notation, we refer to the distance from $\boldsymbol{o}_i$ to the target instance $\boldsymbol{o}_t$ as E_{t-i}. In Figure 2.7, we illustrate the concept of linearly combining spatial and time distances. There are multiple candidate functions to measure the spatial distance $S(\cdot)$, such as the Euclidean distance, Manhattan distance, or cosine similarity distance. In this study, we choose the Euclidean distance:

$$S(\boldsymbol{o}_t, \boldsymbol{o}_i) = \|\boldsymbol{o}_t - \boldsymbol{o}_i\|_2 \tag{2.9}$$

Assuming uniformly spaced time intervals and considering the N most recent observed instances, we choose the distance in time, defined as a linear function of the time indices:

$$T(\boldsymbol{o}_t, \boldsymbol{o}_i) = \frac{|t-i|}{N} \tag{2.10}$$

Other more complex time distances can be chosen; for example, the exponential function $T(\boldsymbol{o}_t, \boldsymbol{o}_i) = e^{|t-i|}$. This choice gives more importance to recent instances; however, we leave this and other complex spatial and time distance functions for future work.

Algorithm 2 Main Loop for Streaming Learning

```
Require: $\mathcal{M} = \{(\boldsymbol{o}_t, z_t)\}_{t=1}^{\infty}$, base learner $\mathcal{L}$
for $t = 1, 2, 3, \ldots$ do
    ▷ Scale the feature vector $\boldsymbol{o}_t$ incrementally
    ▷ Test $\mathcal{L}$ with $(\boldsymbol{o}_t, z_t)$
    ▷ Update the model metrics
    ▷ Train $\mathcal{L}$ with SIS using Algorithm 3
end for
```

A weight can be assigned to the Euclidean distance function using a fixed or cross-validation strategy [1]. This work assigns a time-variant weight β_t to the Euclidean distance function to reduce the impact of an inappropriate range of feature values. To do so, we use a scaling function $s : \mathbb{R}^m \mapsto \mathbb{R}^m$ that transforms the feature domain of all instances so that the values of the features are on a similar scale. Specifically, we scale the instances such that the values of the features have zero mean and unit variance. At each time step, the running mean and variance are maintained. Scaling differs from offline scaling because the exact means and variances are unknown beforehand [44]. Thus, the Euclidean distance becomes:

$$S(\boldsymbol{o}_t, \boldsymbol{o}_i) = \|s(\boldsymbol{o}_t) - s(\boldsymbol{o}_i)\|_2 = \beta_t \|\boldsymbol{o}_t - \boldsymbol{o}_i\|_2 \tag{2.11}$$

Remark 2.6.2. Power systems measurements make the spatiotemporal distance vulnerable to improper feature scaling because measurements exhibit different orders of magnitude. For example, voltage magnitudes may be reported in kilovolts and currents in amperes.

Algorithm 3 SIS

```
Require: base learner $\mathcal{L}$, set of most recent instances $\mathcal{R} = \{(\boldsymbol{o}_{t-i}, z_{t-i})\}_{i=1}^{N}$
▷ Reorder instances from set $\mathcal{R}$ using Algorithm 4
▷ Reset the base learner $\mathcal{L}$
▷ Search the optimal size for sliding window and train the base learner $\mathcal{L}$ using Algorithm 5
Return $\mathcal{L}$
```

Algorithm 4 Reorder

```
Require: Target instance $\boldsymbol{o}_t$, set of most recent instances $\mathcal{R} = \{(\boldsymbol{o}_{t-i}, z_{t-i})\}_{i=1}^{N}$
for $i = 1, \dots, N$ do
    ▷ Compute the distance $E_{t-i}$ according to (2.8)
end for
▷ Sort the distances in ascending order $E_{g(1)} < E_{g(2)} < \cdots < E_{g(N)}$
▷ Build the natural-valued function $g : \mathcal{K} \mapsto \mathcal{V}$, where $\mathcal{K} = \{1, 2, \dots, N\}$, and $\mathcal{V} = \{t-1, t-2, \dots, t-N\}$
Return $g$
```

2.6.1.2 The Instance Selection Algorithm

This section describes the proposed stream instance selection (SIS) algorithm. Let $\boldsymbol{o}_t$ be the target instance, $\mathcal{L}$ be the base learner, and $\mathcal{R} = \{(\boldsymbol{o}_{t-i}, z_{t-i})\}_{i=1}^{N}$ the set containing the most recent observed instances. Let $g : \mathcal{K} \mapsto \mathcal{V}$ denote the one-to-one natural-valued function, where $\mathcal{K} = \{1, 2, \dots, N\}$, and $\mathcal{V} = \{t-1, t-2, \dots, t-N\}$. Algorithm 2 presents the steps of the main loop of stream learning, where the SIS algorithm is used to enhance the performance of the base learner. The algorithm has three algorithmic stages explained as follows:

(1) Reorder: The observed instances are sorted in ascending order according to their distance to the target instance $\boldsymbol{o}_t$. The sorting procedure assigns a new set of indices $\{g(1), g(2), \dots, g(N)\}$ to the observed instances, so the base learner is trained first with the most similar instances. Algorithm 4 presents the steps of this stage.

(2) Reset: The base learner is reset to forget what was learned in the previous time step. This reset allows the model to adapt to concept drifts. The effectiveness of bypassing concept drifts depends on N.

(3) Search: In this stage, SIS uses a sliding window $\mathcal{W}$ containing previous instances to train the base learner. The size of the window $\mathcal{W}$ is chosen dynamically, which is upper bounded by N. SIS evaluates the trained base learner with a trial set containing the k most recent instances. The trial set is indexed by time $\{t-1, t-2, \ldots, t-N\}$, and not by the sorted indices $\{g(1), g(2), \ldots, g(N)\}$. The training window $\mathcal{W}$ is found using a warm restart to alleviate the processing of all the most recent instances in $\mathcal{R}$. SIS performs a local search around the previous best window size to find the new best size. Let b be the previous best window size and r a natural number that defines the search size. SIS searches the next best window's size in the interval $[l, u] \subseteq [1, N]$, where $l = b - r$ and $u = b + r$. Finally, SIS stops the search when the learner error on the trial set is less than a threshold ϵ. Algorithm 5 presents the steps involved in this stage.

At each time step, the SIS assigns a new index to the instances in $\mathcal{R}$ by

Table 2.3: Time and memory cost and complexity of the SIS algorithm per stage.

Stage		Time	Memory
(1) Reorder	Cost	$2N + N\log(N)$	$2N+1$
	Complexity	$\mathcal{O}(N\log(N))$	$\mathcal{O}(N)$
(2) Reset	Cost	1	1
	Complexity	$\mathcal{O}(1)$	$\mathcal{O}(1)$
(3) Search	Cost	$l + 2rk$	$2N$
	Complexity	$\mathcal{O}(l+2rk)$	$\mathcal{O}(N)$

solving the following optimization problem:

$$\begin{aligned} \min_{g : \mathcal{K} \mapsto \mathcal{V}} \quad & \sum_{i=2}^{N} |E_{g(i)} - E_{g(i-1)}| \\ \text{s.t.} \quad & \mathcal{K} = \{1, 2, \ldots, N\}, \\ & \mathcal{V} = \{t-1, t-2, \ldots, t-N\} \end{aligned} \tag{2.12}$$

Then, SIS finds the optimal window $\mathcal{W}$ by solving:

$$\begin{aligned} \min_{\mathcal{W} \subset \mathcal{R}} \quad & |\mathcal{W}| \\ \text{s.t.} \quad & l \leq |\mathcal{W}| \leq u, \\ & \frac{1}{k}\sum_{i=1}^{k} L_{\mathcal{W}}(\mathcal{L}(\boldsymbol{o}_{t-i}), z_{t-i}) \leq \epsilon, \\ & L_{\mathcal{W}} = \begin{cases} 1 & ; \mathcal{L}(\boldsymbol{o}_k) = z_k \\ 0 & ; \mathcal{L}(\boldsymbol{o}_k) \neq z_k \end{cases}, \\ & \boldsymbol{o}_{g(j)} \in \mathcal{W}, \quad \forall j \in \{1, \ldots, |\mathcal{W}|\} \end{aligned} \tag{2.13}$$

Algorithm 5 Search

```
Require: $|\mathcal{R}| = N$, base learner $\mathcal{L}$, natural-valued function $g$, number of testing instances $k$, previous best window size $b$, natural number $r$, error threshold $\epsilon$
▷ Set the upper and lower limits $u = b + r$, $l = b - r$
for $i = 1 : u$ do
    if $i > u$ then
        ▷ break
    end if
    ▷ Train the base learner $\mathcal{L}$ with $(\boldsymbol{o}_{g(i)}, z_{g(i)})$
    if $i < l$ then
        ▷ continue
    end if
    for $j = 1 \ : \ k$ do
        ▷ Test base learner $\mathcal{L}$ with $(\boldsymbol{o}_j, z_j)$
        ▷ Update metric learnerError
    end for
    if learnerError $< \epsilon$ then
        ▷ $b = i$ and break
    end if
end for
Return $\mathcal{L}$, $b$
```

Algorithms 4 and 5 describe the procedures of SIS for solving problems (2.12) and (2.13), respectively.

The computational complexity per stage of the SIS algorithm is presented in Table 2.3. The complexity is expressed using the big-O notation and corresponds to the worst case. The cost represents the time iterations and memory size based on the parameters of the SIS algorithm, such as N, l, r, and k. The complexity operator considers the higher-order terms of the cost only and without scaling. The cost and complexity of each stage are added to obtain the total cost and complexity of the SIS algorithm. The algorithm uses memory $\mathcal{O}(N)$ and time $\mathcal{O}(N \log(N) + l + 2rk)$, both of which are concentrated in stages (1) and (3). The second stage, Reset, is a one-line statement that reinitializes the parameters of the base learner. Considering stage (1), the distance computation (lines 1-3 of Algorithm 4) requires time and memory costs of N and $N+1$, respectively. The sorting statement (line 4 of Algorithm 4) sorts the set $\mathcal{R}$ and is executed using the Tim sort algorithm with a time cost of $N \log N$ and a memory cost of N. The natural-valued function g is a mapping with a memory size N, which is built using N iterations. The third stage trains the base learner using the first l instances (lines 6-9) of the reordered set $\mathcal{R}$. The base learner is then validated k times with the following $2r$ ordered instances of the set $\mathcal{R}$; thus, the time cost of the third stage is $l + 2rk$. The third stage requires having the set $\mathcal{R}$ in memory and the function g, each with size N. It is desirable to set $r \ll N/2$ and $k \ll N$ to reduce the complexity of the third stage.

2.6.2 Numerical Experiments

The experiments were conducted using Massive Online Analysis (MOA) [45] and River [46]. The MOA is an open-source Java framework for stream machine learning. River is an open-source Python package dedicated to developing online/streaming machine learning algorithms. We run the experiments using a MacBook Pro 2019, 2.8 GHz Intel Core i7 processor, 16 GB 2133 MHz LPDDR3 RAM, and 1 TB hard disk drive. Based on initial tests, we set the SIS hyperparameter $\epsilon = 0.1$. We used the Hoeffding Tree (HT) [47] and variants of the Hoeffding Adaptive Tree (HAT) [32] as the base learners for the experiments. After an initial trial on the MOA classifiers for streaming machine learning, we selected the HAT+DDM and HT+DDM learners because they performed better using a portion of the multiclass dataset. We set the base learners with the hyperparameters suggested in the related literature. More detailed tuning of the base learner's hyperparameters is left for future work. HAT+SIS and HT+SIS exhibited the same performance for the multiclass dataset. Finally, we chose HAT+SIS because it performed better for a price forecasting dataset, as shown in one of our experiments. We assessed the performance of the three learners in six case studies. Case studies are simulated by imitating real fault disturbances and cyber-attacks. We explored scenarios that affect the system's physics and monitoring architecture, including loading variation, PMU disappearance, and measurement overlapping. Additionally, we explored the performance of our proposed classifier using a price forecasting dataset.

2.6.3 Case Study I: Multiple Events

This case study evaluated the performance of the three learners with 37 events from the multiclass dataset. The hyperparameter tuning of the SIS method using grid search is presented in Table 2.4. A performance comparison is presented in Fig. 2.8. It can be seen that HAT+SIS is the best performer among all learners, whereas HAT+DDM is the worst performer. As shown in Fig. 2.8(a), HAT+SIS achieves an accuracy of more than 99% in the first 250 instances, whereas the accuracy of HAT+DDM and HT+DDM is less than 99% during the same interval. Around instance 4000, HAT+DDM and HT+DDM obtain an abrupt decrease in accuracy, while HAT+SIS remains unchanged. The learners HAT+DDM and

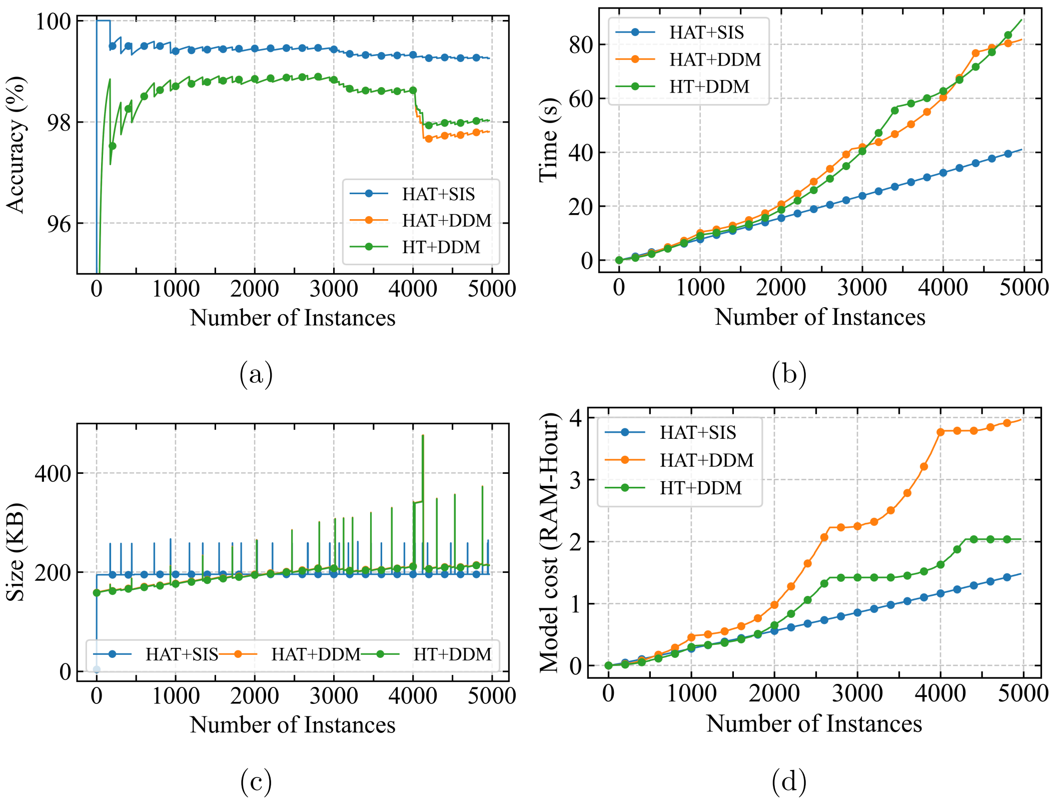

Figure 2.8: Performance comparison of the three learners in the case study I using the first set from the multi-class dataset. The evaluation considers the 37 events from the multi-class dataset in sequence. The comparison is shown for the following metrics: (a) Accuracy, (b) Time, (c) Size, and (d) Model cost.

HT+DDM performed similarly during the first 4,000 instances. Then, HT+DDM showed a slightly higher recovery rate accuracy than HAT+DDM. Fig. 2.8(b) presents the time comparison of the learners. We observe that HAT+SIS maintained a linear running time as the stream progressed. The model sizes of the three learners are shown in Fig. 2.8(c). It can be seen that the three learners demanded moderate memory. HAT+DDM and HT+DDM used the same model sizes, while HAT+SIS exhibited reduced peak memory demands. Fig. 2.8(d) shows the combined effect of the time and model size.

To evaluate the performance of the three learners in static and evolving data, we used a window performance evaluator for classification with a window size of 20, as shown in Fig. 2.9. The three learners presented the same accuracy during static data, represented by horizontal lines, reaching 100% accuracy. Evolving data manifests as an abrupt or gradual decrease in accuracy, displayed as downward peaks. HAT+SIS exhibited minor peaks during evolving data, especially around instance 4000, where HAT+DDM and HT+DDM exhibited significant accuracy degradation.

The performances of the three learners among the fifteen sets from the multiclass dataset are shown in Table 2.5. Considering the accuracy and Kappa statistic, HAT+SIS was the best performer among the fifteen sets, whereas HAT+DDM was the worst performer. Furthermore, HAT+SIS had the smallest running time, model size, and cost. Table 2.6 presents the mean and standard deviation of the metrics across the fifteen sets. The results indicate that the performance of HAT+SIS remained invariant among the sets while exhibiting the most accurate and precise performance.

Table 2.4: 15-fold average hyperparameter tuning of the HAT+SIS learner using the multiclass dataset in case study I.

Base Learner	Metrics	$r = 10$				$r = 5$				$r = 2$			
		$k = 4$	$k = 3$	$k = 2$	$k = 1$	$k = 4$	$k = 3$	$k = 2$	$k = 1$	$k = 4$	$k = 3$	$k = 2$	$k = 1$
	Accuracy	99.07	99.13	99.25	99.30	99.07	99.12	99.23	99.29	99.04	97.91	98.60	99.27
HAT	Kappa	99.04	99.10	99.23	99.27	99.03	99.09	99.20	99.27	99.00	97.83	98.55	99.24
+	Time	54.62	50.56	46.93	43.10	54.12	50.46	46.49	42.92	53.54	50.55	47.28	43.28
SIS	Size	195.83	195.82	195.82	195.82	195.82	195.82	195.82	195.82	195.82	195.82	195.82	195.82
	Cost	2.16	1.95	1.76	1.56	2.14	1.95	1.74	1.55	2.12	1.94	1.77	1.59

Table 2.5: Performance of the base learners for the 15 sets of the multiclass dataset in case study I.

Base Learner	Metric	Dataset														
		1	2	3	4	5	6	7	8	9	10	11	12	13	14	15
	Accuracy	99.25	99.29	99.32	99.31	99.30	99.27	99.29	99.30	99.33	99.37	99.31	99.31	99.30	99.30	99.30
HAT	Kappa	99.23	99.26	99.29	99.28	99.28	99.25	99.27	99.28	99.30	99.35	99.29	99.29	99.27	99.27	99.27
+	Time	40.95	42.27	44.57	43.51	42.10	41.38	43.19	43.89	44.03	45.54	43.31	42.63	43.36	42.05	43.73
SIS	Size	195.73	195.73	195.92	195.92	195.73	195.97	195.78	195.73	195.92	196.02	195.88	195.73	195.78	195.73	195.78
	Cost	1.48	1.53	1.61	1.57	1.52	1.50	1.56	1.59	1.59	1.64	1.56	1.54	1.57	1.52	1.58
	Accuracy	97.81	98.42	96.66	98.02	98.57	98.51	98.05	98.61	97.98	97.36	98.59	98.58	98.60	98.55	97.16
HAT	Kappa	97.73	98.37	96.53	97.94	98.52	98.46	97.98	98.55	97.89	97.25	98.54	98.53	98.54	98.50	97.04
+	Time	81.71	76.35	75.52	129.42	78.41	99.14	86.84	84.07	211.72	210.14	169.43	88.73	84.13	164.01	72.02
DDM	Size	214.34	217.94	228.26	221.93	220.38	214.81	223.03	224.87	226.26	231.94	223.19	222.14	224.54	219.10	224.17
	Cost	3.96	3.72	4.21	2.97	4.55	3.17	3.95	4.12	2.41	2.80	1.99	3.53	4.31	2.14	3.18
	Accuracy	98.03	98.42	97.67	98.21	98.57	98.51	98.17	98.61	97.98	97.86	98.59	98.58	98.60	98.55	97.82
HT	Kappa	97.96	98.36	97.58	98.14	98.52	98.46	98.10	98.55	97.89	97.78	98.54	98.53	98.54	98.50	97.73
+	Time	89.00	69.63	66.30	84.05	65.36	92.21	78.98	62.95	161.98	162.21	194.52	228.09	70.49	142.79	81.59
DDM	Size	213.68	217.12	227.43	220.94	219.38	213.65	222.03	223.88	225.10	230.94	222.37	221.14	223.54	217.94	223.18
	Cost	2.04	2.64	2.08	2.06	2.48	1.39	2.06	2.19	1.31	1.48	0.70	2.30	2.25	1.45	2.18

2.6.4 Case Study II: Ternary Events

In this case study, we used the three-class dataset to evaluate the performance of the proposed approach. The three-class dataset consisted of ternary events, that is, events labeled as natural, normal, and attack events. The attack events consisted of twenty-eight scenarios, the natural events consisted of eight scenarios, and the normal events consisted of one scenario. This section is important because the experiments assessed the efficacy of the proposed classifier in distinguishing normal operation from cyber and non-cyber contingencies in a cyber-physical power system.

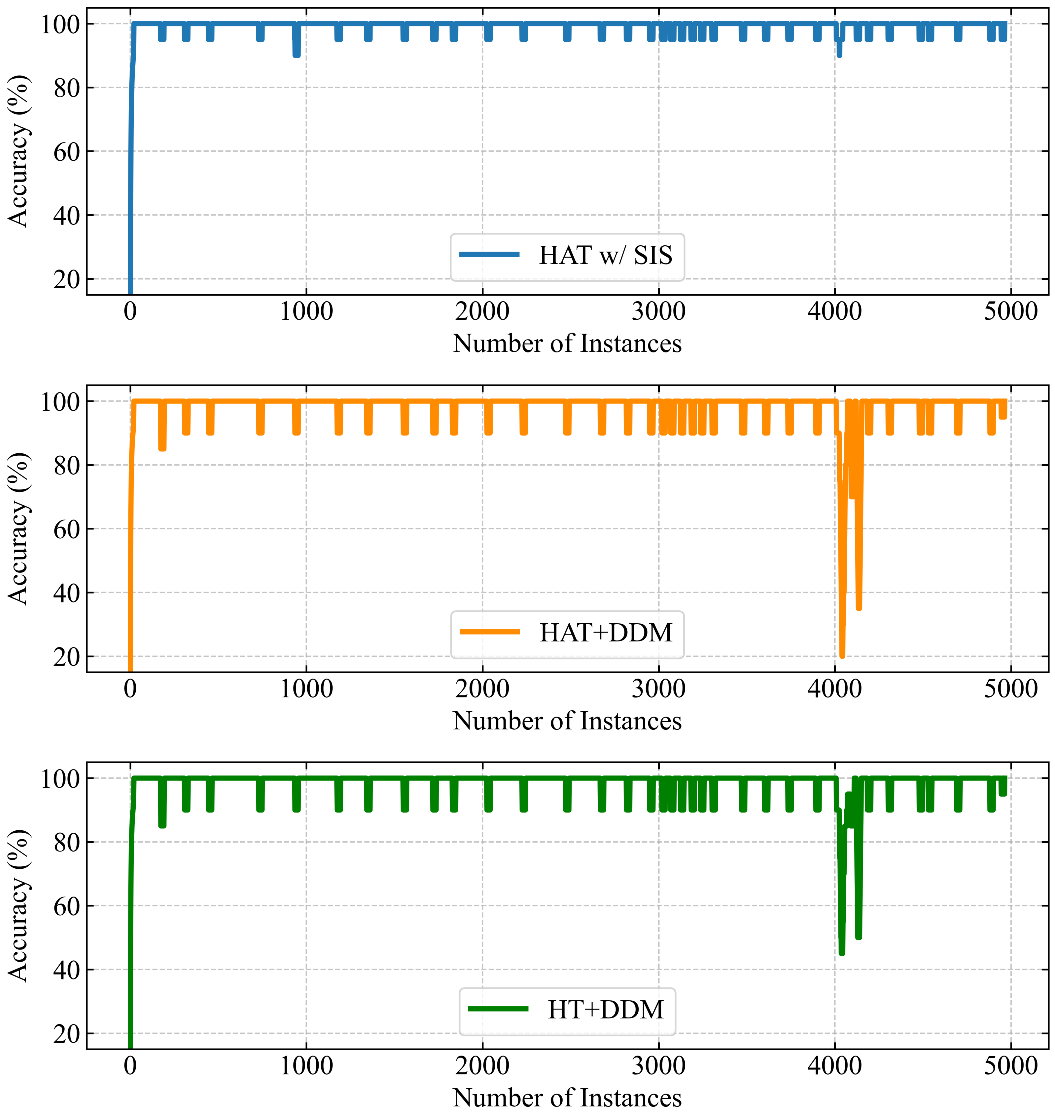

Figure 2.9: Performance evaluation of the base learners using the accuracy metric in dealing with stationary data and concept drift in case study I.

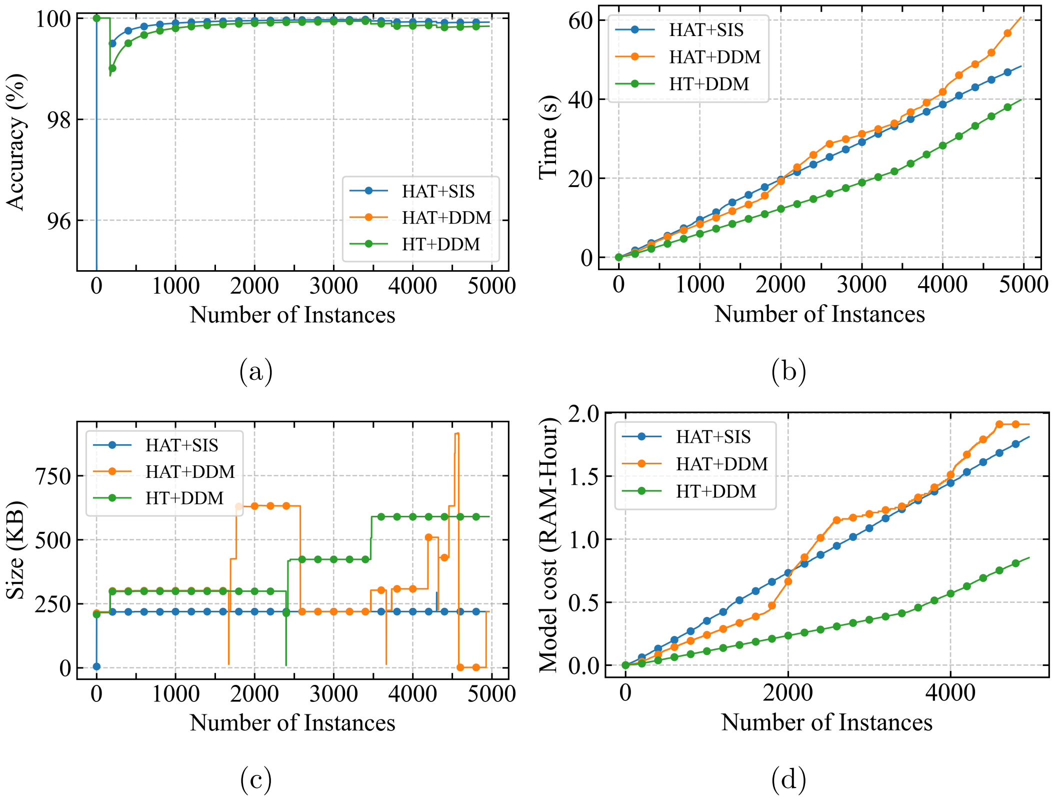

Figure 2.10: Performance comparison of the three learners in the case study II using the first set from the three-class dataset. The comparison is shown for the following metrics: (a) Accuracy, (b) Time, (c) Size, and (d) Model cost.

Table 2.6: The mean μ, standard deviation σ, minimum and maximum values of the performance metrics tested on the 15 sets of the multiclass dataset in case study I.

Learner	Metrics	Statistics			
		μ	σ	min	max
HAT + SIS	Accuracy	99.30	0.027	99.25	99.37
	Kappa	99.28	0.025	99.23	99.35
	Time	43.10	1.22	40.95	45.54
	Size	195.82	0.10	195.73	196.02
	Cost	1.56	0.044	1.48	1.64
HAT + DDM	Accuracy	98.10	0.62	96.66	98.61
	Kappa	98.02	0.64	96.53	98.55
	Time	114.11	49.97	72.02	211.72
	Size	222.46	4.73	214.34	231.94
	Cost	3.88	1.01	1.99	4.55
HT + DDM	Accuracy	98.28	0.33	97.67	98.61
	Kappa	98.21	0.35	97.58	98.55
	Time	110.01	53.52	62.95	228.09
	Size	221.49	4.71	213.65	230.94
	Cost	1.81	0.494	0.70	2.64

The hyperparameters of the SIS algorithm were the same as those in section 2.6.3 to alleviate the burden of hyperparameter tuning. Notice that the target space of the multiclass dataset is quite diverse and rich; hence, the best hyperparameters from section 2.6.3 benefited the HAT+SIS learner in this section.

Fig. 2.10 presents the performance of the three learners across the entire first set of the three-class dataset. Although HAT+SIS had a higher accuracy performance, the three learners showed a similar overall accuracy. HAT+SIS and HT+DDM exhibited a linear time complexity across the entire simulation, whereas the time complexity of HAT+DDM departed from being linear around instance 4000. Notably, HAT+SIS maintained a stable model size of less than 250 KB. HAT+SIS

Table 2.7: Performance of the three learners for the 15 sets of the three-class dataset in the case study II.

Learner	Metric	Dataset														
		1	2	3	4	5	6	7	8	9	10	11	12	13	14	15
HAT + SIS	Accuracy	99.92	99.92	99.93	99.92	99.92	99.92	99.92	99.92	99.91	99.93	99.92	99.92	99.92	99.92	99.92
	Kappa	99.77	99.82	99.83	99.84	99.82	99.81	99.80	99.82	99.80	99.83	99.79	99.84	99.78	99.80	99.85
	Time	48.30	107.90	77.53	50.55	106.75	59.33	47.50	48.08	48.36	49.69	47.41	46.58	47.14	45.49	47.79
	Size	219.15	219.15	219.33	219.33	219.15	219.38	219.19	219.15	219.33	219.43	219.29	219.15	219.19	219.15	219.19
	Cost	1.81	1.64	1.86	1.89	1.83	1.65	1.77	1.79	1.80	1.86	1.77	1.74	1.76	1.70	1.78
HAT + DDM	Accuracy	99.83	99.84	99.85	99.84	99.84	99.83	99.84	99.84	99.85	99.85	99.84	99.84	99.84	99.84	99.84
	Kappa	99.54	99.65	99.66	99.68	99.64	99.63	99.61	99.65	99.69	99.67	99.60	99.68	99.57	99.60	99.70
	Time	60.66	50.56	47.04	38.88	131.88	44.34	107.68	95.40	105.95	102.29	60.19	63.46	50.96	40.81	57.01
	Size	219.11	219.11	219.30	643.12	302.82	303.37	219.19	219.45	303.20	637.85	302.98	219.19	219.27	219.19	224.85
	Cost	1.16	1.43	1.45	1.39	1.59	1.45	1.06	2.01	1.24	1.29	1.77	1.56	1.70	1.51	1.29
HT + DDM	Accuracy	99.82	99.83	99.85	99.84	99.83	99.83	99.84	99.84	99.83	99.83	99.84	99.84	99.84	99.84	99.82
	Kappa	99.52	99.65	99.64	99.68	99.64	99.62	99.61	99.63	99.69	99.65	99.60	99.68	99.59	99.61	99.69
	Time	39.80	39.65	47.98	49.67	40.65	49.98	60.93	54.88	53.51	58.89	33.26	42.12	40.00	40.12	47.59
	Size	590.28	921.81	716.03	585.08	509.08	1000.06	801.64	316.01	428.12	1000.14	224.06	636.65	717.90	513.86	980.01
	Cost	0.85	0.83	1.01	1.13	0.87	0.03	1.19	0.72	1.04	0.61	0.67	0.85	0.82	0.83	1.02

showed a linear model cost during the simulation, whereas HT+DDM had the lowest cost. Table 2.7 presents the metrics of the three learners for the 15 sets of the three-class dataset. We observe that the accuracy and Kappa metrics were not significantly different between HAT+SIS and the other two learners. Table 2.8 presents the four statistics computed from the performance metrics of the fifteen sets.

2.6.5 Case Study III: Binary Events

We conducted the experiments in this case study using the two-class dataset corresponding to only two events, normal operation, and attack events. Binary classification is essential because it allows us to test whether our proposed classifier can detect deviations from normal cyber-physical system behavior. We set the hyperparameters of the SIS algorithm as $r = 10$ and $k = 1$, as described in section 2.6.4. Fig. 2.11 presents the performance of the three learners across the entire first set of the two-class dataset. HAT+DDM and HT+DDM showed similar accuracy across the experiment, whereas HAT+SIS had slightly higher accuracy. HAT+SIS

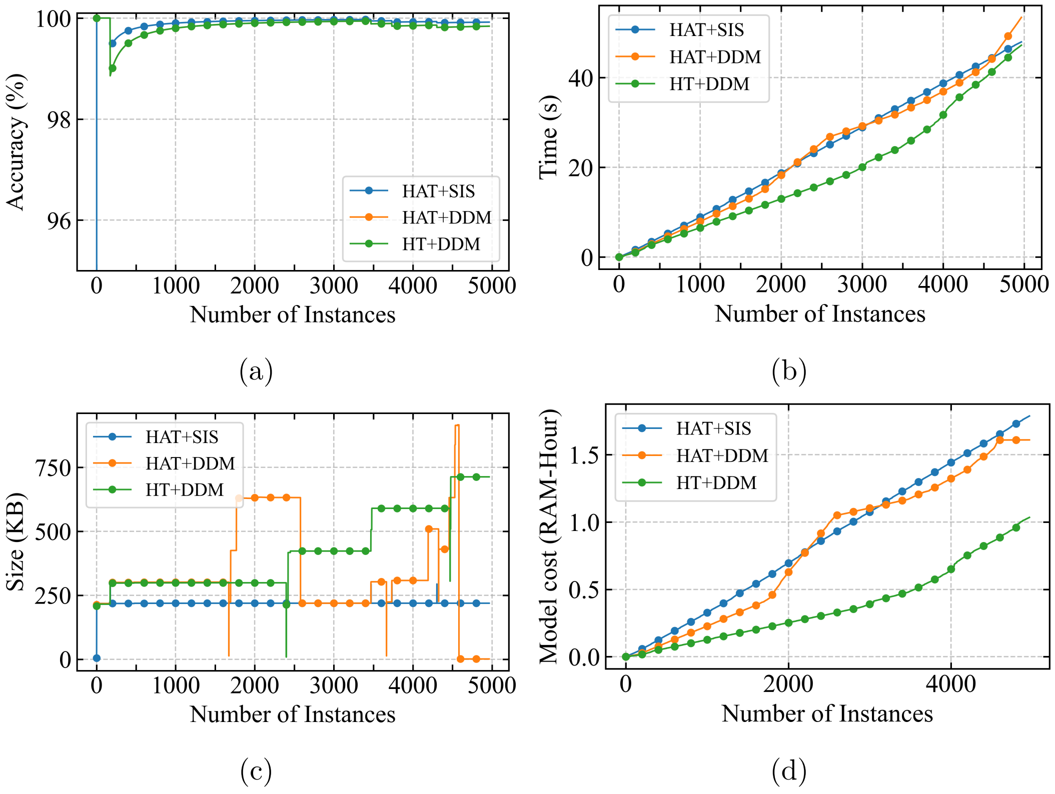

(a)

(b)

(c)

(d)

Figure 2.11: Performance comparison of the three learners in the case study III using the first set from the two-class dataset. The comparison is shown for the following metrics: (a) Accuracy, (b) Time, (c) Size, and (d) Model cost.

Table 2.8: The mean μ, standard deviation σ, minimum and maximum values of the performance metrics tested on the 15 sets of the three-class dataset in the case study II.

Learner	Metrics	Statistics			
		μ	σ	min	max
HAT + SIS	Accuracy	99.92	0.004	99.91	99.93
	Kappa	99.81	0.023	99.77	99.85
	Time	58.56	21.35	45.49	107.90
	Size	219.23	0.099	219.15	219.43
	Cost	1.77	0.072	1.64	1.89
HAT + DDM	Accuracy	99.84	0.005	99.83	99.85
	Kappa	99.63	0.046	99.54	99.70
	Time	70.47	29.72	38.88	131.88
	Size	298.13	143.85	219.11	643.12
	Cost	1.46	0.246	1.06	2.01
HT + DDM	Accuracy	99.83	0.005	99.82	99.85
	Kappa	99.61	0.046	99.52	99.69
	Time	46.60	8.062	33.26	60.93
	Size	662.71	245.82	224.06	1000.14
	Cost	0.831	0.275	0.03	1.19

and HAT+DDM exhibited a linear time complexity during the entire simulation. HT+DDM had the smallest time complexity, but it showed a moderate increase at the end of the experiment. HAT+SIS maintained a stable model size of approximately 250 KB overall, whereas HT+DDM had step increases in its model size. The three learners exhibited a model cost behavior similar to their processing time behavior. Table 2.9 presents the performance of the three learners for the 15 sets of the two-class dataset. In this table, we observe that HAT+SIS was the best performer in terms of accuracy, Kappa, and model size metrics. Table 2.10 shows the four statistics calculated using the results of the 15 sets of the two-class dataset. HAT+SIS had a small standard deviation for all metrics except the processing time.

Table 2.9: Performance of the base learners for the 15 sets of the two-class dataset in the case study III.

Base Learner	Metric	Dataset														
		1	2	3	4	5	6	7	8	9	10	11	12	13	14	15
	Accuracy	99.92	99.92	99.93	99.92	99.92	99.92	99.92	99.92	99.91	99.93	99.92	99.92	99.92	99.92	99.92
HAT	Kappa	99.76	99.81	99.82	99.83	99.81	99.80	99.79	99.81	99.78	99.82	99.79	99.82	99.77	99.79	99.83
+	Time	47.93	61.16	73.72	58.23	59.80	63.59	66.99	66.31	87.75	68.56	49.86	47.41	47.75	46.43	47.70
SIS	Size	219.15	219.15	219.33	219.33	219.15	219.38	219.19	219.15	219.33	219.43	219.29	219.15	219.19	219.15	219.19
	Cost	1.78	1.94	2.05	1.90	1.93	1.72	1.89	2.09	2.05	2.17	1.84	1.77	1.78	1.73	1.78
	Accuracy	99.83	99.84	99.85	99.84	99.84	99.83	99.84	99.84	99.85	99.85	99.84	99.84	99.84	99.84	99.84
HAT	Kappa	99.53	99.62	99.64	99.66	99.62	99.61	99.59	99.63	99.66	99.65	99.58	99.65	99.55	99.59	99.66
+	Time	47.18	45.35	44.38	39.27	45.37	40.77	55.28	63.65	63.16	42.18	47.60	44.93	49.09	44.93	42.40
DDM	Size	230.15	219.72	219.88	646.82	303.4	303.95	219.79	250.07	303.77	641.55	303.56	219.8	219.84	219.77	226.45
	Cost	1.16	1.46	1.16	1.18	1.39	1.30	0.95	1.78	1.17	1.22	1.57	1.35	1.41	1.45	1.26
	Accuracy	99.83	99.84	99.85	99.84	99.84	99.83	99.84	99.84	99.85	99.85	99.84	99.84	99.84	99.84	99.84
HT	Kappa	99.53	99.62	99.64	99.66	99.62	99.61	99.59	99.63	99.66	99.65	99.58	99.65	99.55	99.59	99.66
+	Time	47.20	72.72	145.43	61.02	53.41	60.75	94.13	61.34	69.95	93.46	39.75	45.31	62.78	211.67	93.56
DDM	Size	713.02	921.78	716.03	875.39	717.87	814.12	801.64	735.29	842.32	333.45	224.06	636.65	717.99	921.76	432.83
	Cost	1.03	0.88	1.01	1.22	0.96	1.29	1.24	0.79	1.16	0.81	0.78	0.92	0.82	0.81	0.88

2.6.6 Case Study IV: Loading Variations

We tested the three learners in this case study to classify a fault event under different loading conditions. We simulated a data stream with three stages in this order: (i) fault from $10 - 19\%$ on line 2; (ii) the fault is cleared, returning the system to normal operation; and (iii) fault from $10 - 19\%$ on line 2. Stages (i) and (iii) were considered to have distinct loads in the system. The confusion matrices are shown in Fig. 2.12. HAT+SIS accounted for the largest number of correct predictions, whereas HT+DDM accounted for the smallest. Although HAT+SIS correctly classified the instances from the normal operation event, it shows the largest misclassification rate for the fault event. HAT+DDM and HT+DDM exhibited excellent performance in classifying the fault event. However, these performers did not exhibit attractive performance for normal event classification.

Table 2.10: The mean μ, standard deviation σ, minimum and maximum values of the performance metrics tested on the 15 sets of the two-class dataset in the case study III.

Learner	Metrics	Statistics			
		μ	σ	min	max
HAT + SIS	Accuracy	99.92	0.004	99.91	99.93
	Kappa	99.80	0.021	99.76	99.83
	Time	59.54	12.03	46.43	87.75
	Size	219.23	0.099	219.15	219.43
	Cost	1.89	0.141	1.72	2.17
HAT + DDM	Accuracy	99.84	0.005	99.83	99.85
	Kappa	99.61	0.040	99.53	99.66
	Time	47.70	7.40	39.27	63.65
	Size	301.90	143.50	219.72	646.82
	Cost	1.32	0.201	0.95	1.78
HT + DDM	Accuracy	99.84	0.005	99.83	99.85
	Kappa	99.61	0.040	99.53	99.66
	Time	80.83	44.96	39.75	211.67
	Size	693.61	208.85	224.06	921.78
	Cost	0.973	0.177	0.78	1.29

2.6.7 Case Study V: PMU Disappearance

Consider a monitoring system consisting of four PMUs whose measurements are modeled as features. After some time, one of the PMUs gets disconnected from the system. Such a situation can be modeled as a feature disappearance drift, which may occur owing to a communication bottleneck, malfunctioning, or physical attack on the device. We simulated this scenario using a data stream consisting of 1450 instances with line maintenance, remote tripping commands, and fault events on both lines and different locations within the lines. Fig. 2.13 shows the results for the three learners in case study V with PMU's disappearance at instance 500. According

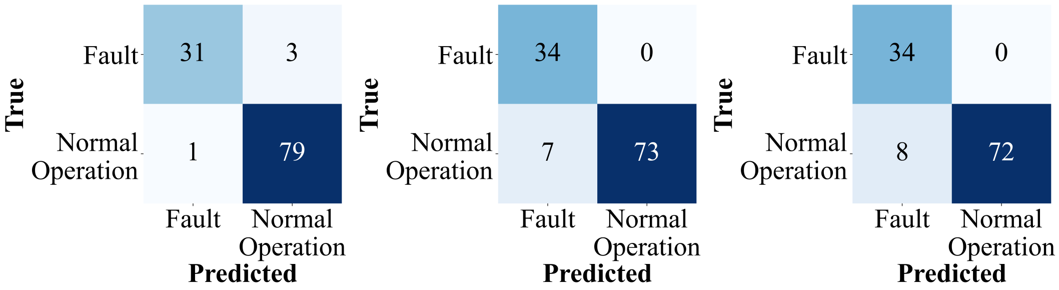

(a) (b) (c)

Figure 2.12: Confusion matrices of the three learners in case study IV. (a) HAT+SIS, (b) HAT+DDM, (c) HT+DDM

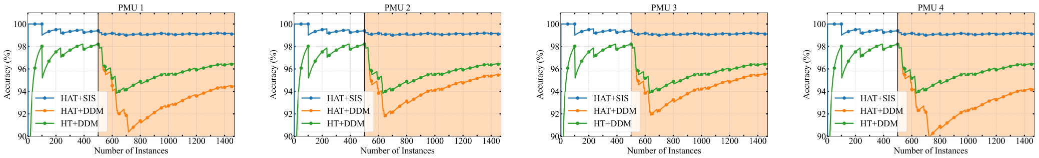

Figure 2.13: Accuracy of the three learners in case study V. The vertical black bar indicates the instance at which one of the PMUs disappears in the data stream. The light orange shaded area corresponds to the portion of the data stream where the PMU is inactive, whereas the uncolored area corresponds to the data stream where the PMU is active.

to the results, HAT+SIS exhibited the best performance.

2.6.8 Case Study VI: Measurements Overlapping

Some cyber-attacks may exhibit similar class conditional measurements distribution $P(X|Y)$ as fault disturbances. In other words, cyber-attacks and faults may fall into the same region of the measurements (features) space. This situation makes it difficult for learners to discriminate between similar events. In this scenario, we studied one fault disturbance and two cyber-attacks: (i) fault from $80-90\%$ on line 1, and (ii) a data injection attack that mimics a fault from $80-90\%$ on line 1 with a remote tripping command; and (iii) a fault from $80 - 90\%$ on line 1 with relay #2 disabled. First, we forced the learner to process a data stream from disturbance (i), followed by an abrupt concept change in the data distribution corresponding to cyber-attacks (ii) or (iii). Then, we made the learner learn oppositely, that is, a cyber-attack (ii) or (iii), followed by the fault disturbance in (i). Fig. 2.14 shows the accuracy of the three learners under case study VI of measurements overlapping. HAT+SIS was less vulnerable to abrupt changes in the data distribution. In Figs. 2.14(a) and 2.14(c), the three learners exhibited similar accuracies when they first process instances from the fault distribution. However, their accuracy performance differed if they start processing instances from the cyber-attack distribution, as seen in Figs. 2.14(b) and 2.14(d). The results indicate that HAT+SIS performed best in this case study because it can correctly classify instances from data injection and remote tripping attacks.

2.6.9 Price Forecasting Dataset

Table 2.11: Hyperparameter tuning of the HAT+SIS learner using the price forecasting Elec2 dataset.

Base Learner	Metrics	$r = 10$				$r = 5$				$r = 2$			
		$k = 4$	$k = 3$	$k = 2$	$k = 1$	$k = 4$	$k = 3$	$k = 2$	$k = 1$	$k = 4$	$k = 3$	$k = 2$	$k = 1$
HAT + SIS‘	Accuracy	85.840	85.88	86.130	85.42	85.71	85.76	85.95	85.41	85.66	77.61	81.25	85.440
	Kappa	71.051	71.12	71.629	70.15	70.78	70.88	71.27	70.14	70.68	54.03	61.64	70.191
	Time	197.31	178.96	155.11	128.02	193.80	176.87	155.15	131.57	188.79	165.12	147.54	131.83
	Size	23.45	23.45	23.45	23.03	23.45	23.45	23.45	23.03	23.45	23.45	23.38	23.03
	Cost	1.01	0.89	0.74	0.57	0.98	0.87	0.73	0.58	0.95	0.80	0.68	0.588

This section used a dataset outside the cyber-attack and disturbance domain to further assess the merits of our proposed approach. We conducted the

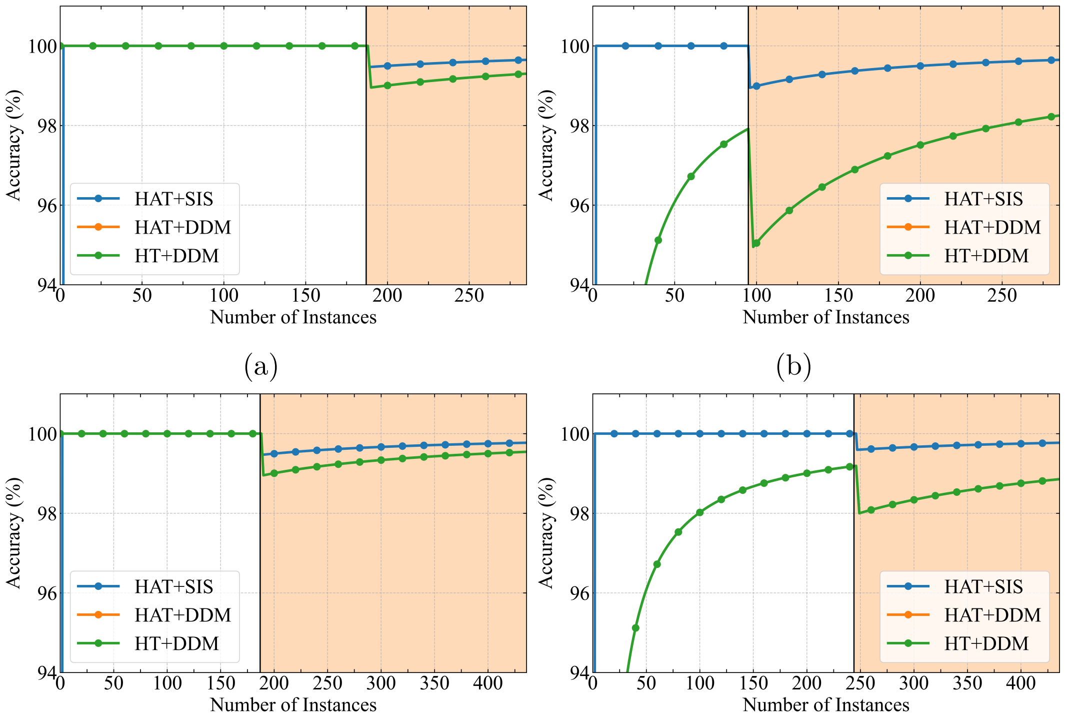

(a)

(b)

(c)

(d)

Figure 2.14: Accuracy of the three learners in case study VI. The vertical black bar indicates the instance at which the abrupt change in the data stream occurs. The white-shaded area corresponds to the portion of the stream under a fault disturbance distribution, whereas the light orange-shaded area corresponds to a cyber-attack distribution. (a) and (b) for fault disturbance and remote tripping command events; (c) and (d) for fault disturbance and relay #2 disabled. The performance of HAT+DDM and HT+DDM is the same in this scenario.

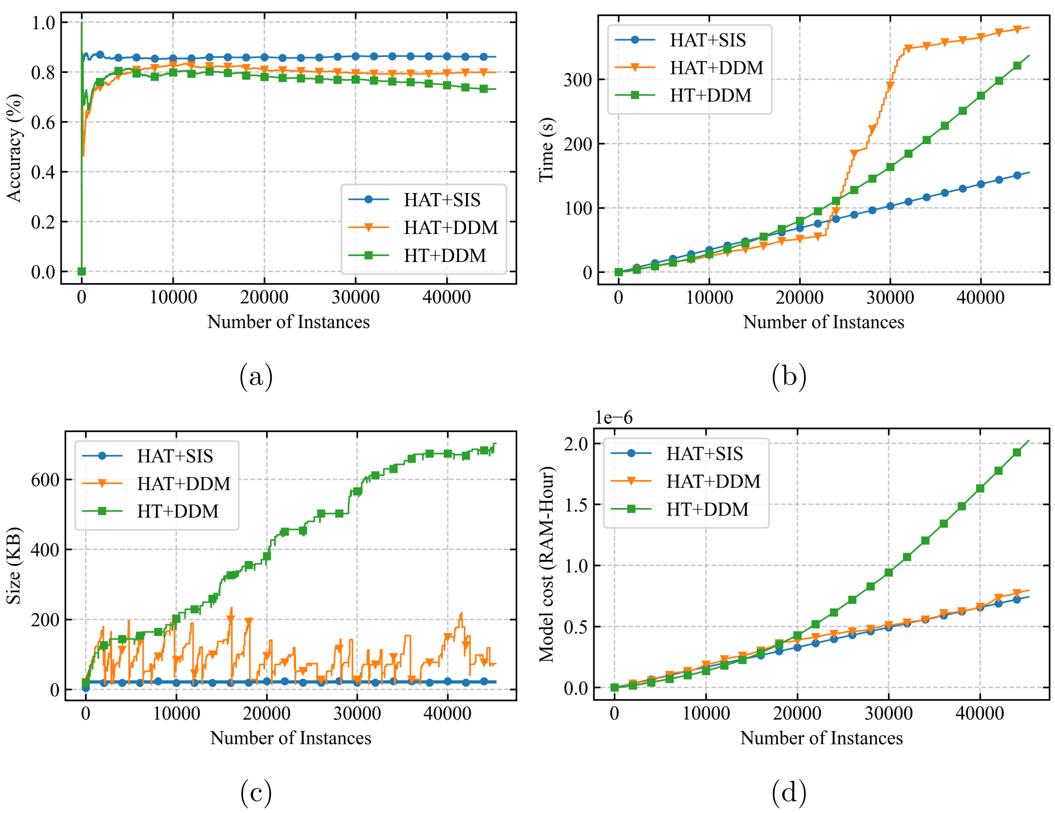

(a) (b)

(c) (d)

Figure 2.15: Performance comparison of the three learners using the price forecasting Elec2 dataset. The comparison is shown for the following metrics: (a) Accuracy, (b) Time, (c) Size, and (d) Model cost.

following experiments with the price forecasting Elec2 dataset based on the electricity price market in the Australian state of New South Wales [48]. The Elec2 dataset contains 45312 instances drawn between May 7th, 1996, and December 5th, 1998, with a sampling resolution of one instance for each half-hour. The market prices are set by matching the electricity demand with the cheapest combination of energy generation from all power stations. Electricity market data is subject to concept drifts because the market is affected by different factors such as weather, time of the day, season, and other factors, that is, the energy prices are not stationary. The dataset

Table 2.12: Performance of the base learners using the price forecasting Elec2 dataset.

Base Learner	Accuracy	Kappa	Time	Size	Cost
HAT + SIS	86.13	71.62	155.11	23.45	0.74
HAT + DDM	79.87	58.63	380.82	73.62	0.71
HT + DDM	73.20	43.95	339.18	702.62	2.05

has eight features including electricity demand and price schedules. The class labels are set as UP or DOWN depending on whether the current electricity price is higher or lower than the average price over the previous 48 instances (or the previous 24 hours).

The hyperparameters of SIS, r and k, were tuned using a grid search, as shown in Table 2.11. The best performance is obtained by setting $r = 10$ and $k = 2$. A finer grid search is left for future studies. Fig. 2.15 shows the performance of the three learners across the entire dataset. HAT+SIS was the best performer overall, whereas HT+DDM has the worst performance. HAT+DDM and HT+DDM exhibited a nonlinear increasing time complexity of approximately half of the dataset, whereas HAT+SIS showed a linear time complexity. HAT+SIS had the smallest model size during the entire simulation, whereas the model size of HT+DDM increased linearly. HT+DDM showed nonlinear behavior for the model cost, similar to its time complexity. HAT+SIS and HAT+DDM exhibited linearly increasing model cost. From Table 2.12, we observe that HAT+SIS outperformed HAT+DDM by 6% and HT+DDM by 12% in terms of accuracy. HAT+SIS required at least half the processing time and model size of the other two learners. The model cost of HAT+SIS was similar to that of HAT+DDM but less than twice that of HT+DDM.

In Table 2.13, we compared the classification accuracy of the HAT+SIS learner and other similar algorithms. Noticeably, we can observe that the HAT+SIS method outperformed existing algorithms for classifying disturbances and cyber-attacks. The reported results for the HAT+SIS, HAT+DDM, and HT+DDM learners were based on the average accuracy among the fifteen sets from the multiclass dataset presented in Table 2.6.

Table 2.13: Accuracies of HAT+SIS and other adaptive classifiers on the Attack dataset reported in the literature.

Algorithm	# of classes	Accuracy
Common Path Mining [49]	7	93.00
NNGE+STEM [17]	41	93.00
HAT+DDM [26]	41	92.00
Weights Voting Algorithm [50]	37	92.40
SSHAD [51]	37	96.84
Tree-based GBFS [27]	37	92.46
HAT+DDM	37	98.10
HT+DDM	37	98.28
HAT+SIS	37	**99.30**

2.7 Discussion

We use a testbed architecture of three buses with PMUs placed on the ends of the two lines. If the test bed is a more extensive network, we may need to consider a specific PMU placement strategy for the proposed approach. Such a strategy will place PMUs in areas defined by clusters of buses that share the same dynamic behavior, reducing the overall number of PMUs [52]. The dataset considered in this work contains events from dynamic transients such as three-phase short circuits, line outages, load variations, and breaker tripping. For instance, placing a PMU in a region where a subset of the system's buses exhibits similar behavior under a short circuit and line outages is sound. A drawback of this strategy is that it may be challenging for the classifier to identify where an event occurs among the buses of the same cluster. Moreover, a tradeoff between the number of clusters and the cost of PMU deployment must be considered.

The 37 events in the dataset allow us to judge the efficacy of any classifier, and a classifier that exhibits a remarkable performance using such events can be judged as a noteworthy classifier. Although the numerical results show that our proposed classifiers exhibit a higher accuracy than other existing classifiers, we know that the set of events is not exhaustive. We acknowledge that different events can be considered to strengthen our proposed approach. For instance, we can include denial of service attacks such as data flooding, mutation of MODBUS protocol, or aurora attacks that refer to opening and closing a breaker near a generator in a rapid sequence.

The learner must exhibit a fast time response for the event and intrusion detection task. As mentioned in section 2.3, ICS datasets are built using high-speed networking and PMU data. PMUs have a very high data rate because they transmit tens or hundreds of synchrophasors per second through the networking architecture. Such a situation forces the learner to make predictions within a concise amount of time. In addition, the available working memory is not abundant, particularly for PMUs or phasor data concentrators (PDC). According to numerical results, our two methods process approximately 5,000 instances in about 43 seconds with a minimal burden in memory consumption. Existing PMUs or PDCs on the market can handle such time and memory demands. Hence, our proposed approaches are suitable for PMU data-based contingency detection.

2.8 Summary

We develop two novel methods based on adaptations of the HAT classifier for power systems event detection. The first method leverages online dictionary learning techniques to automatically build a new feature space for the labeled data examples by extracting valuable information from the unlabeled dataset. The learned sparse codes of the labeled instances become the new feature representations based on which we train the HAD classifier. The numerical results corroborate the effectiveness of the first method, yielding a better classification performance and compensating for the additional computational burden of learning the higher dimensional representations.

The second method incorporates an instance selection algorithm that improves HAT capabilities and comprises three algorithmic stages: reordering, resetting, and searching. The first stage uses a spatiotemporal distance function to measure the similarity of a set of observations with the target instance. The distance function uses an adaptive feature weight for the PMU measurements with different scales. The second stage reinitializes the parameters of HAT to allow the tree to adapt to the current concept underlying the data distribution. The third stage greedily searches the optimal size of a sliding window by identifying the instances most similar to the target instance. Extensive numerical results demonstrate that the novel combination of HAT with the SIS algorithm outperforms the first method and other existing classifiers in the literature, especially for multiclass classification.

This study demonstrates that the proposed methods apply to real-time scenarios in CPPS, are sensitive to cyber and non-cyber contingencies, and show superior performance over the competitors.

Chapter 3

Fault detection for grid-forming inverters

The introduction of converter-interfaced power generation has successfully integrated renewable energy sources into small-scale power systems, such as microgrids [53] [54]. Microgrids can operate in two modes: grid-connected or islanded. In the grid-connected mode, a microgrid relies on the main grid for voltage and frequency regulation, which benefits from its upstream protection. On the other hand, an islanded microgrid functions as an independent system and must independently maintain reference voltage magnitude and frequency for its components. Consequently, ensuring stability in the islanded mode is more challenging than in the grid-connected mode [10]. In addition, independent microgrids face risks to their stability during abnormal events, such as internal faults, which can result in significant imbalances between energy demand and supply. These imbalances can lead to partial power outages or blackouts.

Furthermore, when an islanded microgrid disconnects from the main power system, the fault current strength decreases, which helps mitigate the decline in voltage magnitude and frequency following a severe event [55]. This situation is exacerbated when the power generators are grid-forming inverters, as they reduce the available electrical inertia in the system [11]. It is crucial to have intelligent fault detection (FD) that is resilient against disturbances and sensitive to faults to ensure stable microgrid performance and prevent interruptions in energy supply.

This chapter presents two fault detection strategies for grid-forming inverters (GFMs) with power-sharing coordination. The first strategy is based on observers and residuals for detecting internal faults in grid-forming inverters with fixed thresholding. The design of our observers and residuals considers H_-/H_∞ conditions to ensure robustness against disturbances and responsiveness to busbar, actuator, and inverter bridge faults. The proposed design is less restrictive than existing observer-based fault detection schemes by leveraging the properties of quadratic inner-boundedness and one-sided Lipschitz conditions. The second strategy presented in this chapter consists of a residual-based adaptive threshold for detecting faults in grid-forming inverters. The adaptive threshold response is evaluated using unwanted events such as busbar and sensor faults. An inequality for the upper bound on the ℓ_2 norm of the residual is derived and used for designing the adaptive threshold. The upper bound is obtained via semidefinite programming with two linear matrix inequality constraints. In both sections, the inverters are modeled as a nonlinear system with one-sided Lipschitz nonlinearities and modeling uncertainties. Also, the inverters are studied while operating in AC microgrids islanded from the primary grid.

$\mathbb{R}$ denotes the set of real numbers. Symbol $\times$ denotes the Cartesian product. Bold letters represent vectors. $\|\mathbf{a}\|$ is the ℓ_2-norm of the vector while $\|\mathbf{a}\|_{[0,t]} := \sqrt{\int_0^t \|\mathbf{a}\|_2^2 \, dt}$ is the ℓ_2-norm up to time t. $A \succ 0$ indicates that matrix A is positive definite. $\langle \mathbf{a}, \mathbf{b} \rangle$ represents the dot product between vectors $\mathbf{a}$ and $\mathbf{b}$. $\mathbf{a}^\top$ is the transpose of vector $\mathbf{a}$.

3.1 Literature review

In general, fault detection algorithms for power converters can be categorized as data-driven, signal-processing, and model-based techniques. *Data-driven techniques* rely on various system measurements to extract fault signatures, thereby implementing fault diagnosis with intelligent algorithms [56–62]. In [56], the authors combine the information change in SCADA data with a recurrent neural network (RNN) to compute a residual and adaptive threshold for fault detection in inverters for wind turbines. In [57], a new spatio-temporal multiscale neural network provides an end-to-end fault diagnosis for wind turbines using imbalanced SCADA data. The approach uses multiple thresholding to isolate faults. The authors in [58] design a fixed threshold and a novel fault diagnostic method for three-phase multilevel converters using 2-D convolutional neural networks and a window-based feature extraction technique. Another approach presented in [59] combines a short-time wavelet entropy calculation method with long short-term memory networks (LSTM) and support vector machines (SVM) for fault detection in multilevel converters. In [60], the authors propose a convolutional neural network (CNN) for fault diagnosis of open-circuit failure in three-phase inverters with multiple thresholds. Despite the merits of these works, data-driven models usually suffer from issues such as high computational burden, low interpretability, complicated weights initialization, and sensitivity to input data.

Signal processing-based methods have effectively identified fault signatures using non-parametric techniques without an accurate system model and by sampling voltage, current, or auxiliary signals. However, these techniques are often limited to specific conditions and scenarios [63–65]. Another approach involves utilizing signal patterns and local measurements near the generation units to create a dependable fault detection module [66–68]. Nevertheless, these strategies may require additional hardware and incur additional costs. In addition to these techniques, model-based methods are employed for fault detection when a system model is available. These methods have gained popularity due to their reliance on the physical relationships governing system dynamics. Among the model-based approaches, observer-based methods have garnered significant interest due to their fast detection capabilities, cost-effectiveness, and the availability of powerful tools for observer design [69–73].

Model-based methods are appropriate when the systems under study can be modeled accurately [71, 74–79]. In [74], the authors propose an adaptive fast voltage-based detection method for open-switch faults with an adaptive threshold. However, the technique is sensitive to noise in measured currents. A detection method with an adaptive threshold is designed for open-circuit faults using a phase voltage vector residual [75]. Nonetheless, the approach has a narrow diagnosis time. The authors in [76] use a combination of a current observer, filter circuits, and an adaptive threshold to detect open-switch faults of voltage source inverters. In [77], high-fidelity model-based detection and isolation filters are employed for open-circuit and current sensor faults. However, the method is sensitive to communication latency. References [71, 78] leverage H_{-}/H_{∞} optimization to design fault detection filters with fixed thresholds for busbar and line faults for inverter-based resources. The methods, however, are limited to system-level solutions that do not scale. In [80], the authors present a model-based method for designing adaptive thresholds for fault detection. However, the designed threshold is limited to linear systems, has a narrow adaptive operation, and does not consider the control input for its computation. The authors in [81] propose a superimposed phase-current scheme with a voltage restraint element to detect faults in an islanded microgrid with grid-forming inverters. Although the method correctly identifies faults, the speed of detection is considerable.

In [70], the authors propose a nonlinear observer for a grid-connected photovoltaic (PV) circuit that monitors unmodeled fault signatures to detect output deviations that could indicate the presence of a fault. However, their study does not account for disturbances and uncertainties in the system parameters. [71] presents an improved fault detection and identification method using $\mathcal{H}_{-}/\mathcal{H}_{\infty}$ optimization, which can effectively handle various component faults. However, their study focuses on DC microgrids with a linear state-space model. Anagnostou et al. [72] develop a time-varying observer for predicting the states of synchronous machines. Their approach linearizes the model at each time step, increasing computational complexity while not considering model uncertainties and disturbances. [73] introduces a constrained minimization program with linear matrix inequality (LMI) constraints and $\mathcal{L}_-/\mathcal{L}_\infty$ performance indices to detect faults in a microgrid comprising synchronous machines. They utilize a Lipschitz equivalent nonlinear model. Their study neglects parametric uncertainties and the influence of faults on the nonlinear function in the state transition model. Moreover, the restrictiveness of the Lipschitz condition is not addressed.

The primary limitation of fault detection strategies based on the Lipschitz condition for nonlinear systems is their susceptibility to the Lipschitz constant, resulting in conservative observer designs [82, 83]. In [82], an observer design problem is introduced for nonlinear systems that take into account the quadratic innerboundedness (QB) and one-sided Lipschitz (OL) conditions. [83] presents reduced- and full-order observer designs for nonlinear systems satisfying the QB and OL conditions, incorporating the Ricatti equation. However, these previous works do not specifically focus on fault detection nor consider the robustness against disturbances and the responsiveness to faults.

From the review of the prior works, an internal fault detection solution for grid-forming inverters operating in islanded AC microgrids that is robust against disturbances and exhibits a fast detection response is still missing. To fill this gap, we develop two model-based fault detection strategies that do not require additional sensors. The strategies use nonlinear observers to produce a residual signal, which is compared against a fixed or adaptive threshold that evolves according to the input dynamics of the grid-forming inverter. We derive the mathematical model of the grid-forming inverter considering the state space framework while considering external disturbances and parametric uncertainties. Based on the inverter model, we select a nonlinear $\mathcal{H}_\infty/\mathcal{H}_-$ observer to compute the discrepancy between the output of the grid-forming inverter and the model's output. Finally, we study the performance of our design considering four types of internal faults with modeling errors, nonlinear loads, and input delays.

3.2 Contributions

Protecting grid-forming inverters against internal faults is essential for improving islanded AC microgrids' transient stability and operation. The low inertia characteristic of the inverters makes fault currents increase at high rates. Such a situation demands fast fault detection and clearance of a few milliseconds. Otherwise, severe and permanent harm may occur to the inverter and microgrid components. Considering the limitations of prior works, the main contributions of our work are summarized as follows.

1. We demonstrate the successful application of nonlinear observers designed with

$\mathcal{H}_-/\mathcal{H}_\infty$ optimization for fault detection in grid-forming converters (GFM) connected to islanded AC microgrids with fixed and adaptive thresholds. The proposed strategies exhibit robustness against disturbances and responsiveness to faults.

2. We thoroughly investigate the relationship between the observer designs based on Lipschitz conditions and the proposed design based on the one-sided Lipschitz (OL) and quadratic inner-boundedness (QB) conditions.

3. We derive a deterministic matrix representation for various types of faults affecting GFMs. Our analysis considers the influence of parametric uncertainties and disturbances on the system model, including the nonlinear function in the state transition equation.

4. Utilizing a nonlinear observer offers the advantage of performing the one-time computation of the observer's gain offline. In contrast, a linearized observer design increases the time complexity by recalculating the observer gain at each time step [72]. Unlike the Lipschitz-based observer design in [73], the OL and QB conditions allow for a less restrictive observer design, avoiding the observer's sensitivity to the Lipschitz constant.

5. Our proposed methods also possess a crucial advantage in that they can be implemented with the two most commonly used practical control techniques: droop control and virtual synchronous machine control. While this work primarily focuses on detecting internal faults in grid-forming inverters, we believe

that our observer design can be easily adapted to detect internal faults in grid-following inverters, given the similar dynamics shared by both technologies. These advantages greatly enhance our proposed method's value for real-world applications.

6. The proposed method with adaptive threshold exhibits fast fault detection and clearance response times, minimizing to zero the false alarm and missed detection rates for the faults considered in this study.

3.3 Preliminaries

3.3.1 Observers for nonlinear dynamic systems

The state-space representation of a nonlinear system in the absence of disturbances and faults can be typically expressed as

$$\begin{cases} \dot{\mathbf{x}} = A\mathbf{x} + B\mathbf{u} + \boldsymbol{\phi}(\mathbf{u}, \mathbf{x}) \\ \mathbf{y} = C\mathbf{x} + D\mathbf{u} \end{cases}, \tag{3.1}$$

where $\boldsymbol{y}$ represents the measurement vector, $\boldsymbol{x}$ is the state vector, $\boldsymbol{u}$ the inputs vector, and function $\boldsymbol{\phi}(\mathbf{x}, \mathbf{u})$ captures nonlinearity of the system. The parametric matrices A, B, C, and D are formed according to the equations that govern the system. We further define two convex sets $\mathcal{D}$ and $\mathcal{U}$ that make up the feasible operating region of the system. They are the Cartesian products of all intervals formed by the maximum and minimum limits of the entire control inputs and states, respectively [84]

$$\mathcal{D} = [x_1^{\min}, x_1^{\max}] \times \cdots \times [x_n^{\min}, x_n^{\max}],$$

$$\mathcal{U} = [u_1^{\min}, u_1^{\max}] \times \cdots \times [u_p^{\min}, u_p^{\max}].$$

A Luenberger observer of the nonlinear system is defined as follows

$$\begin{cases} \dot{\hat{\mathbf{x}}} & = A\hat{\mathbf{x}} + B\mathbf{u} + \phi(\hat{\mathbf{x}}, \mathbf{u}) + L\mathbf{r} \\ \hat{\mathbf{y}} & = C\hat{\mathbf{x}} + D\mathbf{u} \end{cases}, \tag{3.2}$$

where $\mathbf{r} = \mathbf{y} - \hat{\mathbf{y}}$ is the residual vector, $\hat{\mathbf{y}}$ is the vector of estimated measurements, $\hat{\mathbf{x}}$ is the vector of estimated states, and the matrix L is the observer gain to be designed. The ideal state-space model of a nonlinear system subject to faults can be presented as follows

$$\begin{cases} \dot{\mathbf{x}} = A\mathbf{x} + B\mathbf{u} + \boldsymbol{\phi}(\mathbf{x}, \mathbf{u}) + E_f\mathbf{f} \\ \mathbf{y} = C\mathbf{x} + D\mathbf{u} + F_f\mathbf{f}, \end{cases} \tag{3.3}$$

where the terms $E_f\mathbf{f}$ and $F_f\mathbf{f}$ exist during the fault occurrence. The faults alter the parametric matrices of the state space model by changing their entry values defined by the inverter's physical parameters. Consequently, E_f, F_f, and $\mathbf{f}$ are formed by appropriately manipulating and reorganizing the dynamic equations and the state-space matrices.

3.3.2 Fault modeling

We introduce four fault models defined by the fault vector $\mathbf{f}$ and the fault matrices E_f and F_f. The fault models are not derived from the theory of small signal analysis. Instead, they are modeled according to the theory of model-based fault diagnosis [85]. Such modeling maps faults as alterations in the inverter's state space model, allowing the construction of the fault vector $\mathbf{f}$ and fault matrices E_f, F_f [71, 73]. Mathematically, the alterations in the GFM state space representation originate from the offset sudden change in the variables of interest modeled as $e' = e + \Delta e$ where e can be v_{bdi} and v_{bqi} for busbar faults, ω_{ni} and V_{ni} for actuator faults, or $\eta_{v_{idi}}$ and $\eta_{v_{iqi}}$ for bridge faults.

3.3.2.1 Busbar faults

A busbar fault affects the voltage phasor at the point of common coupling (PCC) with the microgrid. Such voltage is represented by the inputs v_{bdi} and v_{bqi}. The busbar fault is implemented as a symmetrical fault corresponding to the grounding of the point of common coupling (busbar that connects the GFM with the microgrid, also known as PCC) through a balanced low-resistance branch (0.1 Ω). The sudden change in the bus voltage at the PCC is modeled as follows

$$v'_{bdi} = v_{bdi} + \Delta v_{bdi} \tag{3.4}$$

$$v'_{bqi} = v_{bqi} + \Delta v_{bqi} \tag{3.5}$$

Hence, by plugging (3.4) and (3.5) into (3.1), the fault model for the busbar fault is given as

$$\begin{aligned} f &= \begin{bmatrix} \Delta v_{bdi} & \Delta v_{bqi} \end{bmatrix}^{\top}, \\ E_f &= \begin{bmatrix} 0_{1\times 11} & -\frac{1}{L_{ci}} & 0 \\ 0_{1\times 11} & 0 & -\frac{1}{L_{ci}} \end{bmatrix}^{\top}, \\ F_f &= \begin{bmatrix} 0_{7\times 2} \end{bmatrix}. \end{aligned}$$

3.3.2.2 Actuator faults

The actuator signals consist of the inputs ω_{ni} and V_{ni}, respectively, which set the GFMs' desired frequency and voltage magnitude. A sudden 10% change in the actuator reference signals is modeled as follows

$$\omega'_{ni} = \omega_{ni} + \Delta\omega_{ni} \tag{3.6}$$

$$V'_{ni} = V_{ni} + \Delta V_{ni}. \tag{3.7}$$

The actuator fault on ω_{ni} affects the linear term $B\mathbf{u}$ and the nonlinear function $\boldsymbol{\phi}(\mathbf{x}, \mathbf{u})$ of (3.1). Hence, by replacing (3.6) in (3.1), the fault model of the actuator ω_{ni} fault is

$$f_{\omega_{ni}} = \Big[\Delta\omega_{ni} \quad \Delta\omega_{ni} i_{lqi} \quad \Delta\omega_{ni} i_{ldi} \quad \Delta\omega_{ni} v_{oqi}$$

$$\begin{bmatrix} \Delta\omega_{ni} v_{odi} & \Delta\omega_{ni} i_{oqi} & \Delta\omega_{ni} i_{odi} \end{bmatrix}^\top$$

$$E_{f_{\omega_{ni}}} = \begin{bmatrix} 1 & 0_{1\times 6} \\ 0_{6\times 1} & 0_{6\times 6} \\ 0_{6\times 1} & A_{\omega_{ni}} \end{bmatrix}$$

$$A_{\omega_{ni}} = \text{diag}\left(\begin{bmatrix} 1 & -1 & 1 & -1 & 1 & -1 \end{bmatrix} \right)$$

$$F_{f_{\omega_{ni}}} = \begin{bmatrix} 0 & 1 & 0_{1\times 5} \\ 0_{6\times 1} & 0_{6\times 1} & 0_{6\times 5} \end{bmatrix}^\top$$

The actuator fault on V_{ni} affects the linear term $B\mathbf{u}$ of (3.1) exclusively. Similarly, by replacing (3.7) in (3.1), the fault model of the actuator V_{ni} fault is

$$f_{V_{ni}} = \begin{bmatrix} \Delta V_{ni} \end{bmatrix}$$

$$E_{f_{V_{ni}}} = \begin{bmatrix} 0_{1\times 3} & 1 & 0 & K_{PV_i} & 0 & \frac{1}{L_{fi}} K_{PC_i} K_{PV_i} & 0_{1\times 5} \end{bmatrix}^\top$$

$$F_{f_{V_{ni}}} = \begin{bmatrix} 0 & 0 & 1 & K_{PV_i} & 0 & K_{PC_i} K_{PV_i} & 0 \end{bmatrix}^\top$$

In this study, the actuator ω_{ni} and V_{ni} signals are the outputs of secondary controllers designed to regulate both reference signals. We consider that the actuator faults occur due to malfunctioning of the secondary controllers' input signals rather than the controllers themselves. The actuator signals these controllers compute rely on measurements such as output voltage magnitude v_{oi} and frequency ω_i of each inverter [2, 86]. A physical fault or the malfunctioning of the devices that measure

v_{oi} and ω_i impacts the output of the secondary controller and, consequently, the grid-forming inverter's performance [3].

3.3.2.3 Inverter bridge faults

The inverter bridge fault is modeled as an abrupt 10% change in the inverter's efficiency. Ideally, the DQ output voltages of the current controller v_{idi}^* and v_{iqi}^* are equal to the inverter bridge's output voltage v_{idi} and v_{iqi}

$$v_{idi} = \eta_{v_{idi}} v_{idi}^*, \quad \eta_{v_{idi}} = 1$$

$$v_{iqi} = \eta_{v_{iqi}} v_{iqi}^*, \quad \eta_{v_{iqi}} = 1$$

In this sense, we model the sudden change in the inverter bridge's efficiency as a parametric abrupt change

$$v_{idi} = (1 - \Delta\eta_{v_{idi}}) v_{idi}^*, \quad \Delta\eta_{v_{idi}} \in (0, 1]$$

$$v_{iqi} = (1 - \Delta\eta_{v_{iqi}}) v_{iqi}^*, \quad \Delta\eta_{v_{iqi}} \in (0, 1]$$

We find the inverter bridge fault model by modifying the corresponding dynamical equations that depend on v_{idi}^* and v_{iqi}^*. Consequently, we split the analysis into two parts.

The fault vector and the fault matrix corresponding to v_{idi} are given as follows

$$\begin{aligned}
\mathbf{f}_{v_{idi}} &= \Delta\eta_{v_{idi}} \begin{bmatrix} Q_i & \phi_{di} & \gamma_{di} & i_{ldi} & i_{lqi} & v_{odi} & v_{oqi} & i_{odi} & V_{ni} \end{bmatrix}^{\top} \\
E_{f_{v_{idi}}} &= \begin{bmatrix} 0_{9\times 7} & \boldsymbol{\xi}_{v_{idi}} & 0_{9\times 5} \end{bmatrix}^{\top} \\
F_{f_{v_{idi}}} &= \begin{bmatrix} 0_{9\times 5} & \boldsymbol{\tau}_{v_{idi}} & 0_{9\times 1} \end{bmatrix}^{\top} \\
\boldsymbol{\xi}_{v_{idi}} &= \Bigg[\tfrac{K_{PC_i}K_{PV_i}n_{Q_i}}{L_{fi}} \quad -\tfrac{K_{PC_i}K_{IV_i}}{L_{fi}} \quad -\tfrac{K_{IC_i}}{L_{fi}} \quad \tfrac{K_{PC_i}}{L_{fi}} \quad \omega_b \\
&\qquad \tfrac{K_{PC_i}K_{PV_i}}{L_{fi}} \quad \tfrac{K_{PC_i}\omega_b C_{fi}}{L_{fi}} \quad -\tfrac{K_{PC_i}F_i}{L_{fi}} \quad -\tfrac{K_{PC_i}K_{PV_i}}{L_{fi}} \Bigg]^{\top} \\
\boldsymbol{\tau}_{v_{idi}} &= \Big[K_{PC_i}K_{PV_i}n_{Q_i} \quad -K_{PC_i}K_{IV_i} \quad -K_{IC_i} \quad K_{PC_i} \\
&\qquad \omega_b L_{fi} \quad K_{PC_i}K_{PV_i} \quad K_{PC_i}\omega_b C_{fi} \quad -K_{PC_i}F_i \\
&\qquad -K_{PC_i}K_{PV_i} \Big]^{\top}
\end{aligned}$$

The fault vector and fault matrices corresponding to v_{iqi} are given as follows

$$\begin{aligned}
\mathbf{f}_{v_{iqi}} &= \Delta\eta_{v_{iqi}} \begin{bmatrix} \phi_{qi} & \gamma_{qi} & i_{ldi} & i_{lqi} & v_{odi} & v_{oqi} & i_{oqi} \end{bmatrix}^{\top} \\
E_{f_{v_{iqi}}} &= \begin{bmatrix} 0_{7\times 8} & \boldsymbol{\xi}_{v_{iqi}} & 0_{7\times 4} \end{bmatrix}^{\top} \\
F_{f_{v_{iqi}}} &= \begin{bmatrix} 0_{7\times 6} & \boldsymbol{\tau}_{v_{iqi}} \end{bmatrix}^{\top} \\
\boldsymbol{\xi}_{v_{iqi}} &= \Bigg[-\tfrac{K_{PC_i}K_{IV_i}}{L_{fi}} \quad -\tfrac{K_{IC_i}}{L_{fi}} \quad -\omega_b \quad \tfrac{K_{PC_i}}{L_{fi}} \\
&\qquad -\tfrac{K_{PC_i}\omega_b C_{fi}}{L_{fi}} \quad \tfrac{K_{PC_i}K_{PV_i}}{L_{fi}} \quad -\tfrac{K_{PC_i}F_i}{L_{fi}} \Bigg]
\end{aligned}$$

$$\boldsymbol{\tau}_{v_{iqi}} = \begin{bmatrix} -K_{PC_i}K_{IV_i} & -K_{IC_i} & -\omega_b L_{fi} & K_{PC_i} \\ -K_{PC_i}\omega_b C_{fi} & K_{PC_i}K_{PV_i} & -K_{PC_i}F_i \end{bmatrix}^\top .$$

The inverter bridge fault affects both efficiencies simultaneously. The fault model of the inverter bridge fault is given as $\mathbf{f} = \begin{bmatrix} \mathbf{f}_{v_{idi}}, \mathbf{f}_{v_{iqi}} \end{bmatrix}^\top$, $E_f = \begin{bmatrix} E_{f_{v_{idi}}}, E_{f_{v_{iqi}}} \end{bmatrix}$, and $F_f = \begin{bmatrix} F_{f_{v_{idi}}}, F_{f_{v_{iqi}}} \end{bmatrix}$.

3.3.3 Fault detection logic

We follow the protocol presented in [85] to decide whether a fault occurs. We define the function that evaluates the residual as $J = \|\mathbf{r}\|_2$. Ideally, during a fault-free scenario, the value of J must be zero and strictly positive. Nonetheless, J is strictly positive even when a fault is absent due to the presence of disturbances. The adaptive threshold is set by considering the system is in the absence of faults and subjected to disturbances. The rule for detecting a fault is defined as

$$\begin{cases} \text{Absence of faults,} & \text{if } J \leq J_{\text{th}} \\ \text{Fault alarm,} & \text{if } J > J_{\text{th}}. \end{cases} \tag{3.8}$$

An essential component in any scheme for detecting faults is the threshold J_{th}. A trustworthy threshold reduces the chances of false alarms and missed detection while enhancing the fault detection capability.

$$
\left\{
\begin{aligned}
A^\top &= \begin{bmatrix}
0 & 0 & 0 & 0 & 0 & 0 & 0 & 0 & 0 & 0 & 0 & 0 & 0 \\
-m_{P_i} & -\omega_{ci} & 0 & 0 & 0 & 0 & 0 & 0 & 0 & 0 & 0 & 0 & 0 \\
0 & 0 & -\omega_{ci} & -n_{Q_i} & 0 & -K_{PV_i} n_{Q_i} & 0 & -\frac{1}{L_{fi}} K_{PC_i} K_{PV_i} n_{Q_i} & 0 & 0 & 0 & 0 & 0 \\
0 & 0 & 0 & 0 & 0 & K_{IV_i} & 0 & \frac{1}{L_{fi}} K_{PC_i} K_{IV_i} & 0 & 0 & 0 & 0 & 0 \\
0 & 0 & 0 & 0 & 0 & 0 & K_{IV_i} & 0 & \frac{1}{L_{fi}} K_{PC_i} K_{IV_i} & 0 & 0 & 0 & 0 \\
0 & 0 & 0 & 0 & 0 & 0 & 0 & \frac{1}{L_{fi}} K_{IC_i} & 0 & 0 & 0 & 0 & 0 \\
0 & 0 & 0 & 0 & 0 & 0 & 0 & 0 & \frac{1}{L_{fi}} K_{IC_i} & 0 & 0 & 0 & 0 \\
0 & 0 & 0 & 0 & 0 & -1 & 0 & -\left(\frac{R_{fi}}{L_{fi}} + \frac{1}{L_{fi}} K_{PC_i}\right) & \omega_b & \frac{1}{C_{fi}} & 0 & 0 & 0 \\
0 & 0 & 0 & 0 & 0 & 0 & -1 & -\omega_b & -\left(\frac{R_{fi}}{L_{fi}} + \frac{1}{L_{fi}} K_{PC_i}\right) & 0 & \frac{1}{C_{fi}} & 0 & 0 \\
0 & 0 & 0 & -1 & 0 & -K_{PV_i} & \omega_b C_{fi} & -\frac{1}{L_{fi}} + \frac{1}{L_{fi}} K_{PC_i} K_{PV_i} & \frac{1}{L_{fi}} K_{PC_i} \omega_b C_{fi} & 0 & 0 & \frac{1}{L_{ci}} & 0 \\
0 & 0 & 0 & 0 & -1 & -\omega_b C_{fi} & -K_{PV_i} & -\frac{1}{L_{fi}} K_{PC_i} \omega_b C_{fi} & -\left(\frac{1}{L_{fi}} + \frac{1}{L_{fi}} K_{PC_i} K_{PV_i}\right) & 0 & 0 & 0 & \frac{1}{L_{ci}} \\
0 & 0 & 0 & 0 & 0 & F_i & 0 & \frac{1}{L_{fi}} K_{PC_i} F_i & 0 & -\frac{1}{C_{fi}} & 0 & -\frac{R_{ci}}{L_{ci}} & 0 \\
0 & 0 & 0 & 0 & 0 & 0 & F_i & 0 & \frac{1}{L_{fi}} K_{PC_i} F_i & 0 & -\frac{1}{C_{fi}} & 0 & -\frac{R_{ci}}{L_{ci}}
\end{bmatrix}, \\
B &= \begin{bmatrix}
-1 & 1 & 0 & 0 & 0 \\
0 & 0 & 0 & 0 & 0 \\
0 & 0 & 0 & 0 & 0 \\
0 & 0 & 1 & 0 & 0 \\
0 & 0 & 0 & 0 & 0 \\
0 & 0 & K_{PV_i} & 0 & 0 \\
0 & 0 & 0 & 0 & 0 \\
0 & 0 & \frac{1}{L_{fi}} K_{PC_i} K_{PV_i} & 0 & 0 \\
0 & 0 & 0 & 0 & 0 \\
0 & 0 & 0 & 0 & 0 \\
0 & 0 & 0 & 0 & 0 \\
0 & 0 & 0 & -\frac{1}{L_{ci}} & 0 \\
0 & 0 & 0 & 0 & -\frac{1}{L_{ci}}
\end{bmatrix}, \quad
C^\top = \begin{bmatrix} 0 \\ 0 \\ -n_{Q_i} \\ 0 \\ 0 \\ 0 \\ 0 \\ 0 \\ 0 \\ 0 \\ 0 \\ 0 \\ 0 \end{bmatrix}, \quad
D^\top = \begin{bmatrix} 0 \\ 0 \\ 1 \\ 0 \\ 0 \end{bmatrix}, \quad
\boldsymbol{\phi}(\mathbf{x}, \mathbf{u}) = \begin{bmatrix}
0 \\
\omega_{ci}(v_{odi} i_{odi} + v_{oqi} i_{oqi}) \\
\omega_{ci}(v_{oqi} i_{odi} - v_{odi} i_{oqi}) \\
0 \\
0 \\
0 \\
0 \\
\omega_{ni} i_{lqi} - m_{P_i} P_i i_{lqi} \\
-\omega_{ni} i_{ldi} + m_{P_i} P_i i_{ldi} \\
\omega_{ni} v_{oqi} - m_{P_i} P_i v_{oqi} \\
-\omega_{ni} v_{odi} + m_{P_i} P_i v_{odi} \\
\omega_{ni} i_{oqi} - m_{P_i} P_i i_{oqi} \\
-\omega_{ni} i_{odi} + m_{P_i} P_i i_{odi}
\end{bmatrix}
\end{aligned}
\right.
\tag{3.9}
$$

3.3.4 Grid-forming inverter model

We use the dq reference frame to represent the grid-forming inverters (GFMs) dynamics according to [3] where the i-th GFM is indexed with the subscript i. The dynamical model of each GFM in state space form considering disturbance- and fault-free scenarios is defined according to (3.1) where

$$
\begin{aligned}
\mathbf{x} &= [\alpha_i \ P_i \ Q_i \ \phi_{di} \ \phi_{qi} \ \gamma_{di} \ \gamma_{qi} \ i_{ldi} \ i_{lqi} \ v_{odi} \ v_{oqi} \ i_{odi} \ i_{oqi}]^\top \\
\mathbf{u} &= [\omega_{com} \ \omega_{ni} \ V_{ni} \ v_{bdi} \ v_{bqi}]^\top \\
\mathbf{y} &= \left[\alpha_i \ \omega_i \ v^*_{odi} \ i^*_{ldi} \ i^*_{lqi} \ v^*_{idi} \ v^*_{iqi}\right]^\top .
\end{aligned}
$$

The parametric matrices A, B, C, D are shown in (3.9) and formed according to the following differential equations governing the GFMs as referenced in [3, 87, 88]. The dynamic equations of the inverter's auxiliary variables are given as

$$\dot{\phi}_{di} = v^*_{odi} - v_{odi}, \tag{3.10a}$$

$$\dot{\phi}_{qi} = -v_{oqi}, \tag{3.10b}$$

$$\begin{aligned}\dot{\gamma}_{di} = F_i i_{odi} - \omega_b C_{fi} v_{oqi} + K_{PVi} v^*_{odi} - K_{PVi} v_{odi} \\ + K_{IVi} \phi_{di} - i_{ldi},\end{aligned} \tag{3.10c}$$

$$\dot{\gamma}_{qi} = F_i i_{oqi} + \omega_b C_{fi} v_o di - K_{PVi} v_{oqi} + K_{IVi} \phi_{qi} - i_{lqi}. \tag{3.10d}$$

The dynamic equations governing the inverter's power angle, active power, and reactive power are presented as follows

$$\dot{\delta}_i = \omega_i - \omega_{com}, \tag{3.11a}$$

$$\dot{P}_i = -\omega_{ci} P_i + \omega_{ci}(v_{odi} i_{odi} + v_{oqi} i_{oqi}), \tag{3.11b}$$

$$\dot{Q}_i = -\omega_{ci} Q_i + \omega_{ci}(v_{oqi} i_{odi} - v_{odi} i_{oqi}). \tag{3.11c}$$

The differential equations of the inverter's output current magnitudes, voltage magnitudes, and LC filter output current magnitudes are

$$\dot{i}_{ldi} = -\frac{R_{fi}}{L_{fi}} i_{ldi} + \omega_{ni} i_{lqi} + \frac{1}{L_{fi}}(v_{idi} - v_{odi}), \tag{3.12a}$$

$$\dot{i}_{lqi} = -\frac{R_{fi}}{L_{fi}} i_{lqi} - \omega_{ni} i_{ldi} + \frac{1}{L_{fi}}(v_{iqi} - v_{oqi}), \tag{3.12b}$$

$$\dot{v}_{odi} = \omega_{ni} v_{oqi} + \frac{1}{C_{fi}}(i_{ldi} - i_{odi}), \tag{3.12c}$$

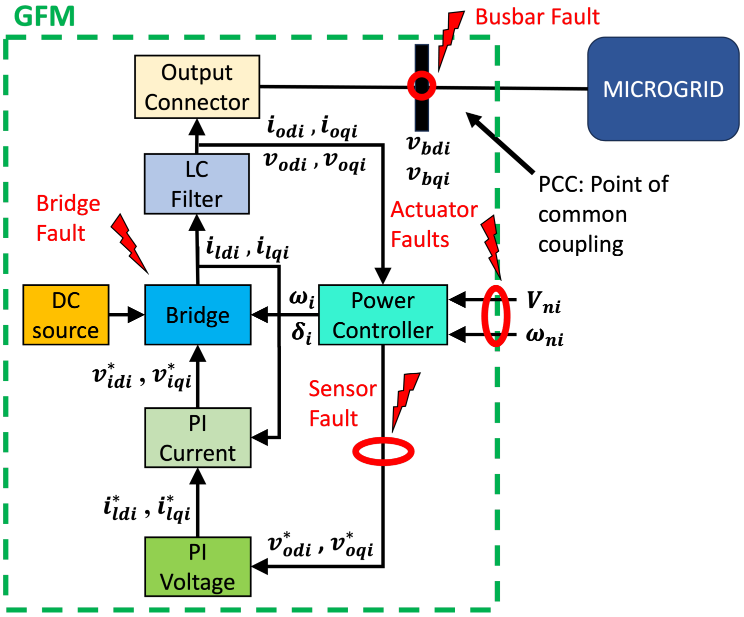

Figure 3.1: Block diagram of grid-forming inverter [2].

$$\dot{v}_{oqi} = -\omega_{ni} v_{odi} + \frac{1}{C_{fi}}(i_{lqi} - i_{oqi}), \tag{3.12d}$$

$$\dot{i}_{odi} = -\frac{R_{ci}}{L_{ci}} i_{odi} + \omega_{ni} i_{oqi} + \frac{1}{L_{ci}}(v_{odi} - v_{bdi}), \tag{3.12e}$$

$$\dot{i}_{oqi} = -\frac{R_{ci}}{L_{ci}} i_{oqi} - \omega_{ni} i_{odi} + \frac{1}{L_{ci}}(v_{oqi} - v_{bqi}). \tag{3.12f}$$

The nonlinear function $\boldsymbol{\phi}(\mathbf{x}, \mathbf{u})$ arises from the Kirchoff voltage and current laws and the low-pass filtered reactive and active power. The grid-forming inverter model considered in this work is described in the block diagram shown in Fig. 3.1. We assume that the GFMs are connected to a stable DC source. The voltage, current, and power controllers are tuned such that the GFM can form the microgrid's reference voltage magnitude and frequency. The power controller sets the operating frequency ($\omega_i = \omega_{ni} - m_{P_i} P_i$) of the inverter bridge, provides the voltage magnitude references

($v^*_{odi} = V_{ni} - n_{Q_i}Q_i, v^*_{oqi} = 0$) to the voltage controller, and contains the droop curves for power-sharing coordination. Using a PI control strategy, the voltage controller aligns the output voltage magnitude perpendicular to the q-axis and provides the current references to the current controller. The current controller uses a PI control strategy to charge/discharge the capacitor of the LC filter so that the desired voltage magnitude is achieved. Both PI controllers introduce auxiliary variables to simplify the state space modeling where $\dot{\phi}_{qi} = v^*_{oqi} - v_{oqi}$, $\dot{\phi}_{di} = v^*_{odi} - v_{odi}$, $\dot{\gamma}_{qi} = i^*_{lqi} - i_{lqi}$, and $\dot{\gamma}_{di} = i^*_{ldi} - i_{ldi}$. The output connector smoothens the output current of the GFM and couples it with the microgrid at the point of common coupling (PCC) [2, 3].

The dq frame of one of the microgrid's generators is selected as the common reference frame rotating at the frequency ω_{com}. Under ambient conditions, the rotating frame of the microgrid's power injection technologies overlaps the common reference frame. However, when a disturbance occurs, the disturbance introduces a phase difference $\delta_i = \int \omega_i - \omega_{com}$ between the power injection technologies and the reference generator where ω_i is the rotation frequency of each technology's frame. Consequently, the frame of each technology no longer overlaps with the common reference frame. According to [89], a rotation matrix is used to map the reference frame to the frame of each technology as follows

$$\begin{bmatrix} x_{bdi} \\ x_{bqi} \end{bmatrix} = \begin{bmatrix} \cos(\delta_i) & \sin(\delta_i) \\ -\sin(\delta_i) & \cos(\delta_i) \end{bmatrix} \begin{bmatrix} x_{bDi} \\ x_{bQi} \end{bmatrix}, \tag{3.13}$$

where x represents voltage (v) or current (i) magnitude. For example, the voltage magnitude at the point of common coupling, denoted as v_{bDi} and v_{bQi}, is converted to the frame of the i-th GFM as $v_{bdi} = \cos(\delta_i)v_{bDi} + \sin(\delta_i)v_{bQi}$, and $v_{bqi} = -sin(\delta_i)v_{bDi} + cos(\delta_i)v_{bQi}$. A similar conversion is applied for the current magnitude in the dq domain.

3.4 Fault detection with fixed thresholding

3.4.1 Nonlinear model with bounded uncertainties

The nonlinear model (3.1) can be modified to incorporate both disturbances and faults as follows

$$\begin{cases} \dot{\mathbf{x}} &= A\mathbf{x} + B\mathbf{u} + \boldsymbol{\phi}(\mathbf{x}, \mathbf{u}) + E_w\mathbf{w} + E_f\mathbf{f} + \eta_1(\mathbf{x}, \mathbf{u}) \\ \mathbf{y} &= C\mathbf{x} + D\mathbf{u} + F_w\mathbf{w} + F_f\mathbf{f} + \eta_2(\mathbf{x}, \mathbf{u}), \end{cases} \tag{3.14}$$

where $\mathbf{w}$ is a disturbance input vector, $\mathbf{f}$ is the fault vector, E_w and F_w are constant disturbance matrices, E_f and F_f are deterministic fault matrices. The unknown functions η_1 and η_2 represent the model uncertainties which are considered to be bounded and finite, i.e.,

$$\|\eta_i(\mathbf{u}, \mathbf{x})\| < \infty, \quad \forall\, \mathbf{x} \in \mathcal{D} \text{ and } \forall\, \mathbf{u}\, \in \mathcal{U},\ i = 1, 2.$$

In this work, we assume that

1. The nonlinear system (3.14) is observable, and

2. The disturbance vector $\mathbf{w}$ and fault vector $\mathbf{f}$ are $\mathcal{L}_2$ square-integrable satisfying $\|\mathbf{w}\|_{[0,t]} < \infty$ and $\|\mathbf{f}\|_{[0,t]} < \infty$.

3.4.2 Residual generation

Define the error of state $\mathbf{e} = \mathbf{x} - \hat{\mathbf{x}}$ and measurement residual $\mathbf{r} = W(\mathbf{y} - \hat{\mathbf{y}})$. Then, the dynamics of the error of state can be derived as follows:

$$\begin{cases} \dot{\mathbf{e}} &= (A - LC)\mathbf{e} + (E_w - LF_w)\mathbf{w} \\ & \quad +(E_f - LF_f)\mathbf{f} + \phi(\mathbf{x}, \mathbf{u}) - \phi(\hat{\mathbf{x}}, \mathbf{u}) \cdot \\ \mathbf{r} &= W(\mathbf{y} - C\hat{\mathbf{x}} - D\mathbf{u}) \end{cases} \tag{3.15}$$

We can compactly rewrite (3.33) as:

$$\begin{cases} \dot{\mathbf{e}} &= \bar{A}\mathbf{e} + \Phi + \bar{E}_w\mathbf{w} + \bar{E}_f\mathbf{f} \\ \mathbf{r} &= \bar{C}\mathbf{e} + \bar{F}_w\mathbf{w} + \bar{F}_f\mathbf{f} \end{cases} \tag{3.16}$$

with $\Phi \triangleq \phi(\mathbf{x}, \mathbf{u}) - \phi(\hat{\mathbf{x}}, \mathbf{u})$ and

$$\begin{cases} \bar{A} = A - LC, & \bar{E}_w = E_w - LF_w, & \bar{E}_f = E_f - LF_f \\ \bar{C} = WC, & \bar{F}_w = WF_w, & \bar{F}_f = WF_f \end{cases} . \tag{3.17}$$

We assume $W = I$ as suggested by [90]. The residual $\mathbf{r}$ can be used for fault detection [73].

3.4.3 Mixed $\mathcal{H}_-/\mathcal{H}_\infty$ optimization for observer design

The fault detection problem becomes challenging when there is no clear distinction between disturbances and faults. Such a situation may mislead the fault detection filter, triggering false alarms. To cope with such a concern, we considered the mixed $\mathcal{H}_-/\mathcal{H}_\infty$ optimization framework for designing our proposed observer [73]. This framework aims to simultaneously make the fault detector filter responsive to faults and sturdy against disturbances by satisfying the following criteria

1. Robustness against disturbances $\mathbf{w}$:

$$\|\mathbf{r}_w\|_{[0,t]} \leq \alpha\|\mathbf{w}\|_{[0,t]}. \tag{3.18}$$

2. Sensitivity to faults $\mathbf{f}$:

$$\|\mathbf{r}_f\|_{[0,t]} \geq \beta\|\mathbf{f}\|_{[0,t]} \tag{3.19}$$

where

$$\mathbf{r}_w = \bar{C}\mathbf{e} + \bar{F}_w\mathbf{w} \tag{3.20}$$

$$\mathbf{r}_f = \bar{C}\mathbf{e} + \bar{F}_f\mathbf{f}. \tag{3.21}$$

In Section 3.4.6, we pose the task of designing a fault detection filter as a convex optimization problem. We will find linear matrix inequalities to propose sufficient conditions to guarantee the existence of such a filter. In this sense, we transform conditions (3.18) and (3.19) into linear matrix inequalities to incorporate them in the filter design effectively.

3.4.4 Threshold computation

The threshold is calculated when the system is in a fault-free condition and subjected to disturbances

$$J_{\text{th}} = \sup_{\mathbf{w}\in\mathcal{L}_2} \|\mathbf{r}_{\mathbf{w}}\|. \tag{3.22}$$

The threshold is an upper bound for the residual norm in a fault-free condition. Notice that the threshold is a fixed magnitude immutable to the faults and the GFM's conditions. The third component, the residual norm, is computed from the proposed observers, which are designed to significantly perturb the residual norms by the presence of faults, making the residual norm exceed the threshold.

3.4.5 Lipschitz observer design

Lipschitz systems include a broad range of physical systems, providing flexibility for the design of observers. Let us assume the nonlinear function $\boldsymbol{\phi}(\cdot)$ satisfies the Lipschitz condition given by the definition given as follows

Definition 3.4.1. A function $\boldsymbol{f}(\cdot)$ is *Lipschitz* continuous if there exists a constant

$\gamma > 0$ such that $\forall\, \mathbf{u} \in \mathcal{U}$ and $\forall\, \mathbf{x}, \hat{\mathbf{x}} \in \mathcal{D}$ we have

$$\|\boldsymbol{f}(\mathbf{x}, \mathbf{u}) - \boldsymbol{f}(\hat{\mathbf{x}}, \mathbf{u})\| \leq \gamma \|\mathbf{x} - \hat{\mathbf{x}}\|. \tag{3.23}$$

The lemma presented below gives sufficient conditions for the existence of a filter gain matrix L based on the mixed $\mathcal{H}_-/\mathcal{H}_\infty$ optimization framework for Lipschitz nonlinear systems.

Lemma 3.4.1 (see [73])**.** Consider the system (3.14) with a Lipschitz continuous observer defined in (3.2) and (3.23). If there exists a gain matrix L, strictly positive scalars α, β, ε_1, ε_2, and identical positive definite matrices Q and P such that the following two LMIs hold

$$\begin{bmatrix} \Omega_1 & P\bar{E}_w + \bar{C}^\top \bar{F}_w & P \\ * & -\alpha^2 I + \bar{F}_w^\top \bar{F}_w & 0 \\ * & * & -\varepsilon_1 I \end{bmatrix} \prec 0 \tag{3.24}$$

$$\begin{bmatrix} \Omega_2 & Q\bar{E}_f - \bar{C}^\top \bar{F}_f & Q \\ * & -\beta^2 I + \bar{F}_f^\top \bar{F}_f & 0 \\ * & * & -\varepsilon_2 I \end{bmatrix} \prec 0, \tag{3.25}$$

where $\Omega_1 = \bar{A}^\top P + P\bar{A} + \bar{C}^\top \bar{C} + \varepsilon_1 \gamma^2 I$, $\Omega_2 = \bar{A}^\top Q + Q\bar{A} - \bar{C}^\top \bar{C} + \varepsilon_2 \gamma^2 I$, and γ is the given Lipschitz constant. Then, i) the residual generator in (3.33) is stable, and

ii) the resulting observer satisfies the robustness and sensitivity constraints (3.18) and (3.19).

The proof of *Lemma* 3.4.1 can be found in [73], where an LMI solution is proposed by considering a nonlinear system that satisfies the Lipschitz condition under the $\mathcal{H}_{-}/\mathcal{H}_{\infty}$ framework.

3.4.6 Proposed OL and QB observer design

The Lipschitz constant is sensitive to the operating region of the system $\mathcal{D} \times \mathcal{U}$ and the parameters that define the nonlinear function $\boldsymbol{\phi}(\cdot)$. In this scenario, *Lemma* 3.4.1 might presumably fail to obtain the observer's gain matrix L and make the residual generator dynamics stable. Generalizing the Lipchitz condition by considering the QB and OL conditions is a suitable alternative according to [82, 83].

Definition 3.4.2. The function $\boldsymbol{f}(\cdot)$ is one-sided Lipschitz continuous if a constant $\rho \in \mathbb{R}$ exists such that $\forall\, u \in \mathcal{U}$ and $\forall\, \mathbf{x}, \hat{\mathbf{x}} \in \mathcal{D}$:

$$\langle \boldsymbol{f}(\mathbf{x}, \mathbf{u}) - \boldsymbol{f}(\hat{\mathbf{x}}, \mathbf{u}), \mathbf{x} - \hat{\mathbf{x}} \rangle \leq \rho \|\mathbf{x} - \hat{\mathbf{x}}\|^2. \tag{3.26}$$

Definition 3.4.3. The function $\boldsymbol{f}(\cdot)$ is quadratic inner-bounded continuous if the constants $\delta, \varphi \in \mathbb{R}$ exist such that $\forall\, u \in \mathcal{U}$ and $\forall\, \mathbf{x}, \hat{\mathbf{x}} \in \mathcal{D}$

$$\begin{aligned} \|\boldsymbol{f}(\mathbf{x}, \mathbf{u}) - \boldsymbol{f}(\hat{\mathbf{x}}, \mathbf{u})\|^2 \leq \varphi \langle \mathbf{x} - \hat{\mathbf{x}}, \boldsymbol{f}(\mathbf{x}, \mathbf{u}) - \boldsymbol{f}(\hat{\mathbf{x}}, \mathbf{u}) \rangle + \\ \delta \|\mathbf{x} - \hat{\mathbf{x}}\|^2. \end{aligned} \tag{3.27}$$

Remark 3.4.1. Different from the Lipschitz constant γ, the constants ρ, δ, and φ are not required to be positive. Hence, it is beneficial for observers to have a less conservative design.

In the following theorem, we propose sufficient conditions that incorporate the $\mathcal{H}_-/\mathcal{H}_\infty$ framework, and conditions (3.26) and (3.27) to demonstrate the existence of the matrix gain L.

Theorem 3.4.1. Consider the constants ρ, δ, and φ, the system in (3.14) satisfying the conditions (3.26) and (3.27), the observer defined in (3.2) and the residual generator in (3.33). If exist a filter gain matrix L, strictly positive scalars α, β, and $\{\epsilon_i\}_{i=1}^4$, and identical positive definite matrices Q and P, such that the LMIs given as follows hold

$$\begin{bmatrix} \Omega_1 & P\bar{E}_w + \bar{C}^\top \bar{F}_w & P + \frac{1}{2}(\epsilon_2\varphi - \epsilon_1)I \\ * & -\alpha^2 I + \bar{F}_w^\top \bar{F}_w & 0 \\ * & * & -\epsilon_2 I \end{bmatrix} \prec 0 \tag{3.28}$$

$$\begin{bmatrix} \Omega_2 & Q\bar{E}_f - \bar{C}^\top \bar{F}_f & Q + \frac{1}{2}(\epsilon_4\varphi - \epsilon_3)I \\ * & -\beta^2 I + \bar{F}_f^\top \bar{F}_f & 0 \\ * & * & -\epsilon_4 I \end{bmatrix} \prec 0 \tag{3.29}$$

where $\Omega_1 = \bar{A}^\top P + P\bar{A} + \bar{C}^\top \bar{C} + (\epsilon_1\rho + \epsilon_2\delta)I$, $\Omega_2 = \bar{A}^\top Q + Q\bar{A} - \bar{C}^\top \bar{C} + (\epsilon_3\rho + \epsilon_4\delta)I$. Then, we have i) the residual generator is stable, and ii) the observer satisfies the robustness and sensitivity constraints (3.18) and (3.19).

The proof of Theorem 3.4.1 is found in appendix A. Notice that matrices in (3.28) and (3.29) are nonlinear in terms of L, P and Q. However, if we set $Y = PL$, then (3.28) and (3.29) become LMIs in Y. The matrix gain L can be obtained using $L = P^{-1}Y$ once the problem is solved. Hereafter, we refer to our proposed observer design as the OL or OL-QB observer.

3.4.7 Relation between Lipschitz and one-sided Lipschitz observer design for nonlinear systems

The relation between Lemma 3.4.1 and Theorem 3.4.1 is established in Theorem 3.4.2, which indicates that the latter is less conservative.

Theorem 3.4.2. Assume the function $\boldsymbol{\phi}(\mathbf{x}, \mathbf{u})$ is nonlinear and Lipschitz continuous with γ as its Lipschitz constant, and the gain matrices L, P, Q, non-negative scalars ε_1, ε_2 exist such that the inequalities (3.24) and (3.25) hold. Then, there exist non-negative scalars ϵ_1, ϵ_2, ϵ_3, ϵ_4, real scalars ρ, δ, φ, together with the matrices L, P, and Q such that the inequalities in (3.28) and (3.29) are satisfied.

The proof of Theorem 3.4.2 is found in Appendix A.

Remark 3.4.2. One-sided Lipschitz continuity does not imply Lipschitz continuity because the Lipschitz condition is a two-sided inequality [82]. Hence, the converse of Theorem 3.4.2 does not hold, which implies that Theorem 3.4.1 is less conservative than Lemma 3.4.1.

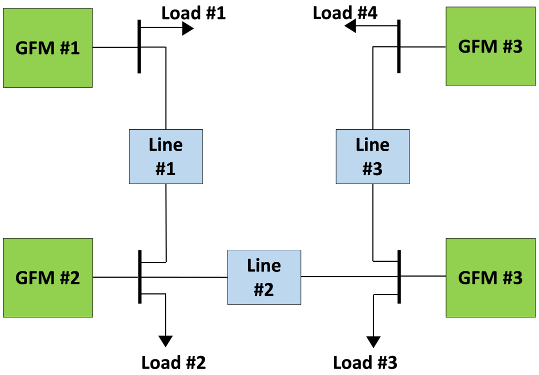

Figure 3.2: The islanded droop-controlled AC microgrid test system [3].

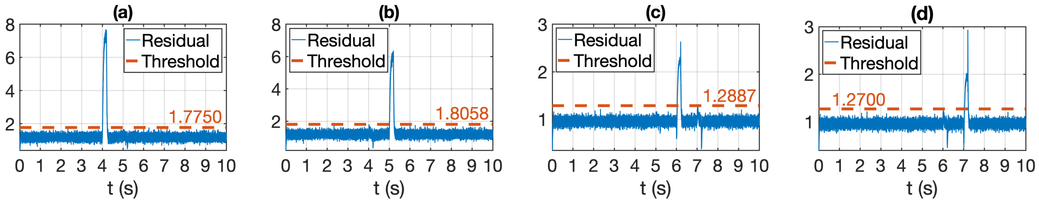

Figure 3.3: Residual norms under busbar fault at the PCC using a one-sided Lipschitz observer: (a) GFM #1 at $t = 4$, (b) GFM #2 at $t = 5$, (c) GFM #3 at $t = 6$, and (d) GFM #4 at $t = 7$. The faults are cleared after 0.2 seconds.

3.4.8 Numerical experiments

We evaluate our proposed observer- and residual-based strategy using the islanded AC microgrid shown in Fig. 3.2. The microgrid has four GFMs, three inductive branches, and four RL loads. The parameters of the microgrid, GFMs, branches, and loads are presented in Tables 3.1 and 3.2, as described in [3]. We run the experiments using a MacBook Pro 2019, 2.8 GHz Intel Core i7 processor, 16 GB 2133 MHz LPDDR3 RAM, and 1 TB hard disk drive. The experiments were performed using MATLAB, Simulink, and the *YALMIP* toolbox with the semidefinite programming solvers *LMILAB*, *MOSEK*, *SeDuMi*, and *SDPT3* to solve optimization

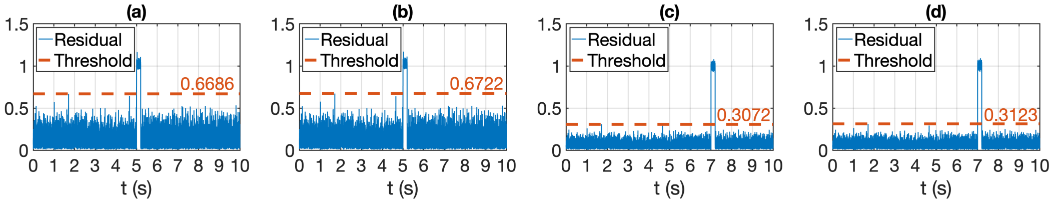

Figure 3.4: Residual norms under an actuator fault corresponding to input ω_{ni}. (a) and (b) GFM #2 at $t = 5$; (c) and (d) GFM #4 at $t = 7$. The residual norms of the one-sided Lipschitz observer are shown in (a) and (c), while the residual norms of the Lipschitz observer correspond to (b) and (d). The fault is cleared after 0.2 seconds.

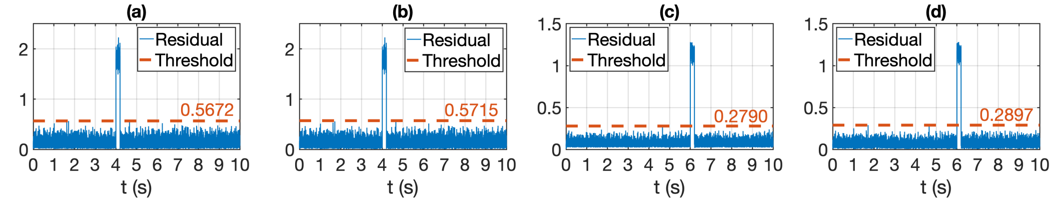

Figure 3.5: Residual norms under an actuator fault corresponding to input V_{ni}. (a) and (b) GFM #1 at $t = 4$; (c) and (d) GFM #3 at $t = 6$. The residual norms of the one-sided Lipschitz observer are shown in (a) and (c), while the residual norms of the Lipschitz observer correspond to (b) and (d). The fault is cleared after 0.2 seconds.

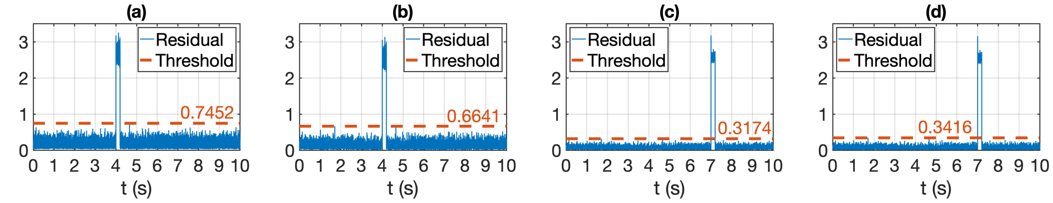

Figure 3.6: Residual norms under an inverter bridge fault (sudden efficiency reduction). (a) and (b) GFM #1 at $t = 4$; (c) and (d) GFM #4 at $t = 7$. The residual norms of the one-sided Lipschitz observer are shown in (a) and (c), while the residual norms of the Lipschitz observer correspond to (b) and (d). The fault is cleared after 0.2 seconds.

problem described by Lemma 3.4.1 and Theorem 3.4.1. The Lipschitz, OL, and QB constants are presented in Table 3.6 and computed according to [84]. For a single type of fault, the fault simulations happen in this order: at $t = 4$ for GFM #1, at $t = 5$ for GFM #2, at $t = 6$ for GFM #3, and at $t = 7$ for GFM #4. All the faults are cleared after 0.2 seconds. The disturbances are modeled as uncorrelated white Gaussian noise on the process and measurements equations. The disturbance matrices are $E_w = B$, and $F_w = D$ [73]. The faults of other GFMs are also considered disturbances or unknown inputs. For each of our experiments, we use a window of ten seconds to find the highest value of the residual vector $\mathbf{r}$. Such a value is selected as the corresponding threshold J_{th} at each experiment. The following simulations compare our proposed approach based on the OL and QB conditions against the state-of-the-art Lipschitz design.

3.4.8.1 Threshold and residual computation

The threshold is computed over a finite-length period according to two criteria. The first criterion points out that the longer the period, the better the estimate of the actual value of (3.22). The second criterion suggests that a more extended period leads to selecting a threshold that helps reduce the rate of false alarms. In this regard, we recommend choosing the minimum data window to be at least ten times the duration of the faults. In this work, we have chosen a more conservative data window of fifty times the duration of the faults, that is, a window of 10 seconds. Notice that the computed threshold is valid before, during, and after the

Table 3.1: Parameters of the grid-forming inverters.

Parameter	Values	
	GFM #1 & #2	GFM #3 & #4
Power rating (kVA)	45	34
Voltage rating (V)	380	380
m_{Pi}	9.4×10^{-5}	12.5×10^{-5}
n_{Qi}	1.3×10^{-3}	1.5×10^{-3}
$R_{ci}\,(\Omega)$	0.03	0.03
$L_{ci}\,(mH)$	0.35	0.35
$R_{fi}\,(\Omega)$	0.1	0.1
$L_{fi}\,(mH)$	1.35	1.35
$C_{fi}\,(\ \mu F)$	50	50
K_{PVi}	0.1	0.05
K_{IVi}	420	390
K_{PCi}	15	10.5
K_{ICi}	20000	16000
$\omega_b\,(rad/s)$	314.16	314.16

fault occurrence, which means that minimum post-fault data is not required. Besides the threshold, the residual signal computation does not require a data window or minimum post-fault data. Instead, the residual calculation is instantaneous because the residual signal is theoretically obtained from the error dynamics represented by (3.16). Notice that the residual is calculated online before, during, and after the presence of the faults.

3.4.8.2 Droop control

Busbar fault

Fig. 3.3 shows the response of the residual norm using an OL-QB observer when a busbar fault occurs at the end of the output connector of all GFMs. The fault impedance considered is 10% of the nominal voltage magnitude of the busbar.

Table 3.2: Parameters of the AC microgrid.

	Values	
	Resistance (Ω)	Inductance (μH)
Line 1	0.23	318
Line 2	0.35	1847
Line 3	0.23	318
Load 1	30	0.477
Load 2	20	0.318
Load 3	25	0.318
Load 4	25	0.477

The depicted figure illustrates the sensitivity of the four residuals to the busbar fault, with all residuals measuring less than two units. An important observation is that the residual for an individual GFM remains robust against disturbances and faults occurring at other GFMs' PCC. The fault location can be readily identified due to the distinct sensitivity of each residual to its corresponding busbar fault. The observer accommodates the faults at other busbars as disturbances. GFM #1 exhibits the smallest detection time of $t_o = 8$ ms, whereas GFM #4 exhibits the largest around $t_o = 45$ ms. The lowest clearing time $t_c = 30$ ms corresponds to GFM #3, whereas GFM #1 exhibits the highest $t_c = 49$ ms.

Actuator faults

Actuator faults considering the input signal ω_{ni} for GFMs #2 and #4, and the input signal V_{ni} for GFMs #1 and #3 are shown in Figs. 3.4 and 3.5 respectively. We notice that the behavior of the residual norms is very similar for both the one-sided Lipschitz and Lipschitz observers. The residual thresholds are a little less

Table 3.3: Lipschitz, OL, and QB constants for all the grid-forming inverters.

GFM #	γ	ρ	δ	φ
1 & 2	44.7488	22.3688	-0.7493	2.3599
3 & 4	44.7488	22.3688	-0.7535	2.3679

Table 3.4: Computational time of OL-QB and Lipschitz observers: Five-fold average values of the mean μ and the standard deviation σ (both in seconds).

Fault type	OL-QB		Lipschitz	
	μ	σ	μ	σ
Three-phase	1144	7.77	–	–
ω_{ni}	1736	3.85	4076	14.89
V_{ni}	1472	3.11	3784	12.76
Inverter bridge	1686	6.91	1916	6.02

for the one-sided Lipschitz observer. Notice that the residual norm of each GFM remains unaffected by the occurrence of the faults in the other GFMs. In other words, the actuator faults are correctly identified among the GFMs. Both observer types present fault detection and clearing times of less than 1 ms.

Inverter bridge fault

A similar situation occurs with the inverter bridge fault, as shown in Fig. 3.6. The inverter bridge fault corresponds to a reduction in the efficiency of the bridge. The residual norm is below the threshold during the absence of the fault, and it stays above the threshold under the presence of the fault. The location of the bridge faults is properly identified because the residual norms are sensitive to the corresponding GFM. Both observers present fault detection and clearing times of less than 1 ms.

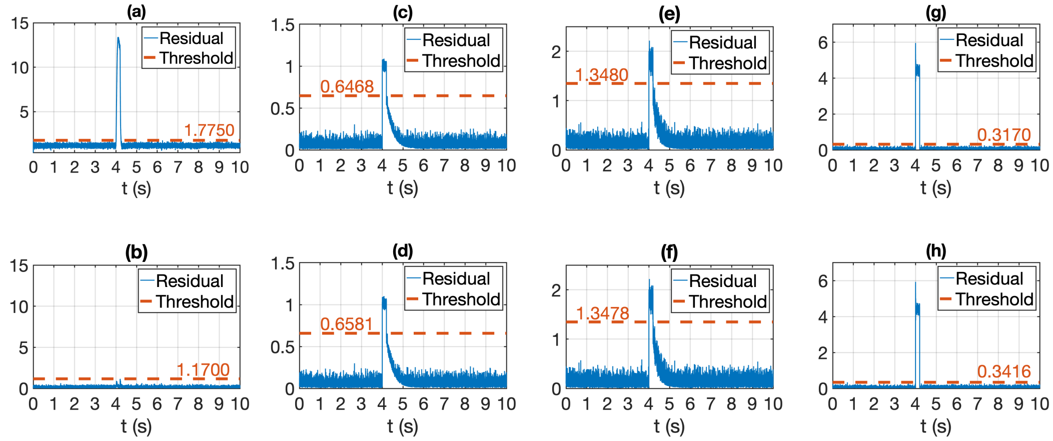

Figure 3.7: Residual norms using an OL-QB observer (upper row) and Lipschitz observer (lower row) in an AC microgrid with technology mix. (a) and (b) GFM #1 under a busbar fault; (c) and (d) GFM #3 under a ω_{ni} actuator fault; (e) and (f) GFM #1 under a V_{ni} actuator fault; (g) and (h) GFM #3 under an inverter bridge fault. The faults last 0.2 seconds.

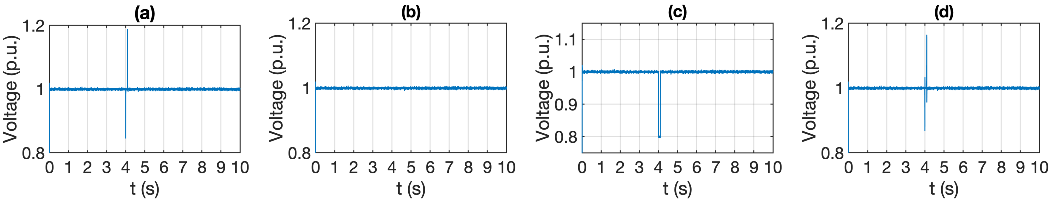

Figure 3.8: Voltage magnitude (p.u.) of GFM #1 in an AC microgrid with technology mix. (a) busbar fault, (b) ω_{ni} actuator fault, (c) V_{ni} actuator fault, and (d) inverter bridge fault. The faults last 0.2 seconds.

3.4.8.3 Virtual synchronous machine control

In this section, we modify the technology mix of the microgrid by replacing GFM #2 and GFM #4 with a grid-following inverter (GFL) and a fourth-order synchronous machine. The dynamic equations of the GFL and parameters can be found in [2]. Similarly, the synchronous machine (SM) parameters and model with turbine-governor and exciter control are found in [91–93]. Second, the droop control of the remaining GFMs #1 and #3 is transformed into its equivalent virtual syn-

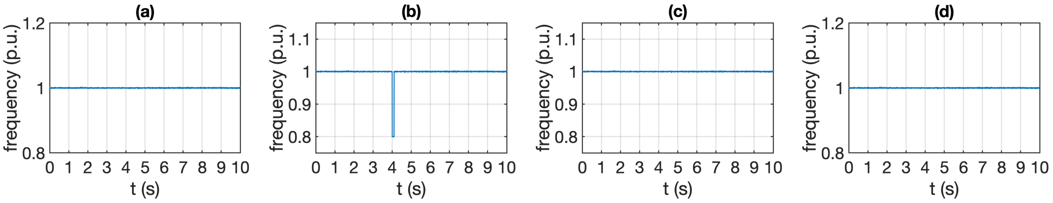

Figure 3.9: Frequency (p.u.) of GFM #1 in an AC microgrid with technology mix. (a) busbar fault, (b) ω_{ni} actuator fault, (c) V_{ni} actuator fault, and (d) inverter bridge fault. The faults last 0.2 seconds.

chronous machine control [94].

Busbar fault

Figure 3.7a shows that the residual norm of the OL-QB observer has increased its peak magnitude during the presence of the busbar fault while preserving the threshold's magnitude compared with the norm's response using droop control as presented in Figure 3.3a. The residual norm of the Lipschitz observer exhibits unresponsive behavior during the fault occurrence. The OL-QB observer exhibits a fault detection time around $t_o = 9$ ms, whereas the clearing time is close to $t_c = 50$ ms.

Actuator faults

Figure 3.7 shows that the shapes of the residual norm under the ω_{ni} and V_{ni} actuator faults present a slow decay after the fault clearance. Such a decay demands an increase in the threshold for the OL-QB and Lipschitz observers. According to our experiments, slow decay results from the dynamics of the frequency and voltage magnitude secondary controllers. The detection time for both type of observers is $t_o = 1$ ms, whereas the clearing times are less than $t_o = 1.3$ ms.

Inverter bridge fault

The response of the residual norm under the inverter bridge fault for GFM #3 is shown in Figures 3.7g and 3.7h. Both responses show higher peak values during the presence of the fault compared to the peak values presented in Figure 3.6. The threshold magnitudes remain similar to the magnitudes of the droop-controlled GFM #4 shown in Figures 3.6c and 3.6d. Both observers present fault detection and clearing times of less than 1 ms.

Figures 3.8 and 3.9 show the voltage magnitude and frequency response per unit at the PCC of GFM #1 when the four internal faults happen. A remarkable observation is that faults will likely be decoupled between voltage magnitude and frequency. For example, the busbar fault is observable in the voltage magnitude, not the frequency. The reason for this phenomenon lies in the characteristic swing equation where the equivalent inertia is inversely proportional to the droop coefficient m_{Pi}, which is in the order of 10^{-5}. Consequently, any change in the unfiltered active power due to the busbar fault does not essentially influence the dynamics of frequency deviations $\Delta\omega$. A similar analysis can be derived for the other internal faults and the droop-controlled GFMs.

Table 3.4 compares the simulation times between the OL-QB and Lipschitz observers. We can not report the simulation time of the Lipschitz design under

Table 3.5: Minimum and maximum fault detection (t_o) and clearance (t_c) response times of the proposed OL-QB observers. The values are obtained by comparing the response times of the observers among all the experiments.

	Fault							
	Busbar		ω_{ni}		V_{ni}		Bridge	
	t_o	t_c	t_o	t_c	t_o	t_c	t_o	t_c
min	7.5	24.9	1.0	1.1	1.0	1.1	1.0	1.0
max	49.7	52.2	1.0	1.3	1.0	1.2	1.0	1.0

a busbar fault because its corresponding optimization program (cf. Lemma 3.4.1) that computes the observer gain matrix is reported as infeasible by the optimization solvers (cf. Remark 3.4.3). Table 3.5 presents our approach's minimum and maximum fault detection and clearing times among all the simulations.

Remark 3.4.3. We identify a drawback of the state-of-the-art Lipschitz observer design. For this particular design, notice that the squared Lipschitz constant in the block matrices Ω_1 and Ω_2 forces the positive definiteness of the LMIs in (3.24) and (3.25). Hence, the feasible set for the matrix gain L becomes more restricted than the counterpart of the one-sided Lipschitz observer. The magnitude of the Lipschitz constant further aggravates the situation. The feasibility issue becomes noticeable for the busbar faults. The four solvers report the optimization problem described by Lemma 3.4.1 as infeasible. On the other hand, the OL and QB constants are not squared in their corresponding constraints and are at least half of the Lipschitz constant (cf. Table 3.6).

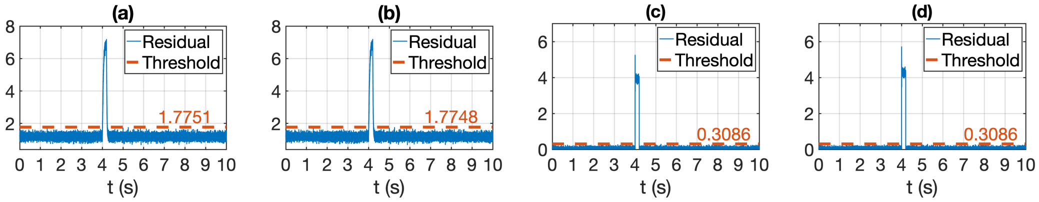

Figure 3.10: Residual norms under the simultaneous occurrence of faults in GFM #1 using the proposed OL-QB observer. (a) busbar and actuator ω_{ni} fault with droop control; (b) busbar and both actuator ω_{ni} and V_{ni} faults with droop control; (c) inverter bridge and actuator V_{ni} fault with virtual synchronous machine control; (d) inverter bridge, busbar and actuator V_{ni} faults with virtual synchronous machine control. The simultaneous faults occur at $t = 4$ and are cleared after 0.2 seconds.

3.4.8.4 Simultaneous occurrence of faults

Figure 3.10 presents a set of experiments under the simultaneous occurrence of faults for GFM #1. Figure 3.10a shows the response of the residual norm under the simultaneous presence of a busbar and V_{ni} faults using our proposed observer designed for a busbar fault. In contrast, an additional ω_{ni} fault is added to the experiment in Figure 3.10b. The busbar fault is the major contributor to the sensitivity of the residual signal. It can be seen that the ω_{ni} fault plays an almost negligible role in the sudden change of the residual norm. Figure 3.10c shows the response of the residual norm under the presence of an inverter bridge and actuator V_{ni} faults using a Lipschitz observer designed for an inverter bridge fault; an additional busbar fault is added to the experiment in Figure 3.10d. The residual signal exhibits a slight increase due to the presence of the busbar fault. Notice that regardless of the simultaneous presence of the faults in the previous four experiments, we observe that the busbar and inverter bridge faults can be identified precisely.

Remark 3.4.4. Fault diagnosis is a two-stage process consisting of fault detection and fault location stages. The fault detection stage sets the basis for a reliable fault location technique. A fault location strategy can be easily derived once a fault is detected. It is worth noting that a single fault may perturb the residual norms of different observers. In this regard, we propose employing a bank of observers to identify triggering patterns among them, thus mitigating the occurrence of false alarms. Another approach is to incorporate the matrix expressions E_f and F_f corresponding to other faults into the disturbance matrix expressions E_w and F_w of the specific fault being analyzed. Alternatively, combining these two solutions, as outlined in [71], can also be considered. However, the comprehensive exploration of these directions is beyond the scope of this paper and will be pursued in future research endeavors.

3.5 Fault detection with adaptive thresholding

3.5.1 Nonlinear model with polytopic uncertainties

In this section, we change the uncertainties in the nonlinear dynamical system model from bounded to polytopic. Such a model can now be expressed as follows

$$\begin{cases} \dot{\mathbf{x}} & = \bar{A}\mathbf{x} + \bar{B}\mathbf{u} + \bar{E}_w\mathbf{w} + E_f\mathbf{f} + \boldsymbol{\phi}(\mathbf{x},\mathbf{u}) \\ \\ \mathbf{y} & = \bar{C}\mathbf{x} + \bar{D}\mathbf{u} + \bar{F}_w\mathbf{w} + F_f\mathbf{f} \end{cases}, \tag{3.30}$$

where,

$$\begin{cases} \bar{A} = A + \Delta A & \bar{B} = B + \Delta B \\ \bar{C} = C + \Delta C & \bar{D} = D + \Delta D \\ \bar{E}_w = E_w + \Delta E_w & \bar{F}_w = F_w + \Delta F_w \end{cases},$$

and $\boldsymbol{\phi}(\mathbf{x}, \mathbf{u})$ captures the nonlinearities in the system. $\mathbf{f}$ is the vector of faults, and $\mathbf{w}$ is the vector of disturbances. The model's matrices are obtained based on the system's dynamical equations. E_f and F_f are the matrix representation of faults, while E_w and F_w correspond to the matrix representation of disturbances. The model uncertainties ΔA, ΔB, ΔC, ΔD, ΔE_w, and ΔF_w belong to the polytope defined as

$$\begin{bmatrix} \Delta A & \Delta B & \Delta E_w \\ \Delta C & \Delta D & \Delta F_w \end{bmatrix} = \mathrm{Co}\left\{\Xi_1, \ldots, \Xi_p\right\}, \tag{3.31}$$

$$\Xi_i = \begin{bmatrix} A_i & B_i & E_{wi} \\ C_i & D_i & F_{wi} \end{bmatrix}, \quad \forall i = 1, \ldots, p, \tag{3.32}$$

where Co denotes the convex hull. A_i, B_i, C_i, D_i, E_{wi}, and F_{wi}, $\forall i = 1, \ldots, p$ are known matrices of appropriate dimensions.

3.5.2 Residual generation

Let us define the measurement error $\mathbf{r} = \mathbf{y} - \hat{\mathbf{y}}$ and state error $\mathbf{e} = \mathbf{x} - \hat{\mathbf{x}}$. Define $\Phi \triangleq \phi(\mathbf{x}, \mathbf{u}) - \phi(\hat{\mathbf{x}}, \mathbf{u})$ and $\phi \triangleq \phi(\hat{\mathbf{x}}, \mathbf{u})$. Then, the dynamics of the state error can be characterized as

$$\begin{cases} \dot{\mathbf{e}} & = (A - LC)\,\mathbf{e} + \left(\bar{E}_w - L\bar{F}_w\right)\mathbf{w} + (E_f - LF_f)\,\mathbf{f} \\ & \quad +\Phi + (\Delta A - L\Delta C)\,\mathbf{x} + (\Delta B - L\Delta D)\,\mathbf{u} \\ \mathbf{r} & = C\mathbf{e} + \bar{F}_w\mathbf{w} + F_f\mathbf{f} + \Delta C\mathbf{x} + \Delta D\mathbf{u}. \end{cases} \tag{3.33}$$

Let us rewrite the error dynamics as

$$\begin{bmatrix} \dot{\mathbf{e}} \\ \dot{\mathbf{x}} \end{bmatrix} = \begin{bmatrix} A - LC & \Delta A - L\Delta C \\ 0 & A + \Delta A \end{bmatrix} \begin{bmatrix} \mathbf{e} \\ \mathbf{x} \end{bmatrix} + \begin{bmatrix} \Delta B - L\Delta D \\ B + \Delta B \end{bmatrix} \mathbf{u}$$
$$+ \begin{bmatrix} \bar{E}_w - L\bar{F}_w \\ \bar{E}_w \end{bmatrix} \mathbf{w} + \begin{bmatrix} E_f - LF_f \\ E_f \end{bmatrix} \mathbf{f} + \begin{bmatrix} \Phi \\ \phi \end{bmatrix},$$

$$\mathbf{r} = \begin{bmatrix} C & \Delta C \end{bmatrix} \begin{bmatrix} \mathbf{e} \\ \mathbf{x} \end{bmatrix} + \begin{bmatrix} \Delta D \end{bmatrix} \begin{bmatrix} \mathbf{u} \end{bmatrix} + \begin{bmatrix} \bar{F}_w \end{bmatrix} \begin{bmatrix} \mathbf{w} \end{bmatrix} + \begin{bmatrix} F_f \end{bmatrix} \begin{bmatrix} \mathbf{f} \end{bmatrix}.$$

Also, let us define

$$\tilde{\mathbf{e}} = \begin{bmatrix} \mathbf{e} \\ \mathbf{x} \end{bmatrix}, \quad \tilde{\mathbf{w}} = \mathbf{w}, \quad \tilde{\mathbf{u}} = \mathbf{u},$$

$$\widetilde{A} = \begin{bmatrix} A - LC & \Delta A - L\Delta C \\ 0 & A + \Delta A \end{bmatrix}, \quad \widetilde{B} = \begin{bmatrix} \Delta B - L\Delta D \\ B + \Delta B \end{bmatrix},$$

$$\widetilde{C} = \begin{bmatrix} C & \Delta C \end{bmatrix}, \quad \widetilde{D} = [\Delta D], \quad \widetilde{\mathbf{\Phi}} = \begin{bmatrix} \Phi \\ \phi \end{bmatrix},$$

$$\widetilde{E}_w = \begin{bmatrix} \bar{E}_w - L\bar{F}_w \\ \bar{E}_w \end{bmatrix}, \quad \widetilde{E}_f = \begin{bmatrix} E_f - LF_f \\ E_f \end{bmatrix}$$

$$\widetilde{F}_w = \begin{bmatrix} \bar{F}_w \end{bmatrix}, \quad \widetilde{F}_f = [F_f].$$

Thus, the error dynamics and residual vectors are given as

$$\begin{cases} \dot{\mathbf{e}} & = \widetilde{A}\tilde{\mathbf{e}} + \widetilde{B}\tilde{\mathbf{u}} + \widetilde{E}_w\tilde{\mathbf{w}} + \widetilde{E}_f\tilde{\mathbf{f}} + \widetilde{\mathbf{\Phi}} \\ \mathbf{r} & = \widetilde{C}\tilde{\mathbf{e}} + \widetilde{D}\tilde{\mathbf{u}} + \widetilde{F}_w\tilde{\mathbf{w}} + \widetilde{F}_f\tilde{\mathbf{f}} \end{cases}, \tag{3.34}$$

which will be used for fault detection [73].

3.5.3 Adaptive Threshold Design

The following theorem establishes an adaptive threshold for fault detection in nonlinear systems.

Theorem 3.5.1. Given a scalar $\alpha \in \mathbb{R}_+$, if there exist $\gamma \in \mathbb{R}$ and a positive definite matrix P, such that the following inequalities hold

$$\begin{bmatrix} P & 0 & 0 & \widetilde{C}^\top \\ 0 & I & 0 & \widetilde{F}_w^\top \\ 0 & 0 & I & \widetilde{D}^\top \\ \widetilde{C} & \widetilde{F}_w & \widetilde{D} & \gamma I \end{bmatrix} \succ \mathbf{0} \tag{3.35}$$

$$\begin{bmatrix} \widetilde{A}^\top P + P\widetilde{A} + \alpha P & P\widetilde{E}_w & P\widetilde{B} & P \\ \widetilde{E}_w^\top P & 0 & 0 & 0 \\ \widetilde{B}^\top P & 0 & -I & 0 \\ P & 0 & 0 & 0 \end{bmatrix} \prec \mathbf{0} \tag{3.36}$$

Then, an adaptive threshold for the residual vector $\mathbf{r}$ is

$$J_{th,adp}(t) = \sqrt{\gamma \times \left(e^{-\alpha t} * \tilde{\mathbf{u}}^\top \tilde{\mathbf{u}} + \bar{d} + \tilde{\mathbf{u}}^\top \tilde{\mathbf{u}} \right)}. \tag{3.37}$$

We can minimize the upper bound by solving the following semidefinite program

$$\boxed{\begin{array}{ll} \underset{\gamma \in \mathbb{R}, P \succ 0}{\text{minimize}} & \gamma \\ \text{subject to} & (3.35) - (3.36). \end{array}}$$

The proof of Theorem 3.5.1 can be found in Appendix A. Due to the polytopic uncertainty of the nonlinear system, the LMIs (3.35) and (3.36) represent infinite LMI constraints, making the optimization problem infinite-dimensional and not tractable. To deal with this problem, let us introduce the following theorem

Theorem 3.5.2 (see [95])**.** The following are equivalent for any H, L_i, R_i.

$$H + \sum_i L_i \Delta R_i \succ \mathbf{0} \quad \forall\, \Delta \in Co\,(\Delta_1, \ldots, \Delta_k) \tag{3.38}$$

$$H + \sum_i L_i \Delta_j R_i \succ \mathbf{0} \quad \forall\, j = 1, \ldots, k \tag{3.39}$$

The theorem says that the LMIs with polytopic uncertainty only need to hold at the vertices of the polytope [95]. To apply Theorem 3.5.2 to the LMIs in (3.35) and (3.36), we set $L_i = R_i = 1$ with $i = 1$ in (3.39), and follow a series of mathematical operations that transform the LMIs into a finite set expressed as

$$\begin{bmatrix} P & 0 & 0 & \widetilde{C}_o^\top \\ 0 & I & 0 & \widetilde{F}_{wo}^\top \\ 0 & 0 & I & \widetilde{D}_o^\top \\ \widetilde{C}_o & \widetilde{F}_{wo} & \widetilde{D}_o & \gamma I \end{bmatrix} + \begin{bmatrix} 0 & 0 & 0 & \Delta\widetilde{C}_i^\top \\ 0 & 0 & 0 & \Delta\widetilde{F}_{wi}^\top \\ 0 & 0 & 0 & \Delta\widetilde{D}_i^\top \\ \Delta\widetilde{C}_i & \Delta\widetilde{F}_{wi} & \Delta\widetilde{D}_i & 0 \end{bmatrix} \succ \mathbf{0} \quad \forall i = 1, \ldots, p$$

$$\begin{bmatrix} \widetilde{A}_o^\top P + P\widetilde{A}_o + \alpha P & P\widetilde{E}_{wo} & P\widetilde{B}_o & P \\ \widetilde{E}_{wo}^\top P & 0 & 0 & 0 \\ \widetilde{B}_o^\top P & 0 & -I & 0 \\ P & 0 & 0 & 0 \end{bmatrix} + \begin{bmatrix} \Delta\widetilde{A}_i^\top P + P\Delta\widetilde{A}_i & P\Delta\widetilde{E}_{wi} & P\Delta\widetilde{B}_i & 0 \\ \Delta\widetilde{E}_{wi}^\top P & 0 & 0 & 0 \\ \Delta\widetilde{B}_i^\top P & 0 & 0 & 0 \\ 0 & 0 & 0 & 0 \end{bmatrix} \prec \mathbf{0}$$

$$\forall i = 1, \ldots, p$$

where

$$\widetilde{A}_o = \begin{bmatrix} A - LC & 0 \\ 0 & A \end{bmatrix}, \quad \widetilde{B}_o = \begin{bmatrix} 0 \\ B \end{bmatrix},$$

$$\widetilde{C}_o = \begin{bmatrix} C & 0 \end{bmatrix}, \quad \widetilde{D}_o = [0],$$

$$\widetilde{E}_{wo} = \begin{bmatrix} E_w - LF_w \\ E_w \end{bmatrix}, \quad \widetilde{F}_{wo} = [F_w],$$

$$\Delta\widetilde{A}_i = \begin{bmatrix} 0 & \Delta A_i - L\Delta C_i \\ 0 & \Delta A_i \end{bmatrix}, \quad \Delta\widetilde{B}_i = \begin{bmatrix} \Delta B_i - L\Delta D_i \\ \Delta B_i \end{bmatrix},$$

$$\Delta\widetilde{C}_i = \begin{bmatrix} 0 & \Delta C_i \end{bmatrix}, \quad \Delta\widetilde{D}_i = [\Delta D_i],$$

$$\Delta\widetilde{E}_i = \begin{bmatrix} \Delta E_{wi} - L\Delta F_{wi} \\ \Delta E_{wi} \end{bmatrix}, \quad \Delta\widetilde{F}_{wi} = [\Delta F_{wi}].$$

Table 3.6: Parameters of the adaptive threshold for the busbar and sensor faults.

	Busbar Fault	Sensor Fault
γ	0.493	0.026
α	1.290	0.121

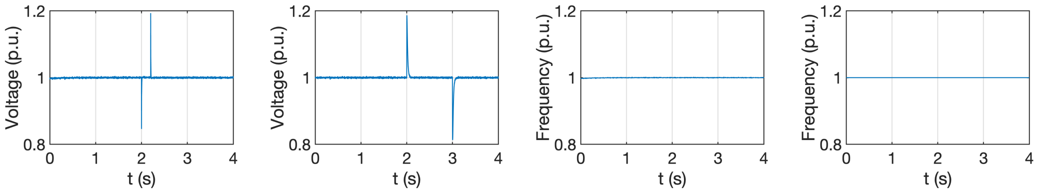

(a) (b) (c) (d)

Figure 3.11: Impact of the internal faults on the voltage magnitude (p.u.) and frequency (p.u.). (a) and (c) busbar fault during 0.2 seconds; (b) and (d) sensor fault during 1 second.

3.5.4 Numerical experiments

We use the islanded AC microgrid, shown in Fig. 3.2, to test the proposed adaptive threshold. The microgrid consists of two GFMs, one GFL, one SG, four busbars, four loads, and three inductive RL branches. The parameters and data of the GFMs and microgrid are shown in Tables 3.1 and 3.2. GFM #1 is selected as the reference generator. The GFMs are locally controlled by the virtual synchronous machine technique (GFM #1) and droop curves (GFM #2) [3]. Moreover, the GFMs incorporate a distributed secondary control layer for the voltage magnitude and frequency. The objective of the secondary voltage controller is to set the input V_{ni} such that the voltage magnitude components converge to $v_{oqi} \to 0$ and $v_{odi} \to v_{ref}$. Similarly, the secondary frequency controller chooses the input ω_{ni} such that ω_i reaches

ω_{com}. The distributed secondary control layer details are in [2]. The parameters of the GFL can be found in [2]. We consider the classical fourth-order nonlinear model for the SG [91] with a BPA-GG governor [93] and low-order exciter [92].

We run the experiments using a MacBook Pro 2019, 2.8 GHz Intel Core i7 processor, 16 GB 2133 MHz LPDDR3 RAM, and 1 TB hard disk drive. The simulations were run using Matlab and Simulink. We use the *YALMIP* toolbox and the *SDPT3* solver to solve the optimization problem in Theorem 3.5.1. All simulations correspond to the grid-forming inverter selected as the reference generator. Similar simulation results were obtained for the remaining inverters in the microgrid test system. Our proposed adaptive threshold is compared with a fixed threshold approach described in a recent work [73]. The disturbance matrices are designed as $E_w = B$ and $F_w = D$. The busbar fault is modeled as $E_f = [B_4\, B_5]$, and $F_f = \mathbf{0}$, whereas the sensor fault is modeled as $E_f = \mathbf{0}$, and $F_f = 1$. The parameter values for the residual thresholds are presented in Table 3.6. We select the parameters of the LC filter as the uncertain parameters. Consequently, the vertices of the polytope $\{\Xi_1, \ldots, \Xi_p\}$ are obtained by uniformly selecting values of these parameters within two percent of the nominal rating shown in Table 3.1. The number of vertices of the polytope is set to $p = 5$.

3.5.4.1 Busbar Fault

The bus at the point of common coupling, which is the bus that connects the GFM with the microgrid, may be subject to a busbar fault. The busbar fault

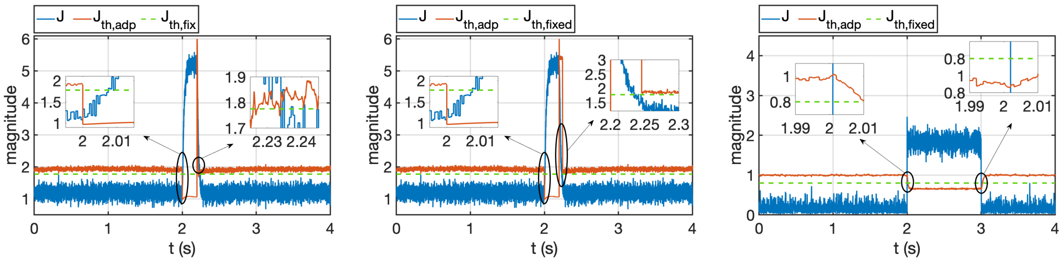

(a) (b) (c)

Figure 3.12: Residual norm, adaptive and fixed threshold comparison: (a) busbar fault, (b) busbar fault with postprocessing, and (c) sensor fault in v^*_{odi}.

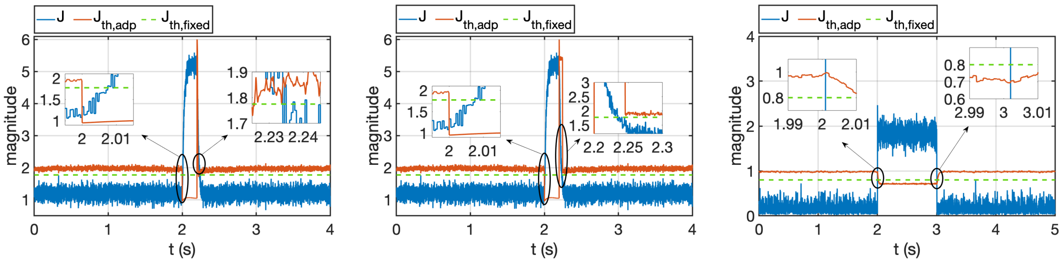

(a) (b) (c)

Figure 3.13: Residual norm, adaptive and fixed threshold comparison with modeling errors: (a) busbar fault, (b) busbar fault with postprocessing, and (c) sensor fault in v^*_{odi}.

is implemented as a symmetrical fault corresponding to the sudden change of the PCC's voltage magnitude (v_{bi}). Fig. 3.11a and Fig. 3.11c present the impact of the busbar fault in the inverter's output voltage magnitude (v_{oi}) and frequency (ω_i). The figures show that the busbar fault perturbs the voltage magnitude at the PCC by decreasing it when the fault occurs and increasing it when the fault is cleared. We observe that the inverter's frequency remains unchanged during the presence of the fault. In other words, the effects of the busbar fault are decoupled between the voltage magnitude and frequency.

The following analysis explains the reason for this phenomenon. The voltage magnitude droop $\omega_i = \omega_{ni} - m_{Pi}P_i$ is equivalent to $\omega_i = \omega_{ni} - \Delta\omega$ and a characteristic swing equation $\dot{\Delta\omega} = \frac{1}{J_i}\left(P_{i,uf} - D_i\Delta\omega\right)$, where J_i, D_i, $P_{i,uf}$ are the equivalent synthetic inertia, damping, and the unfiltered active power measurement for the i-th GFM, respectively. Notice that the product $\frac{1}{J_i}P_{i,uf}$ is exceedingly diminutive because the equivalent inertia J_i is inversely proportional to the droop coefficient m_{Pi}, which is in the order of 10^{-5}. Hence, any change in the unfiltered active power $P_{i,uf}$ due to the busbar fault does not largely influence the dynamics of $\Delta\omega$.

Fig. 3.12a shows the adaptive threshold and residual norm response when a busbar fault occurs at time $t = 2$ s at the PCC. After 0.2 seconds, the busbar fault is cleared at time $t = 2.2$ s. Both thresholds remain above the residual during the absence of the fault in the entire simulation horizon. The adaptive threshold decreases rapidly below the residual norm when the fault happens, as shown in the left magnified box. The fault is detected as early as 0.01 milliseconds. Notice that the adaptive threshold quickly responds to the fault presence, making fault detection fast. On the other hand, using a fixed threshold takes almost ten milliseconds to detect the busbar fault. In the right magnified box, we observe the behavior of the thresholds when the fault is cleared. Both thresholds yield similar clearing times because restoring the fault-free condition takes about 40 milliseconds.

Postprocessing of the adaptive threshold can reduce the threshold's fault-clearing time. In Fig. 3.12a, we observe that the adaptive threshold reaches a maximum value of about six when the busbar fault is cleared at time $t = 2.2$ s. This is because the threshold is computed using the input vector $\mathbf{u}$, which is severely affected by the bus voltages v_{bdi} and v_{bqi} when the busbar fault occurs. Fig. 3.12b presents the post-processed response of the adaptive threshold and the residual norm. The postprocessing consists of holding the value of the dynamic residual for approximately 30 milliseconds as soon as the maximum value of the threshold is detected, i.e., immediately after the fault is cleared. The threshold follows its original value afterward. A limitation of such an approach is that a busbar fault cannot be detected while postprocessing takes effect.

3.5.4.2 Sensor Fault

The sensor fault is implemented as a sudden increase in v^*_{odi}, the reference voltage for the GFM's voltage controller, corresponding to at least the 10% of its steady-state value. A sudden change above 10% will excite the residual norm sufficiently for our proposed adaptive threshold to detect the fault. Fig. 3.11b and Fig. 3.11d present the impact of the sensor fault in the inverter's output voltage magnitude (v_{oi}) and frequency (ω_i). We notice that the fault is observable in the voltage magnitude rather than in the frequency. The explanation for this phenomenon is the same as the explanation given for the busbar fault in Section 3.5.4.1. Fig. 3.11b shows that the inverter's voltage controller immediately reacts at $t = 2$ s in opposition to the detected increase in v^*_{odi} by reducing the output voltage magnitude v_{odi} and maintaining it around its pre-fault value. A similar situation occurs when the fault is cleared at $t = 3$ s.

Fig. 3.12c presents the responses of the residual norm, dynamic, and fixed thresholds under a v_{odi}^{*} sensor fault. The sensor fault occurs at time $t = 2$ s and is cleared at $t = 3$ s. The adaptive threshold obeys the desired detection logic during the entire horizon. The adaptive threshold remains above the residual norm during fault-free intervals and below the norm during fault occurrence. The proposed adaptive threshold minimizes the rates of false alarms and missed detection to zero. Notice that the adaptive threshold allows for a fast detection of around 0.01 milliseconds. Also, it can be seen that the fixed threshold is tighter than the adaptive threshold. However, the adaptive threshold stays farther from the residual than the fixed threshold. Such a distance may help to avoid false alarms and missed detections under potential new disturbances.

3.5.4.3 Modeling Errors

To account for the influence of modeling errors, we double the resistance (R_{fi}), inductance (L_{fi}), and capacitance (C_{fi}) values of the LC filter. Also, we double the resistance (R_{ci}) and inductance (L_{ci}) values of the output connector. Meanwhile, the adaptive threshold parameters are the same as those presented in Table 3.6. Fig. 3.13a, 3.13b, and 3.13c show the response of the adaptive threshold with modeling errors for the busbar fault and sensor fault, respectively. The figures show that the thresholds still follow the same response as the original ones without errors. The adaptive threshold for busbar fault exhibits a slight positive bias; see Fig. 3.13a and 3.13b. The adaptive threshold for the sensor fault presents a slight negative bias; see Fig. 3.13c.

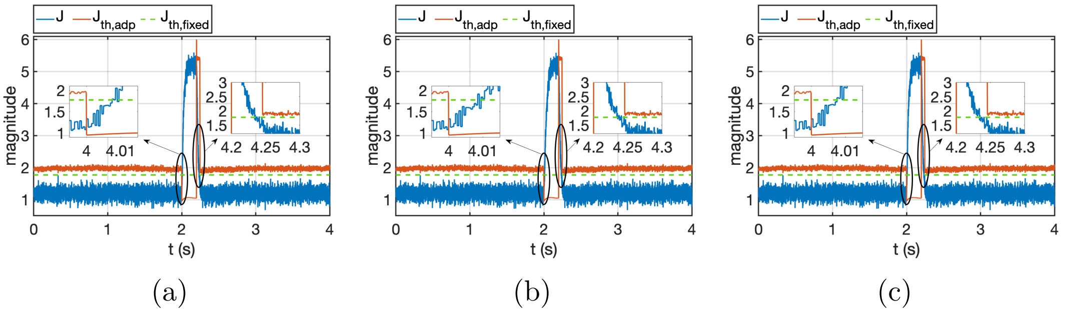

Figure 3.14: Response of the residual norm, fixed threshold, and adaptive threshold with postprocessing and modeling errors under a busbar fault using nonlinear loads with (a) $\mathbf{v} = [v_{bdi}^2 \ \ v_{bqi}^2]^\top$, (b) $\mathbf{v} = [v_{bdi}^4 \ \ v_{bqi}^4]^\top$, and (c) $\mathbf{v} = [v_{bdi} i_{lod_i} \ \ v_{bqi} i_{lod_i}]^\top$.

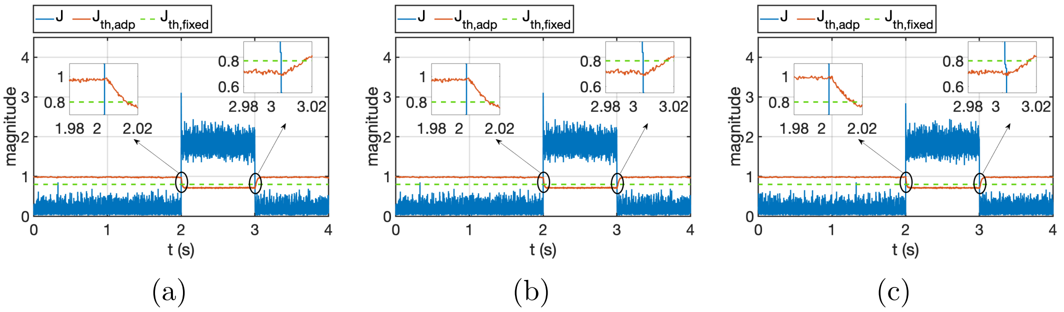

Figure 3.15: Response of the residual norm, fixed threshold, and adaptive threshold with modeling errors under a sensor fault using nonlinear loads with (a) $\mathbf{v} = [v_{bdi}^2 \ \ v_{bqi}^2]^\top$, (b) $\mathbf{v} = [v_{bdi}^4 \ \ v_{bqi}^4]^\top$, and (c) $\mathbf{v} = [v_{bdi} i_{lod_i} \ \ v_{bqi} i_{loq_i}]^\top$.

3.5.4.4 Nonlinear Loads

We evaluate the merits of our proposed adaptive threshold design using three types of nonlinear loads by running experiments for both busbar and sensor faults. In general, the dynamics of the loads in the *dq* domain are expressed as $\dot{\mathbf{i}}_{lo} = J\, \mathbf{i}_{lo} + \mathbf{v}$ where $\mathbf{i}_{lo} = [i_{lodi} \quad i_{loqi}]^\top$, $\mathbf{v} = [v_{bdi} \quad v_{bqi}]^\top$ and

$$J = \begin{bmatrix} -\frac{R_{lo}}{L_{lo}} & \omega_{com} \\ -\omega_{com} & -\frac{R_{lo}}{L_{lo}} \end{bmatrix}.$$

We modify $\mathbf{v}$ as a two-dimensional vector with entries nonlinear in terms of v_{bdi} and v_{bqi} to model the nonlinear models. For these experiments, we consider three types of nonlinear loads defined by $\mathbf{v} = [v_{bdi}^2 \;\; v_{bqi}^2]^\top$, $\mathbf{v} = [v_{bdi}^4 \;\; v_{bqi}^4]^\top$, and $\mathbf{v} = [v_{bdi} i_{lodi} \;\; v_{bqi} i_{loqi}]^\top$. Figures 3.14 and 3.15 show that the response of our adaptive threshold design remains almost invariant to the three types of nonlinear load dynamics across all the experiments. Such a result is congruent with the fault modeling and state-space representation of the inverter, which considers the rest of the microgrid and its components as external entities. Notice that, from the GFM side, the dynamics of the nonlinear loads and other microgrid components show up in the bus voltage magnitudes v_{bdi} and v_{bqi}, which are inputs of the state-space GFM modeling. Despite these results, we acknowledge that other types of nonlinear loads should be used to test the robustness of our approach. Nonetheless, these preliminary results show that our adaptive threshold design achieves an accurate response in the presence of the considered nonlinear loads.

3.5.4.5 Input Delays

In this section, we evaluate the performance of the proposed approach when the input vector $\mathbf{u}$ is delayed d units of time. Notice that three out of five input signals, ω_{com}, ω_{ni}, and V_{ni} might be subject to delays because these signals travel through the communication network established by the secondary control layer. The other two input signals, the dq bus voltage magnitudes (v_{bdi}) and (v_{bqi}), are not influenced by the communication delays because they are physical signals. Figures

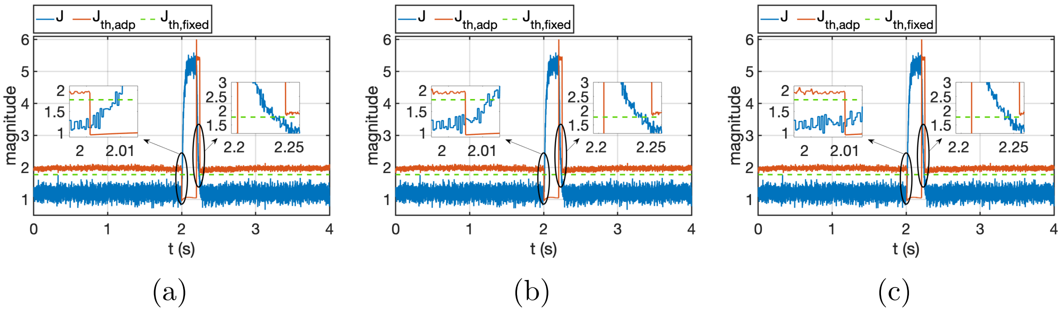

Figure 3.16: Response of the residual norm, fixed threshold, and adaptive threshold with postprocessing and modeling errors under a busbar fault with an input delay of (a) $d = 1$ ms, (b) $d = 5$ ms, and (c) $d = 10$ ms.

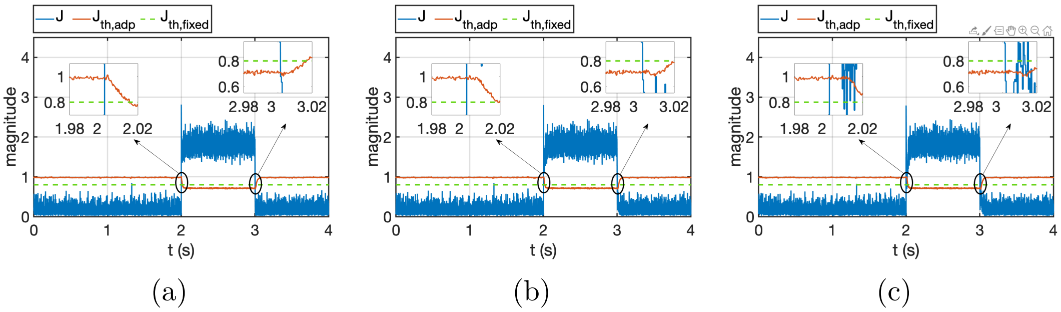

Figure 3.17: Response of the residual norm, fixed threshold, and adaptive threshold with modeling errors under a sensor fault with an input delay of (a) $d = 1$ ms, (b) $d = 5$ ms, and (c) $d = 10$ ms.

3.16 and 3.17 show the response of the residual norm, fixed threshold, and adaptive threshold with postprocessing and modeling errors under a busbar and sensor fault for input delays of 1 ms, 5 ms, and 10 ms. We observe that the input delay setbacks the response of the adaptive threshold proportionally to the value of d. The higher the delay d, the longer the adaptive threshold takes to respond to the fault occurrence or clearance. Figures 3.16a and 3.17a show that the response of the adaptive threshold and residual norm preserve the accuracy of the fault detection logic. However, as shown in Figure 3.17c, when the delay is $d = 10$ ms, both the observer residual and

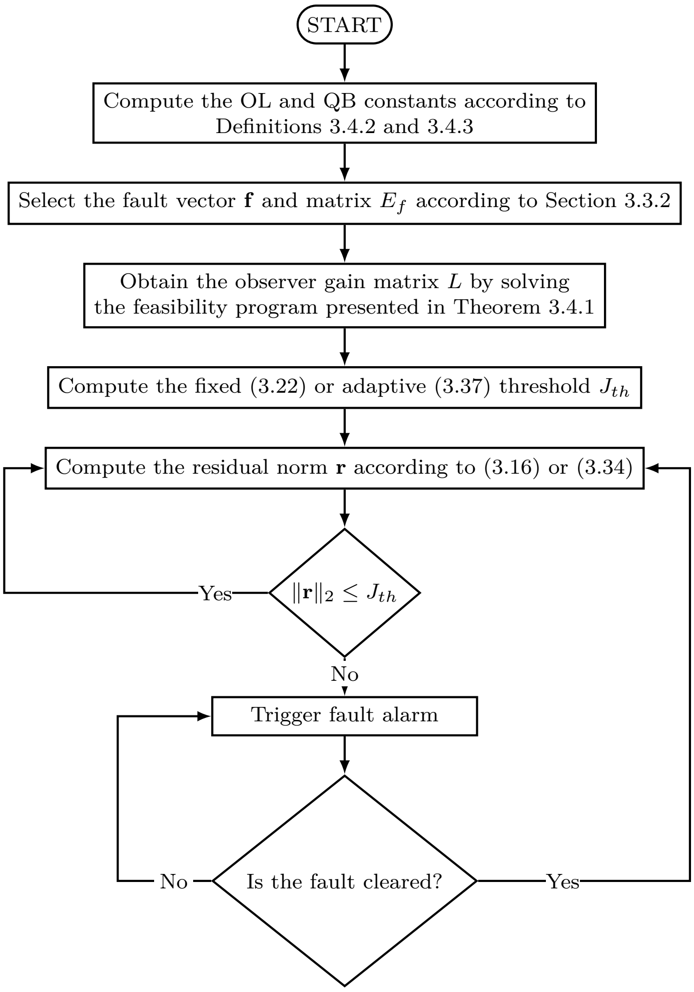
START
Compute the OL and QB constants according to Definitions 3.4.2 and 3.4.3
Select the fault vector $\mathbf{f}$ and matrix E_f according to Section 3.3.2
Obtain the observer gain matrix L by solving the feasibility program presented in Theorem 3.4.1
Compute the fixed (3.22) or adaptive (3.37) threshold J_{th}
Compute the residual norm $\mathbf{r}$ according to (3.16) or (3.34)
$\|\mathbf{r}\|_2 \leq J_{th}$
Yes
No
Trigger fault alarm
Is the fault cleared?
No
Yes

Figure 3.18: Flowchart of the proposed fault detection methods.

adaptive threshold do not synchronize correctly, leading to unwanted outcomes of the detection logic for almost 5 ms.

Figure 3.18 presents the flowchart of our proposed fault detection methods.

3.6 Discussion

The two detection strategies presented in this chapter can be merged into one module that exchanges inputs and outputs with the inverter's sensor and controller. The module can be implemented in real-time within the inverter's embedded microcontroller as code written in any programming language with appropriate software libraries. The processing extra burden exerted over the microcontroller is minimal due to the advancements in computational processing power for microcontrollers. A significant advantage of our approach is that its implementation requires no additional hardware because the module uses signals already measured by the grid-forming inverter. Such a solution is cost-effective, with the extra benefit of making it an entirely internal solution where other external information is not required.

We divide our proposed scheme into four stages to define its complexity and computation burden. The first stage computes the OL and QB constants in less than 20 minutes according to the algorithms in [84] with a complexity of $\mathcal{O}(n^3\, n_{\mathcal{D}})$ and $\mathcal{O}(n^3\, n_{\mathcal{D}}^2)$ respectively, where n is the number of states and $n_{\mathcal{D}}$ is the number of samples taken from the operating region $\mathcal{D}$. It takes approximately 20 minutes to compute the OL and QB constants using the processing power of a MacBook Pro 2019, 2.8 GHz Intel Core i7 processor, 16 GB 2133 MHz LPDDR3 RAM, and 1 TB hard disk drive. The constants need to be recomputed when the operating region of the grid-forming inverter is reduced or expanded as a consequence of modeling the inverter with a simpler or more elaborated state space representation. The second stage solves the semidefinite program posed in Theorem 3.4.1 in less than twenty seconds using primal-dual interior points methods, which have a worst-case complexity estimate of $\mathcal{O}(p^{2.75}K^{1.5})$ where p is the number of variables (states and measurements), and K is the number of constraints [96]. The threshold computation performed in the third stage has a complexity of $\mathcal{O}(t)$ for the fixed thresholding approach, and $\mathcal{O}(p^{2.75}K^{1.5})$ for the adaptive thresholding strategy. Lastly, the fourth stage computes the residual norm online with a complexity of $\mathcal{O}(m)$ where m is the number of the system's measurements.

The works [71], [73], and [97] propose methods similar to our proposed approach because they develop a residual-, observer-, and model-based fault detection strategy using the $\mathcal{H}_-/\mathcal{H}_\infty$ optimization framework with fixed thresholding. However, the main limitation of [71] is that the observers' design targets linear dynamic systems in DC microgrids. The essential drawback of [73] is that the authors need to consider the limitations of the Lipschitz condition while designing the observers for fault detection. In [97], the authors limit their approach to sensor faults and do not study grid-forming inverters. Our proposed fault detection method overcomes these limitations because the observers are designed for the nonlinear dynamics of the GFMs in AC microgrids, considering four different types of faults based on the OL-QB conditions that improve upon the limitation of the state-of-the-art Lipschitz design.

Finally, choosing between a fixed and adaptive threshold depends primarily on the input's dynamics. We suggest the fixed thresholding method in the scenario where the inverters are governed by primary controllers only, and the microgrid conditions are stable. In such a scenario, the input vector, mainly governed by the bus voltage magnitude at the PCC and the voltage and frequency references, changes slowly over time. Hence, the input dynamics can be considered negligible. Otherwise, we recommend considering the adaptive thresholding method.

3.7 Summary

We propose two fault detection strategies using a nonlinear observer design based on the OL and QB conditions with fixed and adaptive thresholding for the emergent grid-forming inverters technology. We derive the matrix expressions of faults and disturbances affecting GFMs and consider them in the observer design process. The internal faults considered in this work are busbar, actuator, inverter bridge, and sensor faults. The first strategy poses a set of LMI constraints and $\mathcal{H}_-/\mathcal{H}_\infty$ optimization to design an observer that achieves sensitivity to faults and robustness against disturbances. The proposed observer design is compared with the state-of-the-art design based on the Lipschitz condition. The association between the Lipschitz and the OL-QB observer is studied theoretically and experimentally, showing that the latter allows for a less restrictive observer design with less computational time. The second strategy presents an adaptive threshold for GFMs in islanded-mode AC microgrids. The proposed threshold is computed as an upper bound on the ℓ_2 norm of the residual vector under a fault-free condition. The bound parameters are successfully obtained by solving a semidefinite program with two constraints of linear matrix inequalities. We demonstrate that the two proposed approaches perform better than the state-of-the-art designs regarding trustworthy detection and computational time. Moreover, leveraging the available signals of typical grid-forming inverters, our proposed strategies do not require additional sensors, yielding a cost-effective solution. Our proposed approach is evaluated with an islanded droop-controlled microgrid. The numerical tests corroborate our proposed approaches' effectiveness and feasibility of real-world implementation.

Chapter 4

Conclusions and future work

4.1 Conclusion

This thesis aims to create and assess new anomaly detection methods to enhance the situational awareness of modern power systems using data mining, machine learning, and observer-based control theory.

Chapter 2 introduces two novel schemes based on the Hoeffding adaptive tree classifier for detecting and identifying cyber and non-cyber contingencies in cyber-physical power systems. The first method constructs a new feature space for labeled energy data via online dictionary learning under the semi-supervised learning framework. The new space consists of extracted patterns from an unlabeled dataset that transforms the labeled data according to the dictionary atoms, delivering valuable information to the HAT classifier. The second method develops an instance selection strategy that works as a wrapper of the HAT classifier, enhancing its capabilities. The selection strategy consists of three actions that allow the HAT classifier to adapt to evolving data distributions with minimal time and memory burden. The extensive numerical results demonstrate the superior performance of our methods compared to the competitors.

Chapter 3 describes two methods for detecting internal faults with fixed and adaptive thresholds for grid-forming inverters operating in islanded AC microgrids. The internal faults considered in this work are the busbar, sensor, actuator, and inverter bridge. We express the mathematical model of the inverters in a nonlinear state-space representation with bounded and parametric uncertainties. The model nonlinear terms are relaxed from satisfying the Lipschitz condition to satisfying the one-sided Lipschitz and quadratic-inner boundedness conditions. The first method designs a nonlinear observer sensitive to faults and robust against disturbances based on the $\mathcal{H}_-/\mathcal{H}_\infty$ optimization framework using the OL and QB conditions. The association between the Lipschitz and the OL-QB conditions in the observer design process is studied theoretically and experimentally, showing that the latter allows for a less restrictive observer design with less computational time. We derive the matrix expressions of faults and disturbances affecting GFMs as part of the alterations in the state-space representation of the inverters' model and consider them in the observer design process. The second method improves upon the first method by introducing an adaptive threshold that follows the behavior of the inverters' input signals. The adaptive threshold is calculated as the upper bound on the ℓ_2 norm of the residual vector in the absence of faults. The bound parameters are obtained as the solution of a semidefinite program with two linear matrix inequalities constraints. We demonstrate that our proposed approaches perform better than the state-of-the-art designs regarding trustworthy detection and computational time. Moreover, leveraging the available signals of typical grid-forming inverters, our approach does not require additional sensors, yielding a cost-effective solution. Our proposed approach is evaluated in inverters operating in small-sized microgrids. The numerical tests corroborate our proposed approaches' effectiveness and feasibility of real-world implementation.

4.2 Future work

The proposed instance selection algorithm in Chapter 2 consists of three algorithmic stages. The first stage relies on reordering the instances based on their spatio-temporal distance to the target. Although instance reordering is an essential component of the first stage, it may degrade the original temporal distribution of the data stream, as shown in [98]. The temporal distribution of the data is crucial because it embeds the actual unknown concept of the data. Reordering the data may cause it to acquire a different concept over time; such a situation represents a different learning problem than the original one. In addition, SIS performs a window size search with a warm restart and stops the search only if the accuracy on a trial set is below a specified threshold. Such a strategy restricts the search around the previous best window size, leading to suboptimal window sizes. The search strategy imposes a trade-off between reducing the searching space and decreasing the complexity of the method to avoid time and memory restrictions. Finally, the selection algorithm introduces four additional hyperparameters that must be tuned according to the CPPS application. Consequently, the researcher either tunes the hyperparameters using an existing preprocessed dataset or tunes the hyperparameters on the fly. We deem it essential to incorporate these considerations as part of future research to avoid degrading the performance of the proposed classifiers based on the Hoeffding adaptive tree.

While our proposed fault detection approaches are convenient at the microgrid level, further analysis is needed for their immediate application to inverter-dominant large-scale power systems. The fundamental reason is that large-scale power systems with high penetration of inverters bring significant stability challenges. Specifically,

1. The dynamics of converters and their controls operate on a similar time scale as the line dynamics, which can result in resonance phenomena and, ultimately, instability [99]. This situation is further aggravated by the coupling of multi-timescale control loops between different inverters' technologies and the numerous lines or devices connected to large-sized power systems.

2. Large-scale power systems may demand longer interconnection lines. In [100], the authors showed that the length of the lines is inversely proportional to the stable penetration of inverter-based resources. They also showed a case study

where a longer transmission line could not support a higher penetration level of inverter-based resources such as grid-forming and grid-following inverters regarding the small-signal stability.

Potential changes in the grid-forming inverters at the parametric and control levels are required to accommodate the aforementioned stability challenges [99]. The parameters of the grid-forming inverter are critical to determine the dynamic behavior of the power-sharing capability, the output filter, the output connector, and the controllers' bandwidth. These parameters must be fine-tuned to meet the power system's stability criteria. Our proposed detection scheme relies on the existence of an observer matrix L that satisfies a couple of linear matrix inequality (LMI) constraints given in Theorem 3.4.1. Notice that the grid-forming inverters' parameters affect the feasibility of such constraints. Such a situation may impair the application of our method to an arbitrary system. In this regard, we recommend conducting a sensitivity analysis of the inverter's parameters to check the feasibility of the LMIs before possibly applying our proposed approach to inverter-dominant large-scale power systems. Moreover, the controllers are responsible for setting the voltage magnitude and frequency supplied to loads and the rest of the microgrid [101]. The advancements in applied control will potentially present new controller designs for grid-forming inverters to reduce the timescale coupling between the controller and the power devices. The new controllers may introduce nonlinearities that can affect the magnitude of the one-sided Lipschitz and quadratic inner boundedness constants from the nonlinear function $\boldsymbol{\phi}$. These constants have a role in determining the existence of the observer matrix gain L. We consider it essential to study the impact of new nonlinearities added to the state space representation of the grid-forming inverter in our proposed detection approach.

Stability challenges may exist in small-scale power systems dominated by power electronics, possibly making it necessary to implement the considerations as mentioned earlier at the microgrid level. However, accommodating the suggested considerations in large-scale power systems is more challenging than in small-scale systems, reinforcing our argument that our proposed approach may not immediately apply to bulk systems. In large-scale power systems, identifying the inverter or set of inverters injecting anomalous dynamics into the grid will likely be carried out only at a geographical level [102]. Furthermore, the ownership mix of inverter-based assets is diverse. Asset owners usually do not have a transparent model of the converter-interfaced resource or its controller [103]. The size of small-scale power systems permits a relatively fast identification and solution of potential stability issues [104]. In this regard, future studies in fault detection for grid-forming inverters should investigate possible solutions to the stability concerns in multiple power converters-based systems at small or large scales.

We have chosen a Luenberger observer design over the stochastic counterparts, such as Kalman or particle filters, mainly for the implementation and design simplicity. The stochastic estimators compute the gain online, whereas Luenberger observers promote an offline computation of the observer matrix gain, reducing the computational efforts at each time step. However, we leave the study of stochastic estimators for fault detection as part of our future endeavors. Such estimators may play an essential role in more complex scenarios. For example, the Luenberger observer design will not be suitable when considering a more elaborate inverter model, which may introduce complex nonlinear system dynamics. Also, Luenberger observers can not handle measurements that are nonlinearly related to the inverter's states or measurements with non-Gaussian noise.

Our proposed approach with an adaptive threshold will be affected by network delays when the grid-forming inverters operate under the regulation of a secondary control layer that relies on a communication network. The reason is that our approach uses the state-space input signals transported through the network's communication channels. Although the convergence of the observer with input delays is guaranteed, its response will be delayed, delaying the residual signal used to compare it with the adaptive threshold. Our goal is to design an adaptive threshold for residual-based fault detection; hence, we leave the design of an observer robust to input delays as part of future endeavors. The designed adaptive threshold performs well with input delays of less than 10 ms but will exhibit a slow response for longer delays. For this reason, an extension to this work would be to assess low-latency communication protocols and their impact on our proposed adaptive threshold for fault detection.

References

[1] I. Žliobaitė, "Combining similarity in time and space for training set formation under concept drift," *Intell. Data Anal.*, vol. 15, p. 589–611, July 2011.

[2] A. Bidram, A. Davoudi, and F. L. Lewis, "A multiobjective distributed control framework for islanded ac microgrids," *IEEE Transactions on Industrial Informatics*, vol. 10, no. 3, pp. 1785–1798, 2014.

[3] A. Bidram, A. Davoudi, F. L. Lewis, and J. M. Guerrero, "Distributed cooperative secondary control of microgrids using feedback linearization," *IEEE Transactions on Power Electronics*, vol. 28, no. 3, pp. 3462–3470, 2013.

[4] D. K. M. Panteli, "Situation awareness in power systems: Theory, challenges and applications," *Electric Power Systems Research*, no. 122, pp. 140–151, 2005.

[5] M. Panteli, D. S. Kirschen, P. A. Crossley, and D. J. Sobajic, "Enhancing situation awareness in power system control centers," in *2013 IEEE International Multi-Disciplinary Conference on Cognitive Methods in Situation Awareness and Decision Support (CogSIMA)*, IEEE, Feb. 2013.

[6] A. Bifet and R. Kirkby, "Data stream mining a practical approach," May 2011.

[7] J. Gama, I. Žliobaitė, A. Bifet, M. Pechenizkiy, and A. Bouchachia, "A survey on concept drift adaptation," *ACM Computing Surveys*, vol. 46, pp. 1–37, Apr. 2014.

[8] "Unifi Consortium." `https://unificonsortium.org/`. [Accessed 04-07-2024].

[9] Q.-C. Zhong and G. Weiss, "Synchronverters: Inverters that mimic synchronous generators," *IEEE Transactions on Industrial Electronics*, vol. 58, pp. 1259–1267, Apr. 2011.

[10] M. Farrokhabadi, C. A. Cañizares, J. W. Simpson-Porco, E. Nasr, L. Fan, P. A. Mendoza-Araya, R. Tonkoski, U. Tamrakar, N. Hatziargyriou, D. Lagos, R. W. Wies, M. Paolone, M. Liserre, L. Meegahapola, M. Kabalan, A. H. Hajimiragha, D. Peralta, M. A. Elizondo, K. P. Schneider, F. K. Tuffner, and J. Reilly, "Microgrid stability definitions, analysis, and examples," *IEEE Transactions on Power Systems*, vol. 35, no. 1, pp. 13–29, 2020.

[11] R. H. Lasseter, Z. Chen, and D. Pattabiraman, "Grid-forming inverters: A critical asset for the power grid," *IEEE Journal of Emerging and Selected Topics in Power Electronics*, vol. 8, no. 2, pp. 925–935, 2020.

[12] G. F. Franklin, J. D. Powell, and A. Emami-Naeini, *Feedback control of dynamic systems.* Upper Saddle River, NJ: Pearson, 7 ed., Apr. 2014.

[13] M. M. S. Khan, J. A. Giraldo, and M. Parvania, "Attack detection in power distribution systems using a cyber-physical real-time reference model," *IEEE Transactions on Smart Grid*, vol. 13, no. 2, pp. 1490–1499, 2022.

[14] I. Zografopoulos and C. Konstantinou, "Detection of malicious attacks in au-

tonomous cyber-physical inverter-based microgrids," *IEEE Transactions on Industrial Informatics*, vol. 18, no. 9, pp. 5815–5826, 2022.

[15] S. Lakshminarayana, S. Adhikari, and C. Maple, "Analysis of iot-based load altering attacks against power grids using the theory of second-order dynamical systems," *IEEE Transactions on Smart Grid*, vol. 12, no. 5, pp. 4415–4425, 2021.

[16] K.-D. Lu and Z.-G. Wu, "Constrained-differential-evolution-based stealthy sparse cyber-attack and countermeasure in an ac smart grid," *IEEE Transactions on Industrial Informatics*, vol. 18, no. 8, pp. 5275–5285, 2022.

[17] U. Adhikari, T. H. Morris, and S. Pan, "Applying non-nested generalized exemplars classification for cyber-power event and intrusion detection," *IEEE Transactions on Smart Grid*, vol. 9, pp. 3928–3941, Sept. 2018.

[18] R. C. Borges Hink, J. M. Beaver, M. A. Buckner, T. Morris, U. Adhikari, and S. Pan, "Machine learning for power system disturbance and cyber-attack discrimination," in *2014 7th International Symposium on Resilient Control Systems (ISRCS)*, pp. 1–8, 2014.

[19] M. Ganjkhani, M. Gilanifar, J. Giraldo, and M. Parvania, "Integrated cyber and physical anomaly location and classification in power distribution systems," *IEEE Transactions on Industrial Informatics*, vol. 17, no. 10, pp. 7040–7049, 2021.

[20] R. Yadav and A. K. Pradhan, “Pca-lstm learning networks with markov chain models for online classification of cyber-induced outages in power system,” *IEEE Systems Journal*, vol. 15, no. 3, pp. 3948–3957, 2021.

[21] M. R. Habibi, H. R. Baghaee, T. Dragičević, and F. Blaabjerg, “Detection of false data injection cyber-attacks in dc microgrids based on recurrent neural networks,” *IEEE Journal of Emerging and Selected Topics in Power Electronics*, vol. 9, no. 5, pp. 5294–5310, 2021.

[22] Y. An and D. Liu, “Multivariate gaussian-based false data detection against cyber-attacks,” *IEEE Access*, vol. 7, pp. 119804–119812, 2019.

[23] A. Gholami, A. Vosughi, and A. K. Srivastava, “Denoising and detection of bad data in distribution phasor measurements using filtering, clustering, and koopman mode analysis,” *IEEE Transactions on Industry Applications*, vol. 58, no. 2, pp. 1602–1610, 2022.

[24] A. Parizad and C. J. Hatziadoniu, “Cyber-attack detection using principal component analysis and noisy clustering algorithms: A collaborative machine learning-based framework,” *IEEE Transactions on Smart Grid*, vol. 13, no. 6, pp. 4848–4861, 2022.

[25] N. Dahal, O. Abuomar, R. King, and V. Madani, “Event stream processing for improved situational awareness in the smart grid,” *Expert Systems with Applications*, vol. 42, pp. 6853–6863, Nov. 2015.

[26] U. Adhikari, T. H. Morris, and S. Pan, "Applying hoeffding adaptive trees for real-time cyber-power event and intrusion classification," *IEEE Transactions on Smart Grid*, vol. 9, pp. 4049–4060, Sept. 2018.

[27] D. Upadhyay, J. Manero, M. Zaman, and S. Sampalli, "Gradient boosting feature selection with machine learning classifiers for intrusion detection on power grids," vol. 18, pp. 1104–1116, Mar. 2021.

[28] E. Hallaji, R. Razavi-Far, M. Wang, M. Saif, and B. Fardanesh, "A stream learning approach for real-time identification of false data injection attacks in cyber-physical power systems," *IEEE Transactions on Information Forensics and Security*, vol. 17, pp. 3934–3945, 2022.

[29] A. Blázquez-García, A. Conde, U. Mori, and J. A. Lozano, "A review on outlier/anomaly detection in time series data," *ACM Computing Surveys*, vol. 54, p. 1–33, Apr. 2021.

[30] H. Gomes, J. Read, A. Bifet, J. Barddal, and J. Gama, "Machine learning for streaming data: state of the art, challenges, and opportunities," *ACM SIGKDD Explorations Newsletter*, vol. 2, no. 21, pp. 6–22, 2019.

[31] J. Gama, R. Sebastião, and P. P. Rodrigues, "On evaluating stream learning algorithms," *Machine Learning*, vol. 90, pp. 317–346, Oct. 2012.

[32] A. Bifet and R. Gavaldà, "Adaptive learning from evolving data streams," pp. 249–260, Springer Berlin Heidelberg, 2009.

[33] A. Bifet and R. Gavaldà, "Learning from time-changing data with adaptive windowing," in *Proceedings of the 2007 SIAM International Conference on Data Mining*, Society for Industrial and Applied Mathematics, Apr. 2007.

[34] J. Gama, P. Medas, G. Castillo, and P. Rodrigues, "Learning with drift detection," in *Advances in Artificial Intelligence – SBIA 2004*, pp. 286–295, Springer Berlin Heidelberg, 2004.

[35] U. Adhikari, S. Pan, T. H. Morris, and J. Beave, "Industrial control system (ics) cyber attack datasets, dataset 1: Power system datasets." `https://sites.google.com/a/uah.edu/tommy-morris-uah/ics-data-sets`. Accessed: 2020-08-11.

[36] I. Žliobaitė, A. Bifet, J. Read, B. Pfahringer, and G. Holmes, "Evaluation methods and decision theory for classification of streaming data with temporal dependence," *Machine Learning*, vol. 98, pp. 455–482, Apr. 2014.

[37] K. Nigam, A. K. Mccallum, S. Thrun, and T. Mitchell *Machine Learning*, vol. 39, no. 2/3, pp. 103–134, 2000.

[38] J. Mairal, F. Bach, J. Ponce, and G. Sapiro, "Online dictionary learning for sparse coding," in *Proceedings of the 26th Annual International Conference on Machine Learning - ICML '09*, ACM Press, 2009.

[39] A. Bifet, R. Gavaldà, G. Holmes, and B. Pfahringer, *Machine Learning for Data Streams.* The MIT Press, 2018.

[40] F. Liu, J. Ma, R. Zhao, and Q. Wang, "Online dictionary self-taught learning for hyperspectral image classification," in *2018 IEEE International Instrumentation and Measurement Technology Conference (I2MTC)*, IEEE, May 2018.

[41] R. Raina, A. Battle, H. Lee, B. Packer, and A. Y. Ng, "Self-taught learning," in *Proceedings of the 24th international conference on Machine learning - ICML '07*, ACM Press, 2007.

[42] A. Bifet, G. Holmes, R. Kirkby, and B. Pfahringer, "Moa: Massive online analysis," *J. Mach. Learn. Res.*, vol. 11, p. 1601–1604, Aug. 2010.

[43] M. Kordos, *Instance Selection in Machine Learning: New Directions in Similarity-based, Evolutionary and Embedded Methods.* 43-309 Bielsko-Biała, ul. Willowa 2: University of Bielsko-Biala, 2019.

[44] "Ten little algorithms, part 3: Welford's method (and friends)." `https://www.embeddedrelated.com/showarticle/785.php`. Accessed: 2021-10-17.

[45] A. Bifet, G. Holmes, B. Pfahringer, P. Kranen, H. Kremer, T. Jansen, and T. Seidl, "Moa: Massive online analysis, a framework for stream classification and clustering," in *Proceedings of the First Workshop on Applications of Pattern Analysis*, vol. 11, pp. 44–50, PMLR, 01–03 Sep 2010.

[46] J. Montiel, M. Halford, S. M. Mastelini, G. Bolmier, R. Sourty, R. Vaysse, A. Zouitine, H. M. Gomes, J. Read, T. Abdessalem, and A. Bifet, "River:

machine learning for streaming data in python," *ArXiv*, vol. abs/2012.04740, 2020.

[47] P. Domingos and G. Hulten, "Mining high-speed data streams," in *Proceedings of the Sixth ACM SIGKDD International Conference on Knowledge Discovery and Data Mining*, KDD '00, (New York, NY, USA), p. 71–80, Association for Computing Machinery, 2000.

[48] M. Harries and N. S. Wales, "Splice-2 comparative evaluation: Electricity pricing," tech. rep., University of New South Wales, 1999.

[49] S. Pan, T. Morris, and U. Adhikari, "Developing a hybrid intrusion detection system using data mining for power systems," *IEEE Transactions on Smart Grid*, vol. 6, pp. 3104–3113, Nov. 2015.

[50] D. Wang, X. Wang, Y. Zhang, and L. Jin, "Detection of power grid disturbances and cyber-attacks based on machine learning," *Journal of Information Security and Applications*, vol. 46, pp. 42–52, 2019.

[51] G. Intriago and Y. Zhang, "Online dictionary learning based fault and cyber attack detection for power systems," in *2021 IEEE Power and Energy Society (PES) General Meeting*, IEEE, 2021.

[52] J. C. Cepeda, J. L. Rueda, I. Erlich, and D. G. Colomé, "Probabilistic approach-based pmu placement for real-time power system vulnerability as-

sessment," in *2012 3rd IEEE PES Innovative Smart Grid Technologies Europe (ISGT Europe)*, pp. 1–8, 2012.

[53] B. Fahimi, A. Kwasinski, A. Davoudi, R. Balog, and M. Kiani, "Charge it!," *IEEE Power and Energy Magazine*, vol. 9, no. 4, pp. 54–64, 2011.

[54] T.-T. Ku, C.-H. Lin, C.-S. Chen, and C.-T. Hsu, "Coordination of transformer on-load tap changer and PV smart inverters for voltage control of distribution feeders," *IEEE Transactions on Industry Applications*, vol. 55, pp. 256–264, Jan. 2019.

[55] D. Ramasubramanian, W. Wang, P. Pourbeik, E. Farantatos, A. Gaikwad, S. Soni, and V. Chadliev, "Positive sequence voltage source converter mathematical model for use in low short circuit systems," *IET Generation, Transmission and Distribution*, vol. 14, pp. 87–97, Dec. 2019.

[56] Y. Zhang, Y. Han, C. Wang, J. Wang, and Q. Zhao, "A dynamic threshold method for wind turbine fault detection based on spatial-temporal neural network," *J. Renew. Sustain. Energy*, vol. 14, p. 053304, Sept. 2022.

[57] Q. He, Y. Pang, G. Jiang, and P. Xie, "A spatio-temporal multiscale neural network approach for wind turbine fault diagnosis with imbalanced SCADA data," *IEEE Trans. Industr. Inform.*, vol. 17, pp. 6875–6884, Oct. 2021.

[58] F. Deng, M. Jin, C. Liu, M. Liserre, and W. Chen, "Switch open-circuit fault localization strategy for mmcs using sliding-time window based features extrac-

tion algorithm," *IEEE Transactions on Industrial Electronics*, vol. 68, no. 10, pp. 10193–10206, 2021.

[59] Y. Han, W. Qi, N. Ding, and Z. Geng, "Short-time wavelet entropy integrating improved lstm for fault diagnosis of modular multilevel converter," *IEEE Transactions on Cybernetics*, vol. 52, no. 8, pp. 7504–7512, 2022.

[60] S. Zhang, R. Wang, Y. Si, and L. Wang, "An improved convolutional neural network for three-phase inverter fault diagnosis," *IEEE Trans. Instrum. Meas.*, vol. 71, pp. 1–15, Nov. 2022.

[61] Q. Lin, S. Chen, and C.-M. Lin, "Parametric fault diagnosis based on fuzzy cerebellar model neural networks," *IEEE Trans. on Power Electron.*, vol. 66, pp. 8104–8115, Oct. 2019.

[62] W.-C. Wang, L. Kou, Q.-D. Yuan, J.-N. Zhou, C. Liu, and G.-W. Cai, "An intelligent fault diagnosis method for open-circuit faults in power-electronics energy conversion system," *IEEE Access*, vol. 8, pp. 221039–221050, Dec. 2020.

[63] M. A. Jarrahi, H. Samet, and T. Ghanbari, "Novel change detection and fault classification scheme for ac microgrids," *IEEE Systems Journal*, vol. 14, no. 3, pp. 3987–3998, 2020.

[64] R. Yadav, A. K. Pradhan, and I. Kamwa, "Real-time multiple event detection and classification in power system using signal energy transformations," *IEEE Transactions on Industrial Informatics*, vol. 15, no. 3, pp. 1521–1531, 2019.

[65] I. Sadeghkhani, M. E. Hamedani Golshan, A. Mehrizi-Sani, J. M. Guerrero, and A. Ketabi, “Transient monitoring function–based fault detection for inverter-interfaced microgrids,” *IEEE Transactions on Smart Grid*, vol. 9, no. 3, pp. 2097–2107, 2018.

[66] N. K. Sharma, S. R. Samantaray, and C. N. Bhende, “Vmd-enabled current-based fast fault detection scheme for dc microgrid,” *IEEE Systems Journal*, vol. 16, no. 1, pp. 933–944, 2022.

[67] R. Bhargav, C. P. Gupta, and B. R. Bhalja, “Unified impedance-based relaying scheme for the protection of hybrid ac/dc microgrid,” *IEEE Transactions on Smart Grid*, vol. 13, no. 2, pp. 913–927, 2022.

[68] Q.-M. Xiao, M.-F. Guo, and D.-Y. Chen, “High-impedance fault detection method based on one-dimensional variational prototyping-encoder for distribution networks,” *IEEE Systems Journal*, vol. 16, no. 1, pp. 966–976, 2022.

[69] D. U. Campos-Delgado and D. R. Espinoza-Trejo, “An observer-based diagnosis scheme for single and simultaneous open-switch faults in induction motor drives,” *IEEE Transactions on Industrial Electronics*, vol. 58, no. 2, pp. 671–679, 2011.

[70] N. Hawkins, N. Jewell, M. Alqatamin, B. Bhagwat, and M. McIntyre, “A nonlinear fault detection scheme for pv applications,” in *2020 American Control Conference (ACC)*, pp. 3188–3192, 2020.

[71] T. Wang, L. Liang, S. K. Gurumurthy, F. Ponci, A. Monti, Z. Yang, and R. W. De Doncker, "Model-based fault detection and isolation in dc microgrids using optimal observers," *IEEE Journal of Emerging and Selected Topics in Power Electronics*, vol. 9, no. 5, pp. 5613–5630, 2021.

[72] G. Anagnostou, F. Boem, S. Kuenzel, B. C. Pal, and T. Parisini, "Observer-based anomaly detection of synchronous generators for power systems monitoring," *IEEE Transactions on Power Systems*, vol. 33, no. 4, pp. 4228–4237, 2018.

[73] M. A. Shoaib, A. Q. Khan, G. Mustafa, S. T. Gul, O. Khan, and A. S. Khan, "A framework for observer-based robust fault detection in nonlinear systems with application to synchronous generators in power systems," *IEEE Transactions on Power Systems*, vol. 37, pp. 1044–1053, Mar. 2022.

[74] H. Yin, Y. Chen, Z. Chen, and M. Li, "Adaptive fast fault location for open-switch faults of voltage source inverter," *IEEE Trans. Circuits Syst. I: Regular Papers*, vol. 68, pp. 3965–3974, Sept. 2021.

[75] W. Zhang, Y. He, and J. Chen, "A robust open-circuit fault diagnosis method for three-level t-type inverters based on phase voltage vector residual under modulation mode switching," *IEEE Trans. on Power Electronics*, vol. 38, pp. 5309–5322, Apr. 2023.

[76] H. Yin, Y. Chen, and Z. Chen, "Observer-based adaptive threshold diagnosis

method for open-switch faults of voltage source inverters," *Journal of Power Electronics*, vol. 20, pp. 1573–1582, Aug. 2020.

[77] X. Ding, J. Poon, I. Celanovic, and A. D. Dominguez-Garcia, "Fault detection and isolation filters for three-phase AC-DC power electronics systems," *IEEE Trans. Circuits Syst. I: Regular Papers*, vol. 60, pp. 1038–1051, Apr. 2013.

[78] M. Huang, L. Ding, W. Li, C.-Y. Chen, and Z. Liu, "Distributed observer-based fault-tolerant control for DC microgrids with sensor fault," *IEEE Trans. Circuits Syst. I: Regular Papers*, vol. 68, pp. 1659–1670, Apr. 2021.

[79] N. Pico, S.-H. Park, J. sup Yi, and H. Moon, "Six-wheel robot design methodology and emergency control to prevent the robot from falling down the stairs," *Applied Sciences*, vol. 12, p. 4403, Apr. 2022.

[80] Z. Wang and Y. Shen, "Residual evaluation based on threshold computation," in *Studies in Systems, Decision and Control*, pp. 61–83, Springer Nature Singapore, Oct. 2022.

[81] S. F. Zarei, H. Mokhtari, and F. Blaabjerg, "Fault detection and protection strategy for islanded inverter-based microgrids," *IEEE Journal of Emerging and Selected Topics in Power Electronics*, vol. 9, no. 1, pp. 472–484, 2021.

[82] M. Abbaszadeh and H. J. Marquez, "Nonlinear observer design for one-sided lipschitz systems," in *Proceedings of the 2010 American Control Conference*, IEEE, June 2010.

[83] W. Zhang, H. Su, H. Wang, and Z. Han, “Full-order and reduced-order observers for one-sided lipschitz nonlinear systems using riccati equations,” *Communications in Nonlinear Science and Numerical Simulation*, vol. 17, pp. 4968–4977, Dec. 2012.

[84] J. Qi, A. F. Taha, and J. Wang, “Comparing kalman filters and observers for power system dynamic state estimation with model uncertainty and malicious cyber attacks,” *IEEE Access*, vol. 6, pp. 77155–77168, 2018.

[85] S. X. Ding, *Model-Based Fault Diagnosis Techniques.* Springer London, 2013.

[86] J. Xiao, L. Wang, Z. Qin, and P. Bauer, “A resilience enhanced secondary control for ac micro-grids,” *IEEE Transactions on Smart Grid*, pp. 1–1, 2023.

[87] A. Intriago, F. Liberati, N. D. Hatziargyriou, and C. Konstantinou, “Residual-based detection of attacks in cyber-physical inverter-based microgrids,” *IEEE Transactions on Power Systems*, pp. 1–18, 2023.

[88] G. Intriago, R. Intriago, and Y. Zhang, “Frequency cyber-attack detection for droop-controlled grid-forming inverters,” in *2023 IEEE Power and Energy Society General Meeting*, 2023.

[89] X. Liu, Z. Zou, J. Tang, Z. Wang, and M. Cheng, “Modeling and stability analysis of converter-based power systems,” in *2021 IEEE Sustainable Power and Energy Conference (iSPEC)*, IEEE, Dec. 2021.

[90] M. Buciakowski, M. Witczak, V. Puig, D. Rotondo, F. Nejjari, and J. Korbicz,

"A bounded-error approach to simultaneous state and actuator fault estimation for a class of nonlinear systems," *Journal of Process Control*, vol. 52, pp. 14–25, Apr. 2017.

[91] E. Ghahremani and I. Kamwa, "Dynamic state estimation in power system by applying the extended kalman filter with unknown inputs to phasor measurements," *IEEE Transactions on Power Systems*, vol. 26, no. 4, pp. 2556–2566, 2011.

[92] NEPLAN, "Exciter Models." `https://www.neplan.ch/wp-content/uploads/2015/08/Nep_EXCITERS1.pdf`.

[93] PowerWorld, "Block Diagrams." `https://www.powerworld.com/files/Block-Diagrams-18.pdf`.

[94] A. Sajadi, R. W. Kenyon, and B.-M. Hodge, "Synchronization in electric power networks with inherent heterogeneity up to 100% inverter-based renewable generation," *Nature Communications*, vol. 13, May 2022.

[95] M. Peet, "Lmi methods in optimal and robust control."

[96] S. Boyd, L. El Ghaoui, E. Feron, and V. Balakrishnan, *Linear matrix inequalities in system and control theory.* Society for Industrial and Applied Mathematics, Jan. 1994.

[97] F. Mehmood, P. M. Papadopoulos, L. Hadjidemetriou, A. Charalambous, and M. M. Polycarpou, "Model-based fault diagnosis scheme for current and volt-

age sensors in grid side converters," *IEEE Transactions on Power Electronics*, vol. 38, p. 5360–5375, Apr. 2023.

[98] I. Žliobaitė, "Controlled permutations for testing adaptive classifiers," in *Discovery Science* (T. Elomaa, J. Hollmén, and H. Mannila, eds.), (Berlin, Heidelberg), pp. 365–379, Springer Berlin Heidelberg, 2011.

[99] F. Dörfler and D. Groß, "Control of low-inertia power systems," *Annual Review of Control, Robotics, and Autonomous Systems*, vol. 6, pp. 415–445, May 2023.

[100] L. Ding, X. Lu, and J. Tan, "Comparative small-signal stability analysis of grid-forming and grid-following inverters in low-inertia power systems," in *IECON 2021 – 47th Annual Conference of the IEEE Industrial Electronics Society*, pp. 1–6, 2021.

[101] J. Rocabert, A. Luna, F. Blaabjerg, and P. Rodríguez, "Control of power converters in AC microgrids," *IEEE Transactions on Power Electronics*, vol. 27, pp. 4734–4749, Nov. 2012.

[102] C. Wang, C. Mishra, K. D. Jones, R. M. Gardner, and L. Vanfretti, "Identifying oscillations injected by inverter-based solar energy sources," in *2022 IEEE Power & Energy Society General Meeting (PESGM)*, pp. 1–5, 2022.

[103] C. Mishra, D. Yang, C. Wang, X. Xu, K. D. Jones, R. Matthew Gardner, and L. Vanfretti, "Analysis of statcom oscillations using ambient synchrophasor

data in dominion energy," in *2022 IEEE Power & Energy Society Innovative Smart Grid Technologies Conference (ISGT)*, pp. 1–5, 2022.

[104] Q. Peng, Q. Jiang, Y. Yang, T. Liu, H. Wang, and F. Blaabjerg, "On the stability of power electronics-dominated systems: Challenges and potential solutions," *IEEE Transactions on Industry Applications*, vol. 55, no. 6, pp. 7657–7670, 2019.

Appendix A

Proof of Theorems in Chapter 3

A.1 Proof of Theorem 3.4.1

Proof. Let us choose the following candidate Lyapunov function $Z = \mathbf{e}^\top P\mathbf{e}$ with $P > 0$ to prove the internal stability of the residual generator (3.33) in the fault-free case. The time derivative of V is

$$\begin{aligned}\dot{Z} &= \mathbf{e}^\top P\bar{E}_w\mathbf{w} + \mathbf{e}^\top(\bar{A}^\top P + P\bar{A})\mathbf{e} + \mathbf{w}^\top\bar{E}_w^\top P\mathbf{e} \\ &\quad + \mathbf{e}^\top P\Phi + \Phi^\top P\mathbf{e}.\end{aligned} \tag{A.1}$$

Given $\epsilon_1 > 0$ and $\epsilon_2 > 0$, the conditions (3.26) and (3.27) can be expressed equivalently as

$$\Phi^\top\mathbf{e} \leq \rho\mathbf{e}^\top\mathbf{e} \Leftrightarrow \epsilon_1\left(\rho\mathbf{e}^\top\mathbf{e} - \Phi^\top\mathbf{e}\right) \geq 0, \tag{A.2}$$

$$\Phi^\top \Phi \leq \varphi \mathbf{e}^\top \Phi + \delta \mathbf{e}^\top \mathbf{e} \Leftrightarrow \epsilon_2(\delta \mathbf{e}^\top \mathbf{e} + \varphi \mathbf{e}^\top \Phi - \Phi^\top \Phi) \geq 0. \tag{A.3}$$

Adding (A.2) and (A.3) to the right-hand side of (A.1), we have:

$$\begin{aligned} \dot{Z} \leq \mathbf{w}^\top \bar{E}_w^\top P\mathbf{e} + \mathbf{e}^\top (\bar{A}^\top P + P\bar{A})\mathbf{e} + \mathbf{e}^\top P\bar{E}_w \mathbf{w} \\ + \Phi^\top P\mathbf{e} + \mathbf{e}^\top P\Phi + \epsilon_1 \rho \mathbf{e}^\top \mathbf{e} - \epsilon_1 \Phi^\top \mathbf{e} \\ + \epsilon_2 \delta\, \mathbf{e}^\top \mathbf{e} + \epsilon_2 \varphi\, \mathbf{e}^\top \Phi - \epsilon_2 \Phi^\top \Phi \end{aligned} \tag{A.4}$$

Rewriting (A.4) as in a matrix inequality:

$$\dot{Z} \leq \begin{bmatrix} \mathbf{e} \\ \mathbf{w} \\ \mathbf{\Phi} \end{bmatrix}^\top \underbrace{\begin{bmatrix} (\bar{A}^\top P + P\bar{A}) & P\bar{E}_w & P + \frac{1}{2}(\epsilon_2 \varphi - \epsilon_1)I \\ (\epsilon_1 \rho + \epsilon_2 \delta)I & & \\ \bar{E}_w^\top P & 0 & 0 \\ P + \frac{1}{2}(\epsilon_2 \varphi - \epsilon_1)I & 0 & -\epsilon_2 I \end{bmatrix}}_{\mathbf{M}} \begin{bmatrix} \mathbf{e} \\ \mathbf{w} \\ \mathbf{\Phi} \end{bmatrix}. \tag{A.5}$$

Hence, $\dot{Z} < 0$ if $M < 0$. Considering that $Z > 0$ and $\mathbf{r}_w$ in (3.20), we can satisfy constraint (3.18) by rewriting it as:

$$\begin{aligned} \int_0^t \left(\dot{Z} + \mathbf{r}_w^\top \mathbf{r}_w - \alpha^2\, \mathbf{w}^\top \mathbf{w} \right) dt \leq 0 \\ \dot{Z} + \mathbf{r}_w^\top \mathbf{r}_w - \alpha^2\, \mathbf{w}^\top \mathbf{w} \leq 0 \\ \mathbf{e}^\top \bar{C}^\top \bar{C}\mathbf{e} - \alpha^2\, \mathbf{w}^\top \mathbf{w} + \mathbf{e}^\top \bar{C}^\top \bar{F}_w \mathbf{w} \\ + \dot{Z} + \mathbf{w}^\top \bar{F}_w^\top \bar{F}_w \mathbf{w} + \mathbf{w}^\top \bar{F}_w \bar{C}\mathbf{e} \leq 0. \end{aligned} \tag{A.6}$$

Assuming zero initial conditions, combining (A.6) with (A.5) we have:

$$\dot{Z} \leq \begin{bmatrix} \mathbf{e} \\ \mathbf{w} \\ \mathbf{\Phi} \end{bmatrix}^\top \underbrace{\begin{bmatrix} \begin{array}{l} (\bar{A}^\top P + P\bar{A}) + \bar{C}^\top \bar{C} \\ \quad (\epsilon_1 \rho + \epsilon_2 \delta) I \end{array} & P\bar{E}_w + \bar{C}^\top \bar{F}_w & P + \frac{1}{2}(\epsilon_2 \varphi - \epsilon_1) I \\ \bar{E}_w^\top P + \bar{F}_w \bar{C} & -\alpha^2 I + \bar{F}_w^\top \bar{F}_w & 0 \\ P + \frac{1}{2}(\epsilon_2 \varphi - \epsilon_1) I & 0 & -\epsilon_2 I \end{bmatrix}}_{\mathbf{M}^*} \begin{bmatrix} \mathbf{e} \\ \mathbf{w} \\ \mathbf{\Phi} \end{bmatrix}. \tag{A.7}$$

If $\mathbf{M}^* < 0$, then $\dot{Z} < 0$, which means that the residual generator is asymptotically stable in the Lyapunov sense. Therefore, the inequality $\mathbf{M}^* < 0$ is equivalent to (3.28).

Similarly, defining the Lyapunov function $Y = \mathbf{e}^\top Q \mathbf{e}$ with $Q > 0$ to demonstrate the internal stability of (3.33) in the disturbance-free case:

$$\begin{aligned} \dot{Y} = \mathbf{e}^\top (\bar{A}^\top P + P\bar{A})\mathbf{e} + \mathbf{e}^\top P\bar{E}_f \mathbf{f} + \mathbf{f}^\top \bar{E}_f^\top P \mathbf{e} \\ + \mathbf{e}^\top P \Phi + \Phi^\top P \mathbf{e}. \end{aligned} \tag{A.8}$$

Adding (A.2), and (A.3) with strictly positive scalars ϵ_3 and ϵ_4 to the right-hand side of (A.8):

$$\begin{aligned} \dot{Y} \leq \mathbf{f}^\top \bar{E}_f^\top P \mathbf{e} + \mathbf{e}^\top P \bar{E}_f \mathbf{f} + \mathbf{e}^\top (\bar{A}^\top P + P\bar{A})\mathbf{e} \\ + \Phi^\top P \mathbf{e} + \epsilon_3 \rho \mathbf{e}^\top \mathbf{e} + \mathbf{e}^\top P \Phi - \epsilon_3 \Phi^\top \mathbf{e} \\ + \epsilon_4 \delta\, \mathbf{e}^\top \mathbf{e} + \epsilon_4 \varphi\, \mathbf{e}^\top \Phi - \epsilon_4 \Phi^\top \Phi. \end{aligned} \tag{A.9}$$

Conducting a similar derivation for constraint (3.19) with Schur complements and elementary manipulations yields the matrix inequality (3.29). □

A.2 Proof of Theorem 3.4.2

Proof. The Lipschitz condition implies the OL and QB conditions [82]. Using the Cauchy-Schwarz inequality and the assumption that $\boldsymbol{\phi}(\mathbf{x}, \mathbf{u})$ is nonlinear satisfying the Lipschitz condition in $\mathcal{U} \times \mathcal{D}$, we obtain:

$$\begin{aligned}|\langle \hat{\mathbf{x}} - \mathbf{x}, \boldsymbol{\phi}(\hat{\mathbf{x}}, \mathbf{u}) - \boldsymbol{\phi}(\mathbf{x}, \mathbf{u}) \rangle| &\leq \|\hat{\mathbf{x}} - \mathbf{x}\| \|\boldsymbol{\phi}(\hat{\mathbf{x}}, \mathbf{u}) - \boldsymbol{\phi}(\mathbf{x}, \mathbf{u})\| \\ &\leq \gamma \|\hat{\mathbf{x}} - \mathbf{x}\|^2.\end{aligned}$$

The OL constant ρ can be set equal to $\pm\gamma$ based on Definition 3.4.2. Similarly, using Definition 3.4.3 we get:

$$\begin{aligned}\|\boldsymbol{\phi}(\hat{\mathbf{x}}, \mathbf{u}) - \boldsymbol{\phi}(\mathbf{x}, \mathbf{u})\|^2 &\leq \varphi \langle \boldsymbol{\phi}(\mathbf{x}, \mathbf{u}) - \boldsymbol{\phi}(\hat{\mathbf{x}}, \mathbf{u}), \mathbf{x} - \hat{\mathbf{x}} \rangle \\ &\quad + \delta \|\hat{\mathbf{x}} - \mathbf{x}\|^2 \\ &\leq (\delta + \varphi\rho) \|\mathbf{x} - \hat{\mathbf{x}}\|^2 .\end{aligned}$$

We can obtain the value of δ by setting $\gamma^2 = (\delta + \varphi\rho)$. Notice that the previous inequality is valid if $\varphi > 0$. By comparing (3.28) with (3.24), we establish the following relations: $\epsilon_1 = \varepsilon_1 \varphi$, $\epsilon_2 = \varepsilon_1$, and $\gamma^2 = \delta + \varphi\rho$. Given that $\varphi > 0$, then $\epsilon_1 > 0$. A similar analysis can be done by using the entries of inequalities (3.29) and (3.25). □

A.3 Proof of Theorem 3.5.1

Proof. Define $V = \tilde{\mathbf{e}}^\top P\,\tilde{\mathbf{e}}$, $W = \tilde{\mathbf{w}}^\top \tilde{\mathbf{w}}$, and $U = \tilde{\mathbf{u}}^\top \tilde{\mathbf{u}}$. We propose an upper bound for the residual norm square $\mathbf{r}^\top \mathbf{r}$ with $\gamma > 0$

$$\begin{aligned} \mathbf{r}^\top \mathbf{r} &\leq \gamma \times (V + W + U) \\ &= \gamma \times \begin{bmatrix} \tilde{\mathbf{e}} \\ \tilde{\mathbf{w}} \\ \tilde{\mathbf{u}} \end{bmatrix}^\top \begin{bmatrix} P & 0 & 0 \\ 0 & I & 0 \\ 0 & 0 & I \end{bmatrix} \begin{bmatrix} \tilde{\mathbf{e}} \\ \tilde{\mathbf{w}} \\ \tilde{\mathbf{u}} \end{bmatrix}. \end{aligned} \tag{A.10}$$

According to (3.34), $\mathbf{r}^\top \mathbf{r}$ can be rewritten as

$$\mathbf{r}^\top \mathbf{r} = \begin{bmatrix} \tilde{\mathbf{e}} \\ \tilde{\mathbf{w}} \\ \tilde{\mathbf{u}} \end{bmatrix}^\top \begin{bmatrix} \widetilde{C}^\top \\ \widetilde{F}_w^\top \\ \widetilde{D}^\top \end{bmatrix} \begin{bmatrix} \widetilde{C} & \widetilde{F}_w & \widetilde{D} \end{bmatrix} \begin{bmatrix} \tilde{\mathbf{e}} \\ \tilde{\mathbf{w}} \\ \tilde{\mathbf{u}} \end{bmatrix}. \tag{A.11}$$

Combining (A.11) and (A.10), we get

$$\begin{bmatrix} \tilde{\mathbf{e}} \\ \tilde{\mathbf{w}} \\ \tilde{\mathbf{u}} \end{bmatrix}^\top \left(\begin{bmatrix} P & 0 & 0 \\ 0 & I & 0 \\ 0 & 0 & I \end{bmatrix} - \frac{1}{\gamma} \begin{bmatrix} \widetilde{C}^\top \\ \widetilde{F}_w^\top \\ \widetilde{D}^\top \end{bmatrix} \begin{bmatrix} \widetilde{C} & \widetilde{F}_w & \widetilde{D} \end{bmatrix} \right) \begin{bmatrix} \tilde{\mathbf{e}} \\ \tilde{\mathbf{w}} \\ \tilde{\mathbf{u}} \end{bmatrix} \geq 0, \tag{A.12}$$

which is equivalent to (3.35) by the Schur complement [96]. Consider the first-order derivative of V

$$\begin{aligned}\dot{V} &= \dot{\tilde{\mathbf{e}}}^\top P\tilde{\mathbf{e}} + \tilde{\mathbf{e}}^\top P\dot{\tilde{\mathbf{e}}} \\ &= \left(\tilde{\mathbf{e}}^\top \widetilde{A}^\top + \tilde{\mathbf{u}}^\top \widetilde{B}^\top + \tilde{\mathbf{w}}^\top \widetilde{E}_w^\top + \widetilde{\boldsymbol{\Phi}}^\top\right) P\tilde{\mathbf{e}} \\ &\quad + \tilde{\mathbf{e}}^\top P\left(\widetilde{A}\tilde{\mathbf{e}} + \widetilde{B}\tilde{\mathbf{u}} + \widetilde{E}_w\tilde{\mathbf{w}} + \widetilde{\boldsymbol{\Phi}}\right) \\ &= \begin{bmatrix} \tilde{\mathbf{e}} \\ \tilde{\mathbf{w}} \\ \tilde{\mathbf{u}} \\ \widetilde{\boldsymbol{\Phi}} \end{bmatrix}^\top \begin{bmatrix} \widetilde{A}^\top P + P\widetilde{A} & P\widetilde{E}_w & P\widetilde{B} & P \\ \widetilde{E}_w^\top P & 0 & 0 & 0 \\ \widetilde{B}^\top P & 0 & 0 & 0 \\ P & 0 & 0 & 0 \end{bmatrix} \begin{bmatrix} \tilde{\mathbf{e}} \\ \tilde{\mathbf{w}} \\ \tilde{\mathbf{u}} \\ \widetilde{\boldsymbol{\Phi}} \end{bmatrix}. \end{aligned} \tag{A.13}$$

Given an appropriate value for α, $\dot{V}$ can be upper-bounded as

$$\dot{V} \leq -\alpha V + \tilde{\mathbf{u}}^\top \tilde{\mathbf{u}}, \tag{A.14}$$

which can be rewritten as:

$$\begin{bmatrix} \tilde{\mathbf{e}} \\ \tilde{\mathbf{w}} \\ \tilde{\mathbf{u}} \\ \widetilde{\boldsymbol{\Phi}} \end{bmatrix}^\top \begin{bmatrix} \widetilde{A}^\top P + P\widetilde{A} + \alpha P & P\widetilde{E}_w & P\widetilde{B} & P \\ \widetilde{E}_w^\top P & 0 & 0 & 0 \\ \widetilde{B}^\top P & 0 & -I & 0 \\ P & 0 & 0 & 0 \end{bmatrix} \begin{bmatrix} \tilde{\mathbf{e}} \\ \tilde{\mathbf{w}} \\ \tilde{\mathbf{u}} \\ \widetilde{\boldsymbol{\Phi}} \end{bmatrix} \leq 0 \tag{A.15}$$

yielding (3.36). Furthermore, from (A.14) we get

$$\begin{aligned} V &\le e^{-\alpha t} V(0) + \int_0^t e^{-\alpha(t-\tau)} \, \left[\tilde{\mathbf{u}}^\top \tilde{\mathbf{u}}\right] \, d\tau \\ &= \int_0^t e^{-\alpha(t-\tau)} \, \left[\tilde{\mathbf{u}}^\top \tilde{\mathbf{u}}\right] \, d\tau \\ &= e^{-\alpha t} * \tilde{\mathbf{u}}^\top \tilde{\mathbf{u}}. \end{aligned} \tag{A.16}$$

By setting $\tilde{\mathbf{w}}^\top \tilde{\mathbf{w}} \le \bar{d}$, we have

$$\mathbf{r}^\top \mathbf{r} \le \gamma \times \left(e^{-\alpha t} * \tilde{\mathbf{u}}^\top \tilde{\mathbf{u}} + \bar{d} + \tilde{\mathbf{u}}^\top \tilde{\mathbf{u}} \right).$$

Therefore, we obtain the adaptive threshold as

$$J_{th,dyn} = \sqrt{\gamma \times \left(e^{-\alpha t} * \tilde{\mathbf{u}}^\top \tilde{\mathbf{u}} + \bar{d} + \tilde{\mathbf{u}}^\top \tilde{\mathbf{u}} \right)}.$$

□